Harnessing Non-invasive Imaging and Modeling towards Early Detection of Tumor Resistance to Targeted Therapy

By

Jie Zhao

Dissertation

Submitted to the Faculty of the

Graduate School of Vanderbilt University

in partial fulfillment of the requirements

for the degree of

DOCTOR OF PHILOSOPHY

in

Physics

May, 2017

Nashville, Tennessee

Approved:

Erin C. Rericha, Ph.D.

Thomas E. Yankeelov, Ph.D.

John P. Wikswo, Ph.D.

Shane M. Hutson, Ph.D.

ACKNOWLEDGEMENTS

I have had the great privilege to work with many excellent scientists during my years in graduate school at Vanderbilt. First and foremost, I'd like to thank my advisor, Erin Rericha, for showing me from the very beginning how science should be done. I'm grateful to be in a cooperative and stimulating lab she nurtured where I gained much both in knowledge and as a person. She provided me with guidance, support, and freedom when I needed them the most. Her enthusiasm for discovery, her upbeat spirit and persistence to resolve problems, and her unbounded support will always remain in my heart.

Among my colleagues, I'd like to thank Halina Onishko who acquired most of the experimental data in this thesis. Her diligent and rigorous work ethic, and her welcoming personality made our collaboration both rewarding and enjoyable. I'd also like to thank Abigail Searfoss, Jonanthan Ehrman, and Austin Oleskie from the Rericha lab for working and sharing ideas together. Their friendship made my years in graduate school even more memorable.

I'd also like to thank Professor Thomas Yankeelov for his guidance and feedback throughout our collaboration. He has taught me much about respect and discipline – probably more than he intended. His humor lights up everyone that he encounters and makes our collaboration unforgettable. Jared Weis, David Hormuth, and Jennifer Whisenant from his lab provided many critical resources to further the project as well as help me learn and grow as a scientist.

I'd like to thank my committee members for both challenging me and encouraging me in the past few years. Professor Hutson has provided me with insightful feedback for this thesis. Professor Wikswo's exuberance and creativity have always inspired me to look at my research

from an exciting angle.

Last but not least, I’m grateful to have my family and my friends Naian, Xinyuan, Junjie, Jialei, Jaggi, and Kenner throughout the years. Their understanding and unconditional support motivate me to do better work as well as to be a better person.

TABLE OF CONTENTS

Page

LIST OF FIGURES

LIST OF TABLES

1. INTRODUCTION

1.1 Motivation

Cancers are one of the leading causes of morbidity and mortality worldwide. In 2012, approximately 14 million new cancer cases were diagnosed and 8.2 million people died from cancer related disease [1]. In the US, cancer related disease was the second most common cause of death in 2016, contributing about 25% of all deaths[2]. It is estimated that in 2017, there will be 1.7 million new cancer cases diagnosed and 0.6 million cancer deaths in the US[2].

Strategy for cancer treatment varies depending on the type and stage of the tumor(s). Therapy options include: surgery, radiation, chemotherapy, immunotherapy, targeted therapy, hormone therapy and stem cell transplant, with most patients receiving a combination of these therapies. A major clinical hurdle is the tendency for cancer to either not respond to the treatment provided or to recur after initially demonstrating response. An ambitious goal of cancer modeling is to provide a platform to choose the optimal combination, including dose and timing, of therapies such that a patient's tumors never grow.

While in some fields of physics it is possible to conceive of modeling from first principles with zero parameters, our current understanding of cancer biology is incomplete and any quantitative tumor model will necessarily contain parameters such as growth rate, mutation rate, drug transporter efficacy, etc that must be determined from experiment. Populating these parameters for clinical purposes is problematic as many are not directly measurable and some fraction is likely to vary depending on conditions, such that the average literature values are insufficient.

In this work, we explore whether clinical imaging can be leveraged to both populate model parameters and to identify poor responder patients early in the course of therapy. Clinical imaging is currently the major tool in diagnosis, accessing staging, and evaluating cancer growth and treatment response. Advanced imaging techniques such as Computed Tomography (CT) scans, Magnetic Resonance (MR) imaging and Positron Emission Tomography (PET) are able to provide 3D measurements of tumor cell number, metabolic activity, perfusion, and. Hence, clinical image provides a powerful set of measurements to refine mathematical models that capture and predict the treatment.

1.2 Overview of thesis

In chapter 2, we review current mathematical modeling work in the context of the development of cancer treatment, and highlight our contribution to this effort.

In chapter 3, we construct a simple two phenotype model for tumor growth under therapy. We prove that the simplified two state model can capture a wide spectrum of drug responses. Inspired by the work in ecological dynamics, we propose to apply a less known size exclusion diffusion model in multi-phenotype tumor's cell-cell interaction in space.

In chapter 4, we extend this work to consider clinical imaging. From ongoing work, we expect that tumor parameters, such as growth rate or drug induced death rate, are sensitive to environment and vary from patient to patient. We propose that serial imaging via non-invasive methods could be used to extract these parameters and to identify the presence of the resistant phenotype. We determine the threshold for detecting resistance as a function of the imaging frequency, measurement noise and tumor composition.

In chapter 5, we outline a set of intermediate experiments to test the model. We use 2D *in vitro* experiments to examine the spread and mixing of two tumor phenotypes. We find no significant advantage of either diffusion model, however, the experiment revealed a dependence of the cell diffusion and surprisingly, packing fraction, on cell type.

In chapter 6, we present an experimental study of non small cell lung cancer growth in different cell culture environments. We find that the response to targeted therapy is sensitive to the stiffness of the environment, and point that stiffer environments increase the likelihood for a *de novo* resistant population.

In chapter 7, we summarize our findings and present new directions to further this study.

2. BACKGROUND

This thesis contributes to a broader research goal of pushing mathematical models of tumor growth and treatment response towards relevance to clinical practice. In particular, in chapter 4 we consider whether a simple tumor model could be used to ascertain if a patient will exhibit resistance to a given drug therapy. Identifying resistance early in the course of drug therapy has clear benefits. Not only does it limit the exposure of the patient to toxicities that are not actually beneficial, it provides the patients the opportunity to switch to a potentially more efficacious treatment protocol. Indeed, there are a large number of potential treatments and treatment combinations available, but not a clear rationality on how to prescribe them.

In order to put our work in context, we use this chapter to (1) describe a subset of the variety of treatments available to patients and how they came about; (2) describe the general structure of mathematical models applied to tumor growth and therapy response; (3) motivate how clinical imaging can be incorporated in this effort; (4) introduce therapy resistance as an important clinical problem; (5) provide a brief overview of how other researchers are using mathematical models to manage resistance.

2.1 Brief history of cancer treatment

The earliest mention of breast cancer in recorded history dates to 1500 BC in Egypt; unfortunately for this patient, cancer then, was described as incurable. While science has learned much about the disease over the centuries, cancer remains the one of the leading cause of death in the world.

In the last century, multiple new treatments have emerged. Depending on the type and progression of cancer, a patient will undergo several forms of therapy including: surgery, radiation, chemotherapy, targeted therapy, hormone therapy, immunotherapy, and stem cell transplant. In this chapter, we briefly describe the historical rationale for each of the above therapies. As there are so many treatments available and more to come, a key need is to rapidly assess whether a given therapy will be effective on a patient specific basis. We highlight therapy choices for which mathematical tumor models have or can play a role in developing.

2.1.1 Surgery

Treatment by surgical removal of the solid tumor from the patient has a history as old as cancer. Indeed, the Ancient Egyptians would remove tumors from under the skin. Along with the development of surgical technique, removal of the tumor and large amounts of surrounding tissue, such as a radical mastectomy for breast cancer, gained popularity in the 1880s[3, 4]. Breast cancer patients treated in the time period from the late 1890s through the 1970s routinely endured surgery that removed the whole breast, the surrounding lymph node, and the chest muscle, disfiguring the patient. The underlying hypothesis that led to radical mastectomies indicated that cancer was a local disease. Clinical trials in the 1970s[5, 6], however, proved no significant survival advantage for patients that underwent radical mastectomy compared with patients that received a more conservative surgical procedure. It became increasingly recognized that cancer has a systemic component and that surgery proceeded by and followed up with other therapies became the standard therapy regimen. Recent literature suggests that surgery in some cases may exacerbate metastasis by introducing more tumor cells into the blood stream, though these findings are controversial [7].

2.1.2 Radiation therapy

Radiation therapy is commonly applied for tumors that are unable to be removed surgically or as part of adjuvant and neo-adjuvant therapy to shrink the tumor. Radiation therapy uses targeted high-energy photons (X-rays) to cause DNA damage inside the tumor cells through molecule ionization. The ionization process is predominantly caused by the Compton effect[8], where outer electrons in DNA molecules are scattered out by the injection of high-energy photons. It is one of the most widely used cancer therapies and is applied to ~ half of cancer cases. Unfortunately, both normal healthy cells and tumor cells are susceptible to DNA damage caused by radiotherapy, and radiotherapy is recognized as a carcinogen. Studies on radiotherapy suggest that cell sensitivity to radiotherapy depend on the position of the cell within the cell cycle (resting cells are more resistant), radiation dosing, and oxygen supply (as oxygen is a potent radio-sensitizer, resistance level is higher in hypoxia environment)[9-11]. These observations have inspired mathematical modeling in order to understand and optimize, phase dependent killing, dosing optimization, oxygen delivery related angiogenesis[12-15].

2.1.3 Standard chemotherapy

Chemotherapy uses chemical substances to cure or manage cancer; it can be divided into two major categories: the traditional standard chemotherapy and molecular targeted therapy. Standard chemotherapies are cytotoxic and act on both proliferating normal and proliferating cancerous cells. The first drug isolate found to have antitumor properties was Nitrogen mustard[16]. Soldiers who were exposed to an accidental spill of sulfur mustard during World War II were found to have depleted cell populations of the bone marrow and lymph nodes. Similar to sulfur mustard, Nitrogen mustard and other classes of alkylating agents, form bonds with single strand and double strand

DNA. This leads to DNA damage and prevents a proliferating cell from passing through replication or chromosome separation cell cycle check points, often triggering apoptosis. While cancer remission in response to mustard gas proved short, alkylating agents and platinum drugs that work through a similar mechanism are still used to treat aggressive cancers. Unfortunately, these patients are at risk for development of leukemia[16].

Another common chemotherapy drug is Antimetabolite. It has similar structures to essential cell nutrients such as vitamins, nucleosides and amino acids. Antimetabolite competes with these nutrients for essential enzyme or receptor binding sites. This competition eventually leads to the inhibition of cell proliferation. The first discovery of antitumor antimetabolites is methotrexate, a folic acid antagonist, made by Farber and Kilte during the 1940s[16]. Derivatives of pyrimidine and purine also fall within this class.

Two chemotherapy drugs that are commonly used in modern cancer treatment are paclitaxel and doxorubicin. Paclitaxel, first isolated from the Pacific Yew tree, was discovered in the 1960's as part of the National Institutes of Health natural products discovery. Paclitaxel interferes with cell division, most likely by stabilizing microtubules during mitosis and preventing cells from passing through cell cycle check points[17, 18]. Side effects from paclitaxel include nausea, reduced appetite, and toxicity of neurons. As the drug is not well soluble in water alone, it is often delivered intravenously dissolved in an ethanol water mixture and is responsible for the burning sensation patients feel. Despite these side effects, paclitaxel is widely prescribed and patients receiving paclitaxel after breast cancer surgery tend to do better than those who do not[19]. Like many other chemotherapy drugs, resistance to paclitaxel is an active area of research[17].

Doxorubicin is a synthetic derivative of an antibiotic produced by the soil bacteria *Streptomyces peucetius*[20]. The full mechanism of action of doxyrubicin is still debated; however, it is known to fit within strands of DNA – a chemical process known as intercalation[21]. Doxorubicin impacts DNA replication by preventing regions of the double helix from resealing. Successful DNA replication and formation of chromosomes is required for cell cycle progression. Hence, doxorubicin sends proliferating cells into cell death. As for side effects, doxorubicin is responsible for many of the side effects commonly associated with chemotherapy including nausea, hair loss, low immune response, and organ toxicity.

2.1.4 Molecular targeted therapy

Targeted therapies build on the paradigm that genetic mutations distinguish cancer from normal tissue. There was no systematic theory of carcinogenesis before Bishop and Varmus discovered the first oncogene in 1976[22], following the discovery of DNA by Watson and Crick in 1953[23]. Subsequently, more hallmarks of cancer at the genetic level have been discovered by molecular biologists [24, 25]. Targeted therapies are rationally designed drugs that bind or disrupt a specific mutation, gene amplification, or translocation associated with the cancer. The first such drug, Gleevec (imatinib), specifically targets the BCR-ABL fusion protein. A subset of patients with chronic myelogenous leukemia (CML), acute lymphoblastic leukemia (ALL), or acute myelogenous leukemia (AML), have a chromosome abnormality where the ABL gene from chromosome 9 joined the BRC gene from chromosome 22, and these cells produce a BCR-ABL fusion protein. The BCR-ABL protein acts as a tyrosine kinase, a class of signaling molecules that relay phosphate groups from ATP to other substrates, increasing their activity and frequently promote cell proliferation over apoptosis. Imatinib acts as an inhibitor to BCR-ABL and other

tyrosine kinases by binding irreversibly near the phospho relay site, preventing the molecule from signaling. In addition, the molecule bound by imatinb is sequestered to the nucleus, further reducing its anti-apoptotic effect. A subset of patients treated with imlatinb do very well[26, 27], however, both *de novo* and acquired resistance to imatinb is a clinical problem.

In the last two decades, many other targeted drugs have been introduced into therapy. Drugs that act as growth factor inhibitors/ apoptosis inducers follow the imatinib model. Experiments presented in this thesis use the targeted drug erlotinib, a type of epidermal growth factor receptor (EGFR) inhibitor. EGFR is shown to have elevated expression in a range of cancers [28], and erlotinib blocks the EGFR tyrosine kinase activity and further signaling cascades by blocking its ATP binding site. In addition, drugs have been developed to target the supporting infrastructure for the tumors. For instance, angiogenesis inhibitors block the formation of new blood vessels to cut out tumors' blood nutrition supply. Hormone therapies are prescribed for some breast and prostate cancers that require certain hormones to grow. Finally, monoclonal antibodies have been developed that specifically bind to a molecular target on the cancer cells and kill the cell either through exposure to a toxic chemical linked to the antibody or by identifying the cell for immune destruction.

2.1.5 Other frontiers

In this thesis, we will be concerned with detecting resistance to targeted and cytoxic therapies. Recently, new therapy avenues have been developed including immunotherapy and stem cell transplants. While exciting, they are not yet directly linked to this work and hence we refer the interested reader to the book by Mukherjee[29] and Documentary by Barak Goodman—*Cancer: The Emperor of All Maladies[30]*.

As is evident from this discussion, research over the last a few decades have led to a rapid increase in the number and types of treatment available for patients and clinicians, see Figure 2.1 that summarizes the development of tumor treatment since 1882. A key clinical question is what therapies and with what temporal and dosing strategy should be used in order to manage the cancer and minimize the toxicities to the patient. The basis for current treatment strategies can be found rooted in two discoveries from the 1950s and 1960s. Kahn and Furth's murine experiment found that a single implanted leukemia cell is able to cause animal death, hence chemotherapy should be administered in adequate concentration and duration so that all cancer cells are killed[31]. The second strategy uses drugs in combination. Famous examples include the so-called VAMP combination (composed of vincristine, amethopterin, 6-mercaptopurine, and prednisone) for childhood leukemia and later improved version of MOMP and MOPP[32]. These two dosing strategies were applied to some cancers in the 1960's and resulted in the first observed lasting complete remission by chemotherapy, a huge milestone for oncology. In the later part of the 20th century, researchers found new strategies to more efficiently design and discover cancer drugs from an extensive repertoire of chemicals as well as developed the massive and expensive clinical trial structure needed to test these drugs. Today the survival rate for both childhood leukemia and Hodgkin's disease treated by chemotherapy are above 90%. As dosing and drug combination has been proved to have significant effect on treatment result, they have also been the active focus of mathematical modeling work to optimize treatment strategy to overcome acquired resistance to chemotherapy[33, 34] [35, 36].

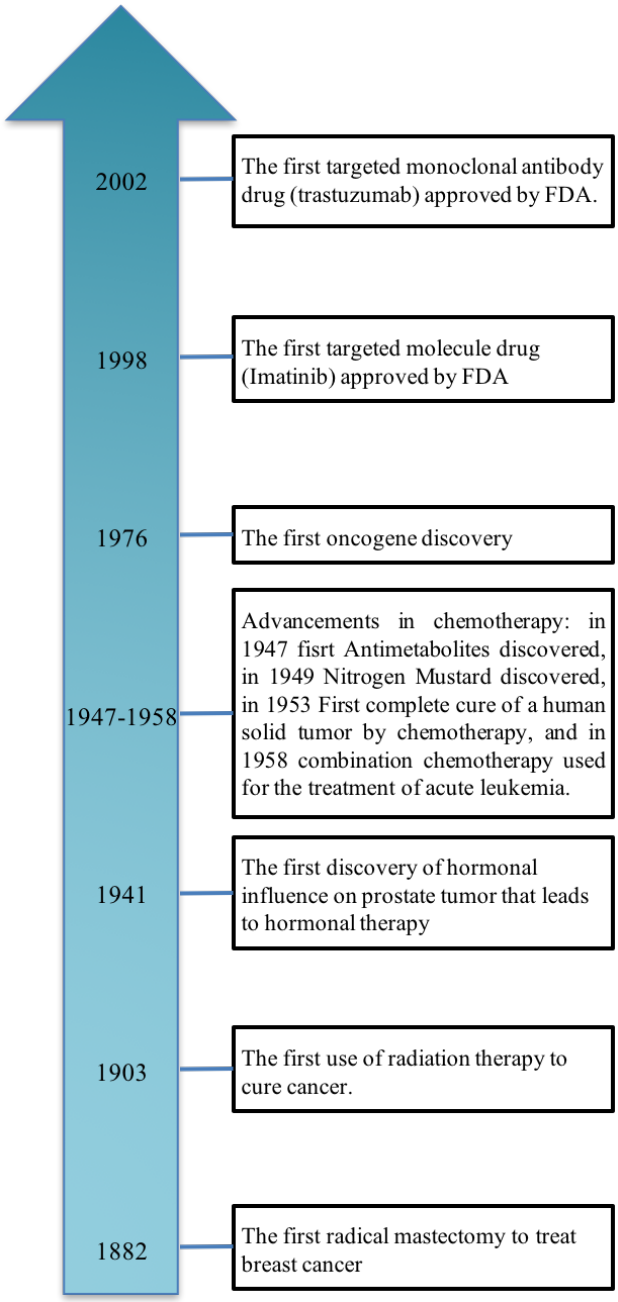

Figure 2.1 Recent progress in cancer therapy. Information are selected from reference [22].

2.2 Modeling of cancer progression

The major goal of clinical oncology is to diminish and eradicate cancer cells. Mathematical models of tumors are therefore constructed to predict the kinetics of tumor cell growth and death. Tumor modeling approaches to cancer can be loosely divided into two categories (1) models that consider how the physics of the environment, such as nutrition delivery and diffusion, the mechanical environment and the tumor morphology, influence the rates of cell growth and death; (2) models that consider biological variation and adaptation that impact the proportion of tumor cells growing and dying, such as the impact of genetic/epigenetic mutation, the position of cells within the cell cycle, and most recently, the growth of cancer stem cells. Here we briefly introduce the basic growth laws frequently used in tumor models, then, we provide examples from both model categories and discuss their current contribution to clinical oncology.

2.2.1 Growth kinetics

In vitro and *in vivo* [37-39] experimental observations find local tumor cell population growth follows a sigmoidal curve. Small tumors or low-density cell populations undergo exponential growth. Exponential growth does not last indefinitely; instead, the growth rate decreases and often plateaus. The biological mechanism that saturates cell growth is not well understood [37, 40], but frequently the plateau is attributed to resource restriction or contact inhibition[41]. Commonly used models that capture these observations include: (1) the exponential model, (2) the Gompertz model, (3) the Bertalanffy model, and (4) the logistic growth model. Below we provide a short description of each of these models and, if possible, their biological interpretation. In chapter 3, we will compare the growth of non-small lung cancer cells to each of these models and connect the measured growth rates with the cell signaling networks and the surrounding environment.

2.2.1.1 Exponential model

The unregulated division and expansion is one of the most fundamental observations about tumor[24, 25]. From the simple assumption based on cell cycle that there is a constant fraction of cells that are in mitosis phase, it follows that the growth of a tumor cell population is exponential growth, as in equation

$$\frac{N(t)}{dt} = kN(t) \tag{2.1}$$

$$N(t=0) = N_0 \tag{2.2}$$

where k is the fraction cells in mitosis. This model predicts that the time for a tumor cell population to double in cell number is constant. The exponential model captures the growth pattern of cells at low density or low volume, however, all known observations have shown that the doubling time increases as tumor cells grow larger and denser. To account for the observed slowing down, Mendelson proposed a modification to the exponential model based on scaling. Briefly, the number of tumor cells grows as the tumor volume, while the surface area of the tumor grows as the volume to the power of 2/3. The model assumes that the cells at the tumor surface, which are in contact with nutrition and oxygen, are primarily responsible for the tumor growth. Hence:

$$\frac{N(t)}{dt} = kN(t)^{\frac{2}{3}} \tag{2.3}$$

$$N(t=0) = N_0 \tag{2.4}$$

The above model was tested by Dethlefsen [42]. They monitored the growth of murine tumors through caliper measurements in three dimesions. The modified model improved the agreement

with experiment, however, it still predicts the tumor will grow infinitely and thus does not fit experimental observations on later tumor growth.

2.2.1.2 Gompertz model

The Gompertz model was introduced to model tumor growth by Anna Kane Laird in 1964 [43]. Instead of a growth rate that's constantly proportional to total tumor cell number, the Gompertz model assumes that the proliferating cell fraction decreases exponentially in time.

$$\frac{N(t)}{dt} = ae^{-bt}N(t) \tag{2.5}$$

$$N(t=0) = N_0 \tag{2.6}$$

The Gompertzian model predicts a sigmoidal growth curve and asymptotes to a constant cell number as *t* goes to infinity.

2.2.1.3 Bertalanffy model

The Bertalanffy model was proposed by Ludwig von Bertalanffy in 1949 [44]. This model is similar to the modified exponential model proposed by Mendelshon, but with an additional term to account for cell death.

$$\frac{N(t)}{dt} = kN(t)^{\frac{2}{3}} - \beta N(t) \tag{2.7}$$

$$N(t=0) = N_0 \tag{2.8}$$

Where β is a scaling factor related to natural cell loss. The Bertalanffy growth curve is also sigmoid in shape, and tumor reaches a steady cell number when the growth and death term are balanced.

2.2.1.4 Logistic growth

The logistic growth model considers the competition between tumor cells for resources to support proliferation by introducing a carrying capacity, the maximum reachable cell density/volume set by the environmental conditions. The general form of logistic growth is

$$\frac{N(t)}{dt} = kN(t)(1-\frac{N(t)}{\theta}) \tag{2.9}$$

$$N(t=0) = N_0 \tag{2.10}$$

where θ is the carrying capacity. Both the logistic and the Gompertzian models predict sigmoidal growth that asymptotes to a constant cell number, however the models differ in shape —the logistic curve is symmetric about the inflection point, while the Gompertz model is not.

2.2.1.5 Comparison to experiment

Despite the ubiquity of these models in the mathematical literature, few direct comparisons to experiment have been made. Gompertz is one of the most widely used tumor models. Some have found that it is a better description of *in vivo* data and is convenient to relate to experimental data [40]. The exponential decrease rate *b* lacks a physiological basis, however recent observations and subsequent modeling work have linked *b* to the idea of tumor self-seeding [45]. A review paper in 1982 suggest the Bertanlanffy model gives the best fit for 7 out of 10 tumors grown in

mice (induced sarcoma), and the logistic model fit best for the patient data (untreated primary tumor of human lung) [39]. Later work finds that the logistic model is proven to be advantageous in describing *in vivo* tumor growth of breast, lung and liver [38]. In this thesis, we also employ the logistic model to account for the growth kinetics of tumors.

2.2.2 Apoptosis kinetics

Mathematical modeling of cancer has primarily focused on tumor cell growth, perhaps unsurprisingly, as therapies found to kill cancer cells arrived centuries past the first observations of cancer growth. The most widespread population model for cancer cell death was initially proposed in the 1980's and takes a similar form to the exponential growth model. The log-kill model considers that an intervention, such as a drug, will decrease the cell population in proportion to the total cell number

$$\frac{N(t)}{dt} = -kN(t) \tag{2.11}$$

where k can depend on environmental variables such as drug concentration or the presence of oxygen. Thinking from this model drives many of the current approaches to measuring drug efficacy in patients, such as the RECIST criteria which measures treatment efficacy by monitoring the change in volume of the tumor[46]. In addition, the log-kill hypothesis drives many of the approaches to prescribing chemotherapies. For example, prescribing maximally tolerated dosages of the chemotherapy drug is directly connected with considerations that a higher k will kill a larger proportion of drugs. Applying drugs in combination considers that if each treatment, given in isolation, has an efficacy of k, then the combined treatment should have an efficacy of k_1+k_2.

Norton and Simons[47] proposed a revision to this model by taking into account the reduction in cell proliferation with increasing cell number (Gompertzian or Logistic growth). In this approach, anti-proliferative drugs would be effective against small rapidly dividing tumors at a lower concentration compared with larger tumors. Since the growth rate impacts the efficacy of the drug, the growth and death terms are not easily separable. Norton-Simon's predicts that the tumor cell number will change as

$$\log(N(t)/N(t_0)) = \log(N(t_\infty)/N(t_0)) + F(t) \tag{2.12}$$

$$F(t) = 1 - ex\{-b(t - k\int_{t_0}^{t} C(x)dx)\} \tag{2.13}$$

F(t) includes the Gompertzian growth, k is the efficacy of the drug and C describes the time dependent concentrations of the drug.

The Norton – Simmons hypothesis dominates thinking for current treatment strategies to maximize patient's quality of life under treatment. Initial treatment should be given in a dose dense fashion and remission can be maintained by a lower dose. Both of the above models are counterintuitive from the perspective of rationally designed targeted therapy. First, the motivation behind the model stems from considerations of cancer as a disease solely of excessive proliferation. This perspective is consistent with the mechanisms of action from the initially successful chemotherapies such as the anti-folates and taxol which interfere with the mechanics of cell mitosis. However, targeted therapies may require a subtle change in thinking when considering how to appropriately model their effects. The rationale behind the development of many targeted therapies considers cancer as a disease where the balance between cell proliferation and cell death has been tipped in favor of proliferation. Drugs are designed not to inhibit mitosis (and hence

protect the healthy cell populations that divide frequently) but to restore the natural dominance of pathways associated with cell death in tissues[24]. Second, targeted therapies are molecular inhibitors and thinking in terms of molecular interactions would instead suggest that a given dose of drug should kill a fixed number of cells (those with sufficient number of drug molecules to inhibit the target) as opposed to a fixed fraction[34]. In short, more work is needed to improve treatment response models for targeted therapy.

2.2.3 Solid tumor modeling

The above models consider the growth of a one-dimensional tumor that grows without the restriction of the surrounding space. Considering the complexity of tumor and tissue interactions, it is surprising that these simple growth models are at all predictive of tumors growing *in situ.* Modeling for solid tumors that includes spatial components seeks to improve our understanding of tumor growth laws and the predictive power of models by incorporating more complexity.

The descriptor “solid” generally refers to benign or malignant tumor tissues that don’t contain a liquid volume or cyst. Examples of solid tumors include those found in breast, prostate, and the lung. The development of solid tumor modeling has evolved for decades [48-59], see Figure 2.2 for a summary of major progress in this field and detailed in later part of this section. Imaging techniques such as microscopy, CT and MRI provide essential data for solid tumor model development and refinement.

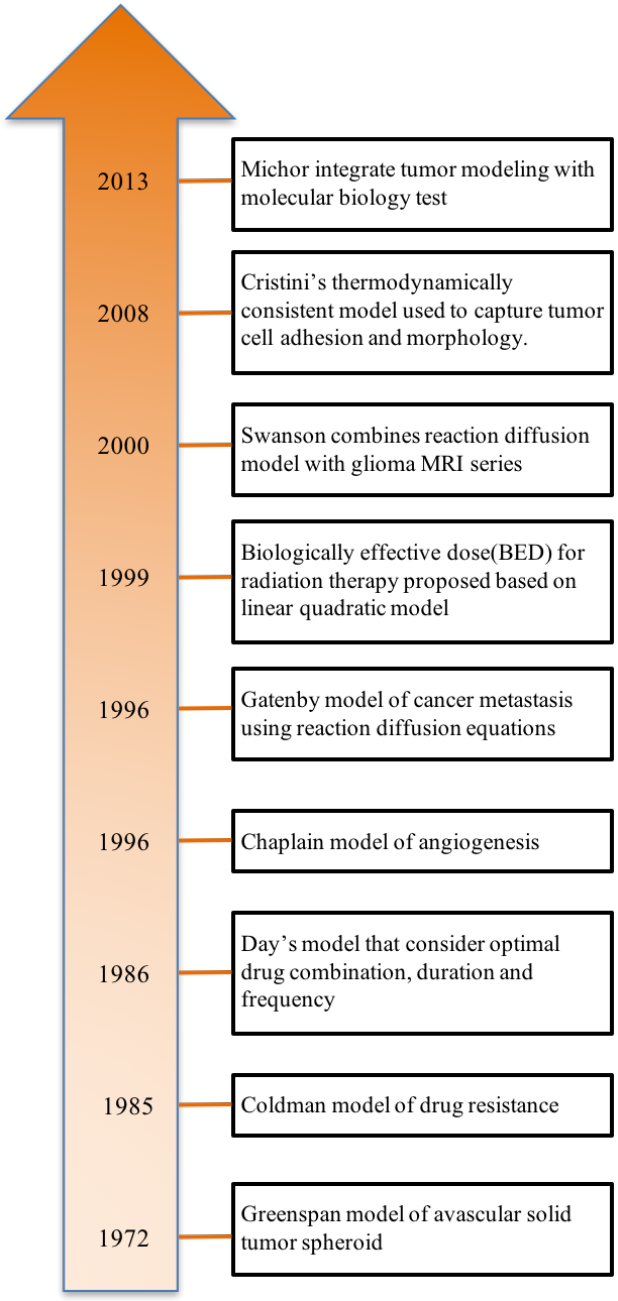

Figure 2.2 Recent progress in cancer modeling.

One of the earliest and influential solid tumor models was developed by Greenspan [54] and colleagues. They developed a model for avascular solid tumor spheroid growth thought to apply

to early stage tumor development. Using a system of ordinary differential equations that models the tumor radius, the diffusion of nutrition, and the generation and diffusion of a growth inhibitor (created form the necrotic core), their model successfully reproduced the three layers of tumor behavior observed in histological examination of tumor spheroids, namely: an outer layer containing a high fraction of proliferating cells, a middle layer with viable cells that are not-proliferating, and the necrotic core, see Figure 2.3 (1). The model predictions for tumor growth, namely the predicted tumor outer radius versus time also agrees well with experimental observations. Their model could be applied to a wide range of experimental settings by changing the microenvironment parameters such as nutrient level and the rate of inhibitor generation. The model gives an explanation to the size equilibrium of a solid tumor: necrotic cells disintegrate while living cells continue to occupy their original space. However, the model assumes that the solid tumor is spherical and symmetric all the time, thus cannot account for the morphological variations observed in the experiments.

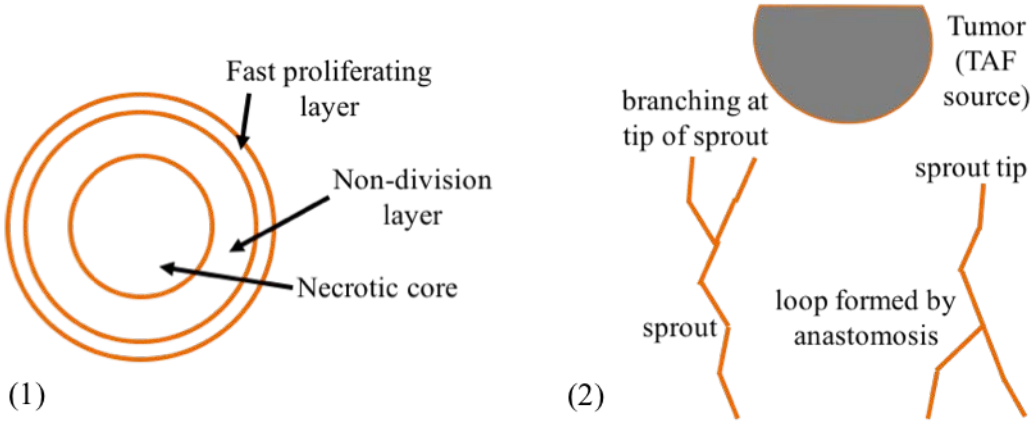

Figure 2.3 Examples of Tumor Morphologies. (1) Schematic plot of commonly observed solid tumor sphere: outside layer of fast proliferating cells, middle layer of non-division cells and inner most necrotic core. (2) Schematic plot of angeogenesis process: the tumor cells cluster secrete tumor angegenesis factor (TAF) that tract endothelial cells to migrate towards the cluster. The migration process is generally composed of directed growth towards tumor cluster through sprouting and branching. The loop formation of two sprouts contributes to the network formation of the endothelial cells.

Ordinary differential equation descriptions of tumor growth are insufficient for tumors requiring more than one spatial variable. To model the growth of tumors without spherical symmetry, Gatenby *et al* [60] proposed a reaction diffusion model (system of partial differential equations) to examine the impact of metabolism on pH and cancer cell migration. The authors assume that the glycolytic metabolism of tumor cells creates an unfavorable high pH environment for normal tissue. The high pH promotes the death of normal cells and the degredation of the ECM , hence, promoting the invasion of tumor cells into normal tissue. The reaction diffusion model considers the tumor tissue's spatial distribution, normal tissue's spatial distribution and the local pH level (see Figure 2.4.1), to describe the microscopic scale population interactions occurring at the tumor-

host interface. They successfully reproduced the experimentally observed pH gradient extending from a tumor into surrounding tissue and found that the velocities of the expanding tumor front generated in the model are consistent with *in vivo* tumor growth rates. They predicted a previously unrecognized hypocellular interstitial gap later found experimentally both *in vivo* and *in vitro*. However, their model doesn't account for the genetic changes and the appearance of central necrosis, and neither did they consider the environmental variations other than pH levels.

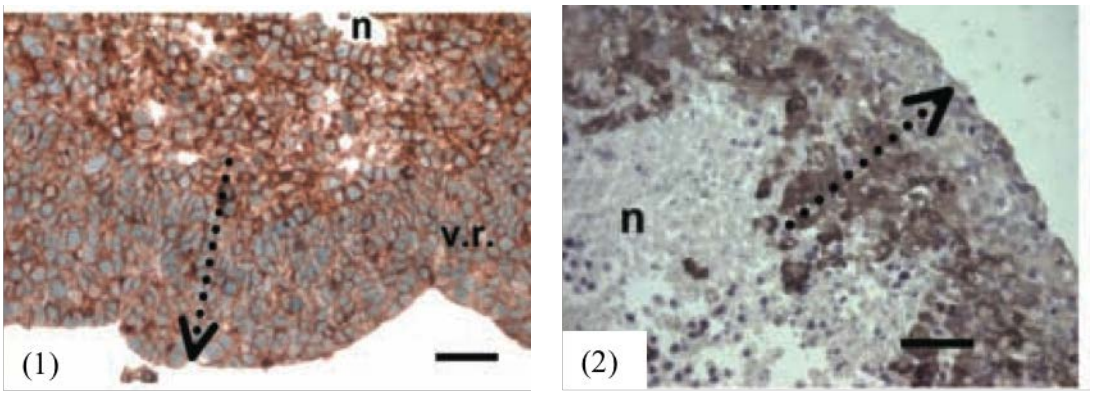

Figure 2.4 Illustration of experimentally observed chemical gradients. (1) NHE-1 staining (darker brown) of up-regulated Na+/H+ transporters towards the necrotic core shows a decrease in PH. (2) Immunohistochemical staining of tumor spheroids where increasing darker brown (increasing positivity for pimonidazole protein adducts) in the outward center direction indicating the decrease in oxygen. n indicates the necrotic core, bar is 50um. Figures are taken from[51] with journal's permission.

The reaction diffusion model is a common backbone for explorations of tumor growth in tissues. The group led by Kristen Swanson[61] has extended the use of this model to describe glioma

growth in the brain. Glioma is one of the most fatal cancer types that has a doubling time as little as 1 week and could expand throughout the central nervous system [62]. The Glioma is detectable by MRI at densities above 40,000 cells/cm^3. Briefly, the tumor can both grow locally and extended into space. The tumor cell motion into space is random, but the mobility of the cells depends on the local composition of the tissue (mobility is higher on white matter than on grey matter). The model then contains 3 parameters (two diffusion constants and one growth rate). To constrain the parameters, Swanson et al reexamined serial MRI scans reported by Tracqui [63]. From measurements of the growing tumor, they related the speed of the advancing boundaries to tow times of square root of diffusion coefficient times proliferation rate. From these parameter estimates, they compare the model predictions for the actual tumor boundary to the detection limits of clinical imaging and suggest that too many tumor cells are remaining behind from surgical removals guided by imaging margins.

The basis of the Swanson group's efforts considers that a reaction diffusion model with constant parameters is a reasonable description of glioma growth, however the predictive power of the model and the parameter estimation by DW-MR images had not been examined. Motivated by the Swanson group's approach, Hormuth *et al* [58] tested the accuracy of a similar model and DW-MRI (see Figure 2.5) constrained parameters applied the reaction-diffusion tumor growth model to glioma growing in rat brains. They first used an *in silico* study to test whether DW-MRI in the presence of experimental noise can constrain the model parameters sufficiently well to allow for the model to make predictions of tumor evolution at later times. They found that the predictions made by the model matched the original tumor evolution well (concordance correlation coefficient (CCC)>0.8). However, the similarly constrained model applied to *in vivo* tumor growth was less successful in predicting subsequent growth (CCC < 0.33). Later work by Weis et al [59] examined

simple considerations to improve the model predictive power for *in vivo* data such as a including a mechanically coupled diffusion constant, such that the motility of the cancer cells depended on the displaced healthy tissue, and a carrying capacity that varies in space. Their biomechanical model projected the tumor residual after neo-adjuvant therapy with high person concordance correlation (PCC=0.84), indicating promising potential of predictive modeling using MRI and mathematical models.

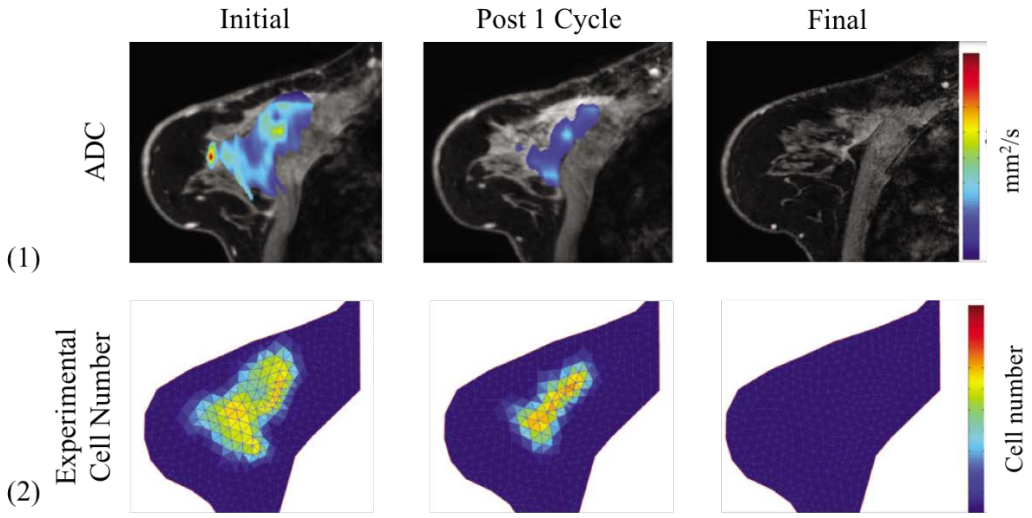

Figure 2.5 (1) Apparent Diffusion Coefficient (ADC) maps using diffusion weighted (DW) MRI overlaid on T1 structural image. (2) Converted cell number distribution based on image series in (1). Figure is extracted from [64]with journal's permission.

Reaction diffusion models of tumor growth can incorporate spatial variation in model parameters

(diffusion and cell growth). For instance, the Swason's group considers a link between hypoxia and tumor aggressiveness using multimodality imaging technologies[11]. Hypoxia is often suggested to be causally linked with radiotherapy resistance and tumor malignancy, see Figure 2.4 (2). They monitored 11 patients' glioma progression prior to surgery by both sequential MRI and PET. Sequential MRI is combined with diffusion reaction of model of tumor growth to infer tumor proliferation rate (ρ) and invasiveness (diffusion coefficient D). F-fluoromisonidazole (FMISO) based PET is used to indicate the oxygen level related hypoxia inside the tumor. They found strong correlation between hypoxic burden and active proliferation, but not between hypoxic burden and invasiveness, indicating increased proliferation is more likely to cause hypoxia compare to the invasive capability. Their work was innovative in the employment of a multi-mode imaging technique, and the application of bio-mathematical models to draw insights on the cause of hypoxia.

The above models describe a tumor's persistent growth into a relatively inert tissue. They are specifically formulated such that most of the parameters can be constrained by clinical imaging and hence models can be made patient specific. Another aspect of solid tumor modeling that is of vast interest is on angiogenesis. Angiogenesis can be found in wound healing, arthritis, and chronic inflammation. Folkman and Klagsbrun found solid tumor secretes a collection of chemicals now generally referred to as tumor angiogenic factors(TAF), which attract endothelial cells to migrate towards the solid tumor and eventually lead to the angiogenesis[65]. Works by Chaplain's group[56] is representative of the deterministic modeling effort in this aspect. In their simplified model, they monitored the growth of tumor and endothelial cells, assuming that the flux of tumor cells originated from both diffusion and taxis towards higher capillary cell density, and that the proliferation and apoptosis of tumor cells depend critically on the nutrient level supplied by the

blood vessels. Though their model is too simple to explain the detailed spatial progression of angiogenesis, it gives quantitative estimate of the tumor expansion speed.

More recent modeling work on solid tumor angiogenesis includes more detailed vasculature formation process in solid tumor. At first, endothelial cells sense the TAF secreted by solid tumor cells, and begin to migrate towards the gradient of TAF. The migration and proliferation of endothelial cells lead to the formation of finger like capillary sprouts. These sprouts go on forming connected loops (the process known as anastomosis) and eventually the capillary network that gives rise to the eventual vascular structure, see Figure 2.3 (2) The interaction between endothelial cells and extracellular matrix (including collagen fiber, fibronectin, etc.) is also found to be critical for the directed migration and cell adhesion[55]. Anderson and Chaplain in 1998[48] use a combination of stochastic discrete model and deterministic continuum model that is capable of addressing the above observations. The continuum model assumes that the migration of endothelial cells is governed by random mobility, chemotaxis to TAF gradient, and haptotaxis in response to fibronectin gradients. The discrete stochastic part models the random work, sprouting, and loop formation of the endothelial cells. Both parts are necessary to generate overall expansion and specific form of capillary growth in the angiogenesis process. It is one of the earliest example of multi-scale modeling of solid tumor.

Finally, it is worth noting the unique approach by Cristini's et al [50-53] to capture the complex morphologies during tumor growth. A continuum model of adhesion is created that is thermodynamically consistent—the authors introduce Helmholtz free energy to consider the cell movements resulting from cell-cell and cell-matrix adhesion forces. From numerical analysis, they conclude that for colonies with strong cell-cell adhesion, the colony boundaries tend to be smooth, while with weak cell-cell adhesion, it's likely the boundaries become fractal like, and prone to

develop invasive fingers. Their modeling methods are strongly influenced by concepts in thermodynamics, and is a typical example of physics models applied in biology.

2.2.4 Stellar example: linear quadratic model in Radiotherapy

Note in this thesis, we do not consider radiotherapy, however mathematical modeling provided considerable insight into how to best apply radiation therapy and we wanted to include this beautiful work here.

One of the most prominent applications of mathematical modeling in clinical oncology is the linear quadratic model in radiotherapy. *In vitro* studies, mouse models, and human clinical trials have been conducted to apply and test the quantitative predictions of the dosing and fractionation's effect on radiotherapy. We list the details of model framework, application, and contribution to clinical oncology here. We aim to show how mathematical modeling has been used in clinical oncology and point out its limitations to guide similar works in the future.

2.2.4.1 The formula

The inspiration for the linear quadratic model originated from the seminal work of Puck and Marcus[66] where they exposed *in vitro* mammalian cells to radiation and measured the cell survival rate *S* from a single radiation dose versus the amount of drug dosage *D*. The S vs D curve shows two regimes (1) a relative slow cell kill at low dosage (2) the linear (in log scale) drop of cell survival fraction at higher dosages.

The high dose response can be described by a linear model:

$$In(S) = -\alpha D + c \tag{2.14}$$

where c is a fitting constant. When D=0, S=1 (no treatment no death of tumor cells), implies that the fitting constant is 0 so that the surviving fraction depends exponentially on the dose,

$$S = \exp(-\alpha D) \tag{2.15}$$

A simple modification to the above expression includes a quadratic term to the model. This accounts for the relative slow cell kill (the so-called 'shoulder' in many literature, close to that of a quadratic function) at low dose delivery is to add the quadratic part

$$In(S) = -\alpha D - \beta D^2 \tag{2.16}$$

$$S = \exp(-\alpha D - \beta D^2) \tag{2.17}$$

2.2.4.2 The application

As was the case for the log kill model, the above simple and descriptive approach has profound practical implications on the scheduling of radiotherapy and the dose fractionation in order to optimize normal tissue preservation.

(1) Dose Fractionation

In external beam radiotherapy, the model can be used to consider how the therapy should be administered, for instance, total radiation dose D could be administered in *n* fractions, each a lower dose than the one before.

$$D = nd \tag{2.18}$$

If tissue of interest is dominant by the linear kill, effect of a single total dose

$$S_1 = \exp(-\alpha D) \tag{2.19}$$

is equivalent to the effect of n fractions of radiation dose of the same total

$$S_2 = \exp(-\alpha d)\exp(-\alpha d)...\exp(-\alpha d) \tag{2.20}$$

$$S_2 = \exp(-\alpha nd) \tag{2.21}$$

$$S_2 = \exp(-\alpha D) \tag{2.22}$$

as $S_1 = S_2$. In comparison, if the tissue of interest is dominant by the quadratic kill, the effect of a single total dose

$$S_1' = \exp(-\beta D^2) \tag{2.23}$$

has more cells killed than the fractionated dosing;

$$S_2' = \exp(-\beta d^2)\exp(-\beta d^2)...\exp(-\beta d^2) \tag{2.24}$$

$$S_2' = \exp(-\beta n d^2) \tag{2.25}$$

$$S_2' = \exp(-\beta D^2 / n) \tag{2.26}$$

as $S_1' < S_2'$.

(2) Normal Tissue Preservation

One widely used measure to illustrate the domination of linear or quadratic kill is the value of α/β, the so-called fractionation sensitivity. When α/β is high, tissue is relatively more dominant by linear kill, so that fractionated dosing has similar effect to a single high dosing. Consequently, when α/β is low, fractionated dosing is not as effective. As it turns out, many cancer tissues usually have higher α/β value, indicating the fractionated radiation dosing achieves similar effective kill of tumor cells while preserve the integrity of normal tissue. Here we listed in table the clinical reference of the estimated α/β value of various tumor tissue and healthy tissues.

Normal Tissue	Low α/β	
	Lung	3.5
	Skin	3.7
	Cord(myelopathy)	<3.3
Tumor tissue	High α/β	
	Lung	50-90
	Skin	8.5
	Cervix	>13.9
	Vocal Cord	>9.9

Table 2.1 α/β values for normal and tumor tissue. The listed information is extracted from reference [67].

(3) Biologically effective dose

As an application of linear quadratic model, the concept of biologically effective dose (BED) is proposed in 1999[68]. The BED estimates the total dose required to achieve the same cell kill as the studied single dosing *D* and aims to generalize the result of any treatment regime in radiotherapy based on rate of fractionation, total dosing and total treatment time, talking the form:

$$\mathrm{BED} = nd(1 + d/[\alpha/\beta]) - In2(T - T_K)/\alpha T_P \qquad (2.27)$$

where *n*, *d*, α and βare same parameters described in previous sessions, adding *T* as the total treatment time, T_k (*k* is abbreviation of kick-off) is the delayed time for repopulation, and T_p for cell doubling time.

2.2.4.3 The effectiveness and limitation

The application of LQ model has proven to be effective in explaining tumor response, and used as a practical tool to guide radiotherapy[69]. Several treatment strategies have been since derived from LQ model including hyperfractionation, hypofractionation, and accelerated fractionation. In hyperfractionation, total radiation dose and treatment duration remains roughly the same, but dose per fraction is decreased and. The LQ model hypothesizes this strategy will conserve low (α/β) tissue while effectively kill high (α/β) tissue. Such prediction is validated by clinical trials on breast, neck and head tumor [70, 71]. On the other hand, hypofractionation that composes higher per fraction dose are recommend for tumors that have lower than normal tissue (α/β) index, such as prostate tumor [72, 73]. Such hypothesis is also validated by multiple clinical trials [74, 75].

Despite the popular application of radiation therapy in cancer treatment, the biological process involved in cell apoptosis under radiotherapy remains elusive. One popular hypothesis[69] to explain the linear-quadratic model is that the radiation caused double-stranded breaks of DNA that is proportional to radiation dose, and further damage is caused by chromosomal aberrations as consequence of mispairing the broken DNA. Many other hypothesized biological process can be explained by the mathematical equations of the same form. The view of LQ model is still controversial. Zaider[76] argues, the LQ is useful but this mathematical model doesn't represent the cellular processes, while Box[77] famously stated 'All models are wrong, but some are useful'. As more understanding on the molecular biology in cancer is needed, we take the value of the second as the motto of this thesis: we don't aim to build the complete model of tumor drug response, but to have effective model to guide resistance detection.

2.3 Biology of drug and radiation resistance

For a given drug therapy to be effective, it is essential that an active form of the drug binds the targeted molecules in the cancer cells or on the surface of the cancer cells, see Figure 2.6. Each therapy except for surgical treatment must go through the pharmacokinetic process: (1) drug absorption, distribution, metabolism, and elimination; (2) be delivered inside cancer cell by cell membrane transporters; (3) maintain actively effective form upon arriving at targeted cells. Resistance to a given therapy could occur due to disruption at any of these steps. Even drugs can be delivered to the cancer cell, the *de novo* and acquired resistance of cancer cell can largely limit the effectiveness of therapy. The *de novo* resistance is referred to the intrinsic resistance to drug even before its administration. As tumor tissue is composed of a spectrum of tumor cells which vary in the types and number of proteins expressed, it is reasonable to consider some tumor cells

as are more resistance than others even before the drug is applied. Indeed, through single cell tracking, Tyson et al[78, 79] found that a commonly studied non-small cell lung cancer line (PC9), contains cells whose intermitotic follows exponentially modified Gaussian distribution, and distribution shifts systematically according to the external drug perturbations.

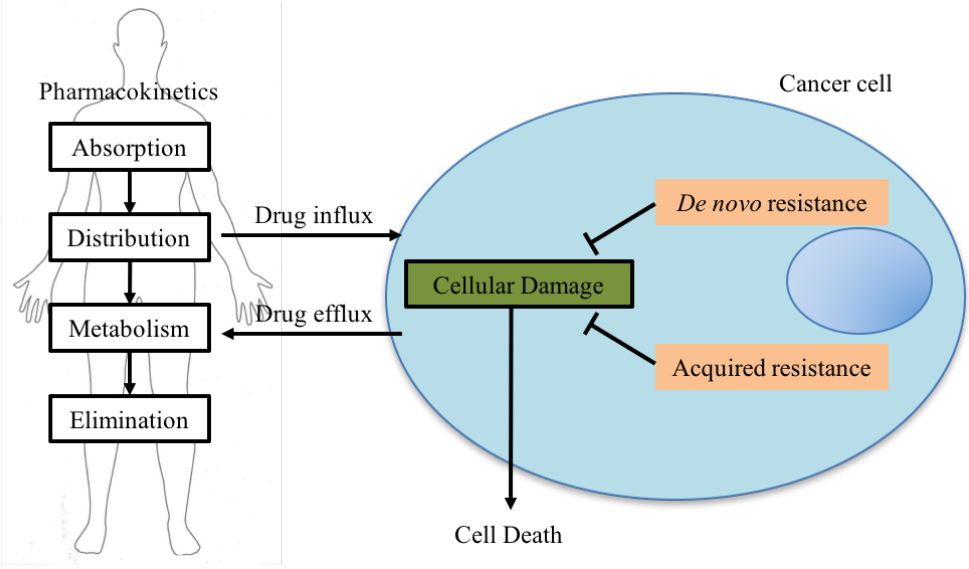

Figure 2.6 The drug cycle and general mechanism of drug resistance. At first the pharmacokinetic process: absorption, distribution, metabolism and elimination decide the amount of drug reach to cancer cells. Then the cancer cell surface transporters limit the amount of drug effectively go inside cancer cells. Eventually, different levels of *de novo* and acquired resistance oppose effective cellular damage by the drug. Figure is adapted from reference [80] with journal's permission.

Acquired resistance develops after drug administration when either the target changes itself through mutation, or the tumor activate another functionally equivalent pathway that doesn't depend on the target, and in a broad sense, the evolved microenvironment that keeps the drug from the target. Below, we mention a few known mechanisms that contribute to resistance to cancer therapy. We deliberately focus on mechanism which could contribute to *de novo* resistance, though there is overlap with acquired resistance pathways.

For many targeted and chemotherapies to be effective, the drugs must exist at sufficient concentrations within the cell in order to bind their cellular targets. In multi-drug resistant tumors, a cell membrane transporter protein increases the transport of drug therapies out of the cell. These transporter proteins, such as MBR1, may be over expressed in tumor cells prior to the administrated drug (*de novo* resistance*)*, or their synthesis could be induced by the therapy (acquired resistance). Similarly, other observed resistance mechanisms for both cytotoxic chemotherapy and targeted molecular therapy include the increased drug target expressions, drug inactivation and elimination, induced activation of pro-survival signaling, deregulation of apoptosis, resilient DNA damage repair system. Drug resistance mechanism is a complex subject, and an evolving research field. Interested reader can refer to [80] for more detailed information on this subject.

Tumor heterogeneity and *de novo* resistance is also linked to the hypothesis that a small number of cancer stems cells (CSC) act as the driving force for cancer recurrence, and the elimination of CSCs is critical for the improvement of cancer survival. A cancer stem cell, as its name suggests, is the cancer cell that possesses stem cell like properties: infinite self-renewal, and the ability to differentiate into multiple cell types. CSC's were first reported in 1997 when researchers found cells within the tumor that share similar markers as stem cells that give rise to

the tissues of the same origin. Using these stem cell markers, such as the expression or depletion of cell surface markers (eg. CD34+, CD38), CSC's have been found in a wide range of cancer types including acute myeloid leukemia, brain, breast, colon, ovary and so on[refs. The significance of the CSCs is still a topic of debate in the research field [81]. Targeted therapy on CSCs were subsequently discovered to control specifically the growth of CSCs.

The tumor microenvironment strongly influences treatment resistance. Regions with low oxygen (hypoxia) are widely observed in solid tumors due to tumor cells' rapid growth and adaptability. As oxygen is a component of the apoptosis pathway, cells that continue to proliferate and thrive in hypoxic regions are often less sensitive to radiotherapy and drugs administered through the blood are less likely to reach their targets. Therapies that impact the vasculature, such as anti-angiogenesis treatment or radiotherapy can either cause or exasperate hypoxic regions.

Tyson's group[82] examined another potential causes of tumor resistance through activation of redundant pathways, more specifically, the acquired resistance of breast cancer cell to endocrine therapies caused by the compensatory functions between estrogen receptor(ER)-regulated and growth factor receptor(GFR) regulated survival signaling pathways. In other words, inhibiting either of the two pathways will activate the other, resulting the survival of cancer cells under drug therapy. Experiments conducted by Liu et, al [83] showed that breast cancer MCF7 sub-closes transfected with GFR (HER/EGFR) displays three GRF distributions patterns that depending on the E2(primary estrogen in breast tumors) level. They modeled the three distribution patterns as a bi-stable biological switch with epigenetic component using system of ODEs and stochastic simulations. Their works shows how mathematical modeling can be used to draw insights on tumor resistance mechanism on the molecular level.

One example of using mathematics to inspire biological study is presented by Levy's group[84]. Their study is based on a clinical trial published in 2009 [85], where Chronic Myelogeneous Leukemia (CML) patients receives imatinib as main treatment, and achieves survival rate of 88% after 6 years follow up. Levy et al took the hypothesis that the death caused by drug resistance is mainly driven by cells that have self-renewal capability (such as the cancer stem cells), and use a stochastic growth model of cancer stem cells to explain the clinical data. After applying estimated parameters such as resistance mutations rate at 4e-7 per division, cell birth and death rate ratio (turnover rate) at [0.1-0.5], they concluded cancer stem cells in CML are more likely to divide symmetrically (into two cancer stem cells) rather than asymmetrically (into stem cell and progenitor cell), in order to account for the transition from chronic phase to acute phase of CML in the not survived patients. Though the estimated parameters such as mutation rate and turnover are difficult to measure and or test, their mathematical modeling work does provide an intriguing prediction to be tested by molecular biologist, and further our understanding of tumor drug resistance.

2.4 Mathematical models of drug response and resistance management

One of the earliest models of drug resistance can be found in Coldman's paper in 1985[36]. At the time of the publication, surgery, radiotherapy, and chemotherapy were the major strategies for cancer treatment. While recognizing the existence of inherent resistance to chemotherapy, their model focuses on the acquired resistance that is due to random genetic mutation. The major assumptions in their model include constant rate of tumor cells growth rate and death rate for the sensitive tumor cells, and fixed mutation rate for drug resistance. Their simplified model predicts that as tumors grow larger, the number of resistance cells increases and likelihood of cure decreases

exponentially. The impact of these model discoveries can clearly be seen in clinical practice. Cancer is frequently staged based on the size of the solid tumor is consistent with thinking that large tumors are more likely to have more resistant mutations. Therapy should be given as early as possible as these tumors are less likely to have mutations leading to resistance. Drug combinations are as good as, if not better than, single-agent therapy and the order of application doesn't matter.

Subsequent approaches consider the order in which drugs should be administered[15] [13, 14, 36]. Day considers the evolution of tumor cells within a heterogeneous colony as a continuous stochastic multi-type branching process, where one cell type produces off-springs of random type according to certain probability distribution. Under the cyclic treatment of two drugs—drug A and B, the cells are divided into four types: sensitive to both A and B, resistant to either A or B, and resistant to both. The four cell types are related to their particular growth rate, death rate, and cell kills rate under each drug. Practical implementation rules are given first by Day[14], generally referred as 'worst drug rule', stating it's better to apply less potent drugs at first and for longer period. Limited by computation cost at the time, Day only explored 16 treatment strategies of two non-cross-resistant drugs [14]. Work by Komarova et al [15] expand the investigation to cross-resistant drugs, and find in most cases best-drug first and worst-drug longer is more suitable. Though these models lack biological complexity of drug intake, drug synergy and resistance development, their approach is logically rigorous and representative of rational planning for drug administration.

Recently this modeling approach has been extended to include tumors which reach a finite size due to logistic or Bettany model factors [86]. The authors consider that each cell that replicates has some probability of acquiring a mutation, some of which could confer resistance, but no

mutation is selected unless treatment is applied. Hence, many potentially resistant mutants die out before therapy. They compute the probability that a given treatment will completely kill a tumor and find the length of time required to kill all sensitive cells. Their model could be used to update the risks to the patient for delaying treatment.

Another promising approach to integrate tumor modeling with molecular biology test is presented by Michor's group [87]. They compared genetic and phenotypic features of 47 breast cancer patients' biopsies pre- and post- neo-adjuvant therapy. Genetic features are extracted from immunoFISH-based analysis of four commonly amplified chromosomal regions in breast cancer-- 8q24.3, 10p13, 16p13.3, and 20q13.31. Epigenetic features are extracted from the staining of CD44 and CD24 surface marker. Based on their treatment response, patients are classified as pathological complete response (pCR) and pathological partial response (pPR) or stable disease (SD, in other words, no response). They found for partial and no response patients, the intra-tumor phenotypes shift significantly while intra-tumor genetic diversity maintains at the same level. Also interestingly, patients with completed pathological response have significant lower pretreatment genetic diversity.

The author proceeds to use proliferation marker Ki67 to constrain a 2D stochastic agent based tumor model, and found it's necessary to add phenotypic switching term to the proliferation model to explain the phenotypic distribution presented in partial response and no response patient. No constant switching rate could account for the discrepancy between simulation and observed patient data, indicating the switching rate should be dependent on other factors such as cell migration. We recognize analysis on the selected a few genomes and surface protein markers is not fully representative on the whole-genome based clonal architecture within a tumor. Before the whole genome sequencing of bulk tumor and single cell becomes more accessible, such

quantitative approach shows a promising step to build tools that integrate mathematical model with patient-specific molecular information to predict the treatment response.

Recent modeling works [27, 88] related to Chronic Myeloid Leukaemia (CML) provide interesting insights in CML therapy strategy. In 2005, Michor's group [27] studied the real-time PCR tracking of the BCR-ABL oncogene in 169 patients under imatinib therapy. They used deterministic ODEs to model CML as a four compartment system that consists of CML stem cells, progenitor cells, differentiated cells, and terminally differentiated cells. They proposed that imatinb works by preventing stem cells proliferation into progenitor cells, but is not as effective in eliminating stem cells. They argue that the probability of mutations increases with the treatment progression as leukemia stem cells grows in abundance. Their model successfully captured the drug response as well as relapse of CML. In the end, they recommended multiple drug therapy for rapidly growing disease. An interesting contrast to Michor's work is presented by Loeffler's group [88]. They used similar experimental method to track the CML cells in patients of two independent patient sets under imatinib treatment. Instead of modeling imatinib as limited elimination for CML stem cells, they assume imatinib works selectively on proliferating leukemia stem cells—accelerating their degradation and inhibiting their proliferation. Their model, too, successfully reproduced the key characteristics in the experimental data sets: the 5-7 years CML latency, bi-phasic decline in malignant CML cells under imatinib and the rapid relapse of malignant CML cells after treatment ceases. The authors propose an unconventional strategy to improve imatinib efficacy by combing imatinib treatment with proliferation-stimulating treatment. They proved that diverse models can reproduce the similar experimental results, yet yield different and even surprising treatment recommendations. Nonetheless, they both provide unique insights to the

existing experimental data. More molecular biology experiments are needed to test the validity of the hypothesis proposed in these two models.

2.5 Summary of the chapter

As seen from the historical development, the field of cancer treatment has evolved from an empirical practice of trial and error (eg. early mastectomy, discovery of cytotoxic chemotherapy, the introduction of radiation therapy) into a more logical system that designs treatment based on the increasing understanding of cancer (eg. the clinical trials of adjuvant and neoadjuvant therapy, the discovery of molecular targeted therapy).

The view of tumors has shifted from masses of fast proliferating tumor cells into a complex tissue where multiple colonial subtypes function collaboratively for survival and expansion. After decades of study of this complex disease, a comprehensive framework of cancer development is beginning to emerge. As suggested in the milestone paper by Weinberg and Hanahan [24, 25]the development of cancer is a multi-step process that usually involves sustained proliferation, uninhibited growth, reduced cell death, unlimited replication, activation of angiogenesis, and metastasis.

Along with the development of cancer treatment and our understanding of the biology of cancer, tumor modeling has evolved address available experiments at the time and guide cancer therapy for better outcome. The application of Linear Quadratic model in radiation therapy sets promising example for addressing tumor models in chemotherapy and others for strategic optimal therapy. With the development and wide application of clinical imaging, we witness the emergence of more comprehensive patient specific tumor models that contain proliferation characteristics, function dynamics, and environmental factors. This interdisciplinary approach for better

understanding and management of tumor has proven to be one of the essential factor in cancer treatment. Our work in this thesis aligns with efforts in this direction.

3. EXPERIMENTS INSPIRED MODELS

As outlined in chapter 2, a tumor is a complex system of cells that are diverse in functionality, heterogeneous in reproduction, capable of complicated evolution, and survive despite stressful environments. Testing a comprehensive and clinically relevant mathematical model that addresses all these processes is made exceedingly difficult as the parameters matter and can not yet be determined for each patient. In consequence, we propose to use a simplified model for tumor growth that can be constrained by available clinical imaging and used to predict therapy outcome. We first describe the ordinary differential equations (ODEs) used throughout the thesis to model tumor response to therapy. We demonstrate how a simplified two state model with sensitive and resistant phenotypes could be realistically applied to a wide range of tumor drug responses. Then we describe how the ODE models could be adjusted to partial differential equations (PDEs) to include spatial components. The PDE models can be used to capture tumor cells' spatial interaction and overall morphological evolution. The current commonly used independent diffusion PDE model for multi-phenotypes interaction ignores the spatial occupation of foreign phenotypes. We introduce a new size-exclusion diffusion model to model cells' migration taking into account of all phenotypes' presence in space.

3.1 Simplified two-state tumor progression model – ODE

3.1.1 Model description

Cancer is an extremely robust system, and survives under both internal and external perturbations[89]. One of the key contributors to this robustness is tumor heterogeneity: in both

functionality and proliferation [24, 25, 89]. Quaranta Lab shows that the sublines of Non-small cell lung cancer (NSCLC) PC9 parental cell line cell grows distinctively before and after targeted therapy, and in each case, cells exhibit a wide range of proliferation rates (see details in Chapter 6). In our simplified two-state tumor model, we categorize cell sublines into either sensitive or resistant category based on their drug response. Without targeted therapy, we assume that all the cell lines grow logistically, which explains a fast exponential growth at low confluency and a slow proliferation at high confluency. Under targeted therapy, cell lines either follow the same logistical growth as they were without targeted therapy (we call these cells resistant to targeted therapy), or they go through apoptosis following the exponential decay (we call these cell lines sensitive). We use equation 3.1 to represent this differentiation among tumor cells.

$$N_T = N_R + N_S \tag{3.1}$$

Where N_T is the total number of cells, N_S is the number of cells categorized as sensitive phenotype, and N_R is the number of cells categorized as resistant phenotype.

It's found both of tumor cell proliferation rates with and without targeted therapy are heterogeneous and span close to a continuous spectrum (see details in Chapter 6). Thus the growth of cell mixtures can be described by the summation of all the individual cell lines. For all sensitive phenotypes under drug treatment, we can capture the total sensitive phenotype's growth as a summation of all sensitive cell lines with corresponding exponential decay rates, as shown in Equation (3.2) and (3.3)

$$N_S = \sum_{j=1}^{n_s} N_S^{(j)} \tag{3.2}$$

$$\frac{\partial N_S^{(j)}(t)}{\partial t} = k_{S,d}^{(j)} N_S^{(j)}(t) \tag{3.3}$$

Where *Ns* is the total sensitive cell number, $N_S^{(j)}$ is the individual sub cell line at corresponding decaying rate $k_{S,d}^{(j)}$.

Correspondingly, for resistant phenotype under drug treatment, we can capture the total resistant phenotype's growth as a summation of all resistant cell lines with corresponding logistic growth rate, see Equation (3.4) and (3.5)

$$N_R = \sum_{i=1}^{n_r} N_R^{(i)} \tag{3.4}$$

$$\frac{\partial N_R^{(i)}(t)}{\partial t} = k_{R,p}^{(i)} N_R^{(i)}(t)(1 - \frac{N_T(t)}{\theta}) \tag{3.5}$$

Where N_R is the total resistant cell number, $N_R^{(i)}$ is the individual sub cell line with corresponding growth rate $k_{R,p}^{(j)}$.

We simplify the multiple phenotypes model to a two state model, where each tumor tissue, even the individual cell lines involved may have distinct growth rates or death rates, can be described as two phenotypes grow or decay at averaged rate. That is, still following the conservation in (3.1), the growth of all sublines can be simplified to only two variables and two parameters, see Equation (3.6) and (3.7).

$$\frac{\partial N_S(t)}{\partial t} = k_{S,d} N_S(t) \tag{3.6}$$

$$\frac{\partial N_R(t)}{\partial t} = k_{R,p} N_R(t)(1 - \frac{N_T(t)}{\theta}) \tag{3.7}$$

3.1.2 Simulation validation

To further demonstrate the rationale of our approach, we compare the growth curve of the summation of ten individual growth curves with distinctive growth rate and that of one growth rate. As for sensitive cell lines' drug response, we first generate 10 individual drug response curves with the decay rate ranging from -0.035/day to -0.08/day with -0.005/day interval. Each of the sublines has an initial cell number of 0.07θ. In Figure 3.1 (1), we show those drug response curves with distinct colors, and faster decaying curve corresponds to the smaller decay rate. We then use the summation of all the ten curves to fit into Equation (3.6) using *MATLAB* build-in function *lsqnonlin()*. We obtain a single decay rate of -0.547/day, meaning the optimized decay rate of the simplified model. As shown in Figure 3.1 (2), the summation of the individual response curves (black) and the response curve generated from the simplified model are nearly identical, indicating the validity of our hypothesis. In summary, sensitive phenotype that is composed of 10 distinct sensitive cell lines at decaying rate ranging from -0.035/day to -0.08/day can be described as one phenotype at decay rate -0.0547/day.

As for resistant cell lines that grow logistically under drug treatment, we first generate 10 individual drug response curves with the growth rate ranging from 0.015/day to 0.06/day with 0.005/day interval. Similarly, each of the sublines has an initial cell number of 0.07θ. In Figure 3.1 (3), we show those drug response curves with distinct colors, and faster growing curve corresponds to the larger growth rate. We then again use the summation of all the ten curves to fit into Equation (4.7) using *MATLAB* build-in function *lsqnonlin()*. We obtain a single decay rate of 0.038/day, which is the optimized growth rate of the simplified model. As shown in Figure 3.1 (4), the summation of the individual response curves (black) and the response curve generated from the simplified model are again nearly identical. In summary, resistant phenotype that is composed

of 10 distinct sensitive cell lines at growth rate ranging from 0.015/day to 0.06/day can be described as one phenotype at growth rate 0.038/day.

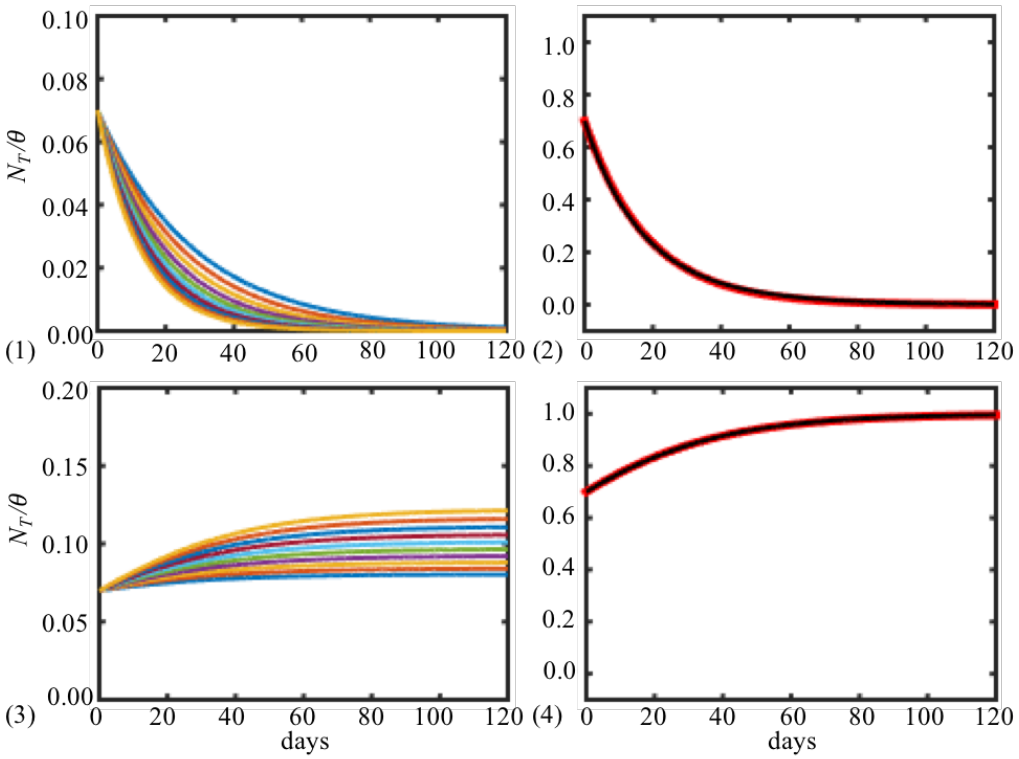

Figure 3.1 (1) A series of ten sensitive tumor drug response curves following exponential decay at rate ranging from -0.035day^{-1} to -0.08day^{-1}. (2) Comparison between summation of all curves in (1) (black) and one tumor response curve following exponential decay at rate -0.0547day^{-1} (red). (3) A series of ten resistant tumor drug response curves following logistic growth at rate ranging from 0.015day^{-1} to 0.06day^{-1}. (4) Comparison between summation of all curves in (1) (black) and one tumor response curve logistic growth at rate 0.038 day^{-1} (red).

3.2 Single phenotype tumor progression in space – origin and application

We can easily extend ODE models described in 3.1 into PDE model of higher dimension (1D, 2D

and 3D) by adding a spatial interaction term. As described in Chapter 2, one of the most widely used models to account for the expansion of tumor in continuum space (macro) is diffusion, and in discrete space (micro) is random walk [90]. The first study of random walk and diffusion equation dates back to 1827 when Robert Brown observed under microscope the random motion of pollens suspended in water. Such observation is later explained by random walk model, which states each molecule at every given moment has equal probability to move one step towards any possible direction. Using statistical method, one found that the probability of distance traveled by single molecule after a period of time is Gaussian distributed, and the standard deviation of such distribution is proportional to the square root of time. On the macro scale, such Gaussian distribution can be explained by Fick's law. The Fick's first law states solute molecules move from high concentration region to low one, with a flux proportional to the concentration gradient (see Equation 3.8).

$$J(x) = -D\frac{\partial \Phi(x)}{\partial x} \tag{3.8}$$

where $J(x)$ is the flux, $\Phi(x)$ is the solute molecules' concentration, D is the Diffusion Coefficient, and x is the spatial coordinate. Constraining the first law by mass conservation, Fick's second law states that change of concentration of the solute molecules in time is proportional to its second spatial derivative (see Equation 3.9).

$$\frac{\partial \Phi(x,t)}{\partial t} = D\frac{\partial^2 \Phi(x)}{\partial x^2} \tag{3.9}$$

We apply the continuum diffusion model to the single phenotype cell growth in space. For simple demonstration, we take 1D model as an example, see Equation 3.10.

$$\frac{\partial N(x,t)}{\partial t} = D\nabla^2 N(x,t) + f(N(x,t)) \tag{3.10}$$

Where *N(x,t)* is the cell density as a function of time and space, *D* is the diffusion coefficient, and *f(N(r,t))* is the function related to cell number change through natural growth, drug response or both. When the tumor tissue density is heterogeneous, cells migrate along the density gradient at rate positively correlated with *D*.

This diffusion term can be used to reproduce tumor tissue's morphological changes over time. As shown in Chapter 2, reaction diffusion equations have been applied in cancer modeling for more than two decades. It effectively captures the tumor spheroid growth in 3D [60], explains the tumor metastasis[61] and more recently matches the morphological evolution observed in clinical imaging[9, 10, 57, 58].

3.3 Multi-phenotypes tumor progression in space

For mixed phenotypes growing in space, the first intuitive approach is to model each species as independent to each other, such as what has been done previously by other groups [50, 52, 53, 61], see Equation 3.11 and 3.12.

$$\frac{\partial N_1(x)}{\partial t} = D\nabla^2 N_1(x,t) + f_1(N_1, N_2, x) \tag{3.11}$$

$$\frac{\partial N_2(x)}{\partial t} = D\nabla^2 N_2(x,t) + f_2(N_1, N_2, x) \tag{3.12}$$

Where each cell phenotype migrates along its own density gradient. However, it ignores the factor that cell's migration is restricted by the occupation of space from other phenotypes as well. Indeed,

cell random walk in space is rather different from molecule random motion in solute. According to the hard sphere model, the packing fraction of ideal gas is approximately zero, that of liquid ranges from zero to 0.494, and that of solid is above 0.494. Note the packing ratio of random spheres, similar to that of cells packing in space, is close to 0.638. Thus the random motion of cells in space is more similar to solid rather than liquid. The assumption that multi-phenotype cells migration in space in the way of ideal gas/ liquid will overestimate the extent of mixing (the depth of penetration into another phenotype) between species.

Another intuitive approach that attempts to damp the speed of diffusion is to assume the original diffusion term to be constrained by the ratio of each species of total cells, as shown in Equation 3.14 and 3.15

$$N_T(x,t) = N_1(x,t) + N_2(x,t) \tag{3.13}$$

$$\frac{\partial N_1(x)}{\partial t} = \frac{N_1}{N_T} D\nabla^2 N_T(x,t) + f_1(N_1, N_2, x) \tag{3.14}$$

$$\frac{\partial N_2(x)}{\partial t} = \frac{N_2}{N_T} D\nabla^2 N_T(x,t) + f_2(N_1, N_2, x) \tag{3.15}$$

Or similarly, one assumes that the second derivative of the diffusion term is constrained by the ratios of each species of total cells.

$$\frac{\partial N_1(x)}{\partial t} = D(\nabla \frac{N_1}{N_T} \nabla N_T(x,t)) + f_1(N_1, N_2, x) \tag{3.16}$$

$$\frac{\partial N_2(x)}{\partial t} = D(\nabla \frac{N_2}{N_T} \nabla N_T(x,t)) + f_2(N_1, N_2, x) \tag{3.17}$$

However, both of the above two approaches failed the mass conservation test in our simulation, and more fundamentally lack rigorous rationale.

Similar subject to multi species interaction has been identified by ecologists[91], and we take inspiration from modeling work by Burger et al [92] on population dynamics, where interactions of species are ubiquitous (eg. the predator and prey relation), and the spatial spread of multiple species in ecological system are similar to that of cells in microenvironment. On the micro level, the model suggests the probability of one specie's migration to an adjacent space is proportional to the density at its local position, and the empty space in adjacent space.

$$P_i^+ \infty N_i \cdot (1-(\sum_{j=1}^{n} N^+{}_j / \theta) \tag{3.18}$$

Where P_i^+ is the probability of migration into positive (arbitrary) direction for species *i*, N_i is the number of species *i*, N^+_j is the number of species *j* in adjacent location at the positive direction, θ is the largest density allowed for all species.

Based on the described principal above, the derived diffusion term for two species system take the form:

$$\frac{\partial N_1(x)}{\partial t} = D((1-\frac{N_T(x,t)}{\theta})\nabla^2 N_1(x,t) + \frac{N_1}{\theta}\nabla^2 N_T(x,t)) + f_1(N_1, N_2, x) \tag{3.19}$$

$$\frac{\partial N_2(x)}{\partial t} = D((1-\frac{N_T(x,t)}{\theta})\nabla^2 N_2(x,t) + \frac{N_2}{\theta}\nabla^2 N_T(x,t)) + f_2(N_1, N_2, x) \tag{3.20}$$

Compared to the first model (Equation 3.14 and 3.15), in regions where tumor tissue density reach confluency-- that is when N_T is approximated to θ —both the first and second term on the right side of the equation have low values—meaning limited migration. In this model, the limited

migration is irrespective of heterogeneous distribution of any single species, while in the first model, cell migration is only correlated with the spatial heterogeneity of that specific species.

3.4 Summary of the chapter

In this chapter, we described and justified our simplified two state tumor model to capture tumor cells' drug response to targeted therapy. We also introduced an application of size-exclusion diffusion model to cell-cell spatial interactions. In later chapters, we will demonstrate how to combine these ODEs and PDEs model with clinically available imaging for early detection of resistance to drug response.

4. DETECTING RESISTANCE FROM SERIAL MR IMAGES

In chapter 2, we presented that medical imaging is not only beneficial for physicians to diagnose and monitor tumor treatment, but also is rising as an invaluable none-invasive tool that allows researchers to build the tumor models that captures both tumor drug response and morphological changes. In this chapter, we use tumor models introduced in chapter 3 to simulate clinical tumors assayed by medical imaging. We demonstrate how medical available imaging, such as diffusion-weighted MRI, coupled with mathematical models of tumor drug response can be used as a powerful tool to achieve early detection of drug resistance and predict tumor drug response from early course of neo-adjuvant therapy.

4.1 DW-MRI

Central to the methodology we propose is the ability to obtain reasonable estimates of cell number as both a function of space and time. Fortunately, MRI methods have been developed to obtain estimates of cell density *in vivo*. Diffusion weighted MRI (DW-MRI) relies on the phenomenon that water molecules in tissues constantly undergo random Brownian motion and diffuse at a rate that is dependent on tissue microstructure. The rate of water diffusion within tissues measured by conventional MR methods are often summarized in terms of an apparent diffusion coefficient (ADC), which is a measure of the effective distance over which water can migrate within tissue within a specified time.

It has been shown that the ADC decreases linearly with cell volume fraction [93] and cell density [94-96]. Thus, one can write:

$$ADC(\vec{r},t) = ADC_w - \lambda N(\vec{r},t) \quad (4.1)$$

where $ADC(\vec{r},t)$ is the measured ADC at position r and time t, ADC_w is the ADC of free water (normally taken to be ~2.8×10^{-3} mm^2/s at 37°C) [97], λ is a scale factor that (most likely) depends on tumor type, and $N(\vec{r},t)$ is the total number of tumor cells at position r and time t. Yankeelov's Lab has previously employed ADC measures of tumor density in simulations [98], pre-clinical [99] and clinical efforts [100] [59]. In the next session, we will detail the estimation of DW-MRI associated noise level as it is central to the effectiveness or methodology.

4.2 Noise of DW-MRI

Due to the wide application of DW-MR imaging, quantifying the reproducibility of the measurement is an active area of research. Typically, the reproducibility is measured in terms of the variation in signal from repeated test of the same subject. Measurements have been made in humans, animals, and ice-water mixtures[101] [102] [103] [104] [105] . While tests on humans and animals are of more practical value for clinical applications, the test on ice-water has unique advantages in measuring DW-MRI's intrinsic noise. For example, ice-water stays at constant temperature around 0 C^0, and is resilient to environmental changes due to water's high heat capacity and the latent heat of solidification. A commonly used parameter to quantify the effect of noise is the coefficient of variation (c_v), often expressed in percentages, and equal to the ratio of the standard deviation δ to the mean μ [101] [102] [103] [105] [106]:

$$c_v = \frac{\sigma}{\mu} \times 100\% \quad (4.2)$$

In the DW-MRI studies, the c_v is used to evaluate the mean *ADC* of tissue ROI (2D region of

interest) or VOI (3D volume of interest). In 2013, Malyarenko et al[105] tested reproducibility of *ADC* value of ice-water phantom on 35 DW-MRI scanners, and found the intra-exam c_v to be less than 1%, and the inter-scanner c_v to be less than 2%. In 2014, Yankeelov's group [104] expanded the test to 11 female mice HER2+ breast xenografts, and found that within tumor ROI c_v to be around 5%[106]. Later, Grech-Sollars *et al* [101] tested the DW-MRI reproducibility of multiple brain regions on 9 healthy adults. They reported the intra scanner VOI c_v of 1.7% and 2.1% for white and grey matter respectively, and the inter scanner VOI c_v of 1.5% for ice-water phantom. Another group[102] conducted tests on 17 solid tumors on children under the age of 16, and found VOI c_v of 3.25%. In summary, *ADC* c_v of ice water phantom falls below 2%, and *ADC* VOI c_v of *in vivo* tissues is between 1.5% and 3.5%, and registered VOI c_v is generally less than the ROI c_v [103] .

For each of the above experiments, the ROI or VOI contained several voxels. Less known is the c_v on the single voxel level. Because of the nature of the MRI signal (unlike the light based imaging technique, MRI related measurements are obtained after the Fourier transformation of received signals), there is no obvious relation between noise level and the number of voxels included in each measurement. However, the noise on the single voxel level is critical for the computational study presented later in the chapter. Thus we analyzed an empirical measure of noise level in a single voxel using sets of scans on an ice-water phantom prepared by Jennifer Whisenant in Thomas Yankeelov's lab at Vanderbilt University. Images were acquired with a single-shot spin echo planar imaging sequence in three orthogonal diffusion encoding directions (x, y and z), with two b values (50 and 600 s/mm^2). The in-plane field of view is 192mm x 192mm on a 96 x 96 matrix with 5mm thickness slice.

(1)

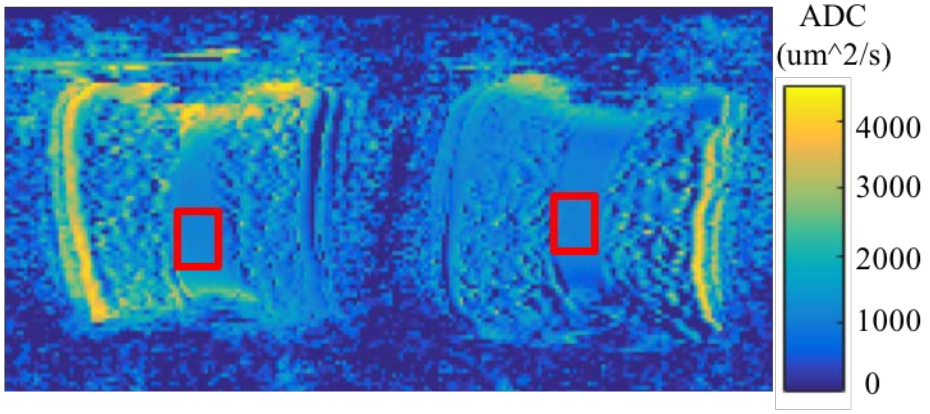

(2)

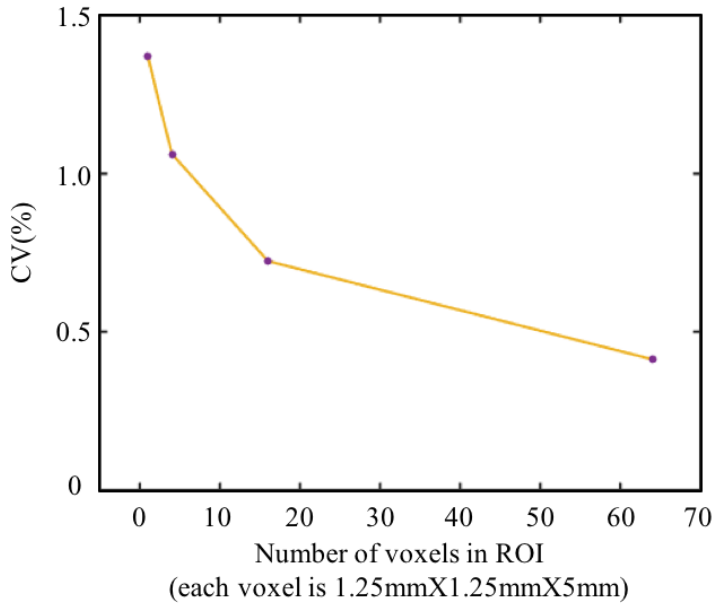

Figure 4.1 (1) representative slice of ADC map for two ice water tubes placed in a breast coil. The red boxes, chosen for their homogeneous signal denote ROI over which coefficient of variation is calculated. (2) The coefficient of variation (c_v) as a function of size of selected ROI.

To determine the c_v, we focus on ROIs extracted from four exams of two water tubes surrounded by ice each set inside a breast coils (Figure 4.1 A). Two VOIs of dimension 10mm x 10mm x 20mm (8 x 8 x 5 voxels) are selected from each exam, and the c_v are calculated based on aggregated ROI from both breast coils. Since we expect the same ADC value from all the voxels inside each ROI, c_v can be directly determined via Equation 4.2. We find the c_v on the single voxel level to be 1.38% (see Figure 4.1 B). As expected, the coefficient of variance decreases as the number of voxels included increase. Combing the repeatability test from literatures of the overall VOI[101] [102] [104] [105] [106], and our empirical calculation of the single voxel level noise, we'll mainly use the global c_v of 3.3%, with added single voxel c_v of 1.5% as the noise level of the simulated MRI measures in this thesis. Occasionally, we introduce simulation with c_v of 0.7% for comparison purpose.

4.3 Methods to apply mathematical models to DW-MRI for diagnosis—parameter optimization and AIC

We use the models described in Chapter 3 to generate simulated data and determine whether, under experimental conditions, the apoptosis ($k_{S,d}$) and growth ($k_{R,p}$) rates can be accurately extracted, and how early can resistant cells be detected. To predict the overall growth of a mixed phenotype tumor, we begin our study from a 1-D model for tumor growth and response to therapy. In the simulations performed in this session, we set $k_{R,p}$ =0.054day^{-1} and $k_{S,d}$ =-0.028day^{-1}, corresponding to estimated growth and death rate in murine experiment (unpublished experiment from Yankeelov's lab). We use the built-in *MATLAB* function *ode45()* to solve the Equation 3.6 and Equation 3.7. Figure 4.2 (1) displays simulated curves for a 1D two-component tumor model

grown under therapy for a range of initial tumor mixtures (i.e., the relative fractions of the tumor cell population that is resistant).

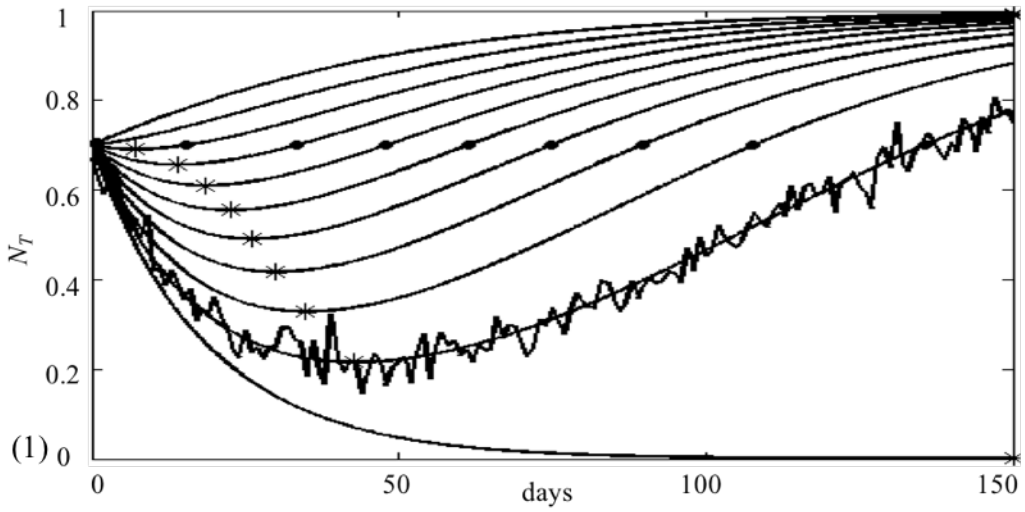

Figure 4.2 Total tumor cell number as a function of time under therapy with kS,p=0.054day-1 and kR,d=0.028day-1. The initial fraction of resistant cells varies from 0% to 100% in 10% increments; asterisk denotes the maximal response time and filled circles the recovery point.

In order to take advantage of the spatial information available from DW-MRI, we generated simulated DW-MR images from Equation 4.3 and Equation 4.4.

$$\frac{\partial N_S(x,y,t)}{\partial t} = D((1-\frac{N_T}{\theta})\nabla^2 N_S(x,y,t) + \frac{N_S}{\theta}\nabla^2 N_T(x,y,t)) + k_{S,p} N_S(x,y,t) \qquad (4.3)$$

$$\frac{\partial N_R(x,y,t)}{\partial t} = D((1-\frac{N_T}{\theta})\nabla^2 N_R(x,y,t) + \frac{N_R}{\theta}\nabla^2 N_T(x,y,t)) + k_{R,p} N_R(1-\frac{N_T}{\theta}) \qquad (4.4)$$

We set θ as the maximal packing of cells in a voxel to be 5435cells/voxel (given a grid size dx = 1.25 mm, dy = 1.25 mm, dz = 4 mm and single cell volume = 1150 μm^3) [107]. We generate a 2D 10×10 grid with 100 voxels that simulate experimentally measured DW-MRI data. The tumor is initially seeded with an average cell number density $N_T(x,y,t_0) = 0.7\theta$. We compare three realizations of the two-component tumor model: 1D tumor, the homogeneous 2D tumor, and the heterogeneous 2D tumor. To generate a heterogeneous distribution of resistant cells, we randomly selected 20 of the 100 voxels within the domain to contain a resistant fraction while keeping the overall $N_T = 0.7\theta$. The fraction of resistance in each of the chosen voxels varies from 5% to 100% at 5% intervals such that the total resistant fraction across all 100 voxels equals 10% of N_T. The system is evolved by finite difference methods with no flux boundary conditions generating simulation for 120 days with a time step of 0.1 day.

To construct the simulated DW-MR images we use the *MATLAB* built-in random number generator *normrnd()* to imitate experimental noise with a mean of 0 and standard deviation of 3.3%*0.7θ (where 0.7θ is the upper bound of the mean cell density) on the overall tumor and 1.5%*0.7θ on single voxels. The noise levels are based on discussion in section 4.2.

To address the accuracy of parameter extraction early in therapy, we sample the noisy images every eight days over a duration of 32, 40, 48, and 56 days respectively. We fit the sampled data using the *MATLAB* function *lsqnonlin()* yielding the tumor growth parameters (i.e., $N_S(t = 0)$, $N_R(t = 0)$, D, $k_{R,p}$, $k_{S,d}$). Finally, we initialize the model with the extracted parameters, evolve the tumor forward in time and compare the model prediction to the original time course. We calculate the difference between the model prediction of $N_T(x,y,t)$ and the original time course and compute

the root mean squared deviation (RMSD) averaged over all voxels. We averaged the resulting RMSD over all model realizations and error bars are the standard deviation about the mean. Parameter distributions, determined from 500 realizations of the noise, are compared to the known values.

To determine how early resistant fractions can be identified, we fit the simulated N_T time course in each pixel to two tumor types: one containing only sensitive cells (i.e., Eq. (3.6)), and the other containing both sensitive and resistant cells (i.e., Eqs. (3.6) and (3.7)).

We apply the Akaike Information Criteria (AIC)[108] to determine which tumor type best describes the temporal evolution of the system. Briefly, given a set of candidate models, the AIC selects the model which best balances goodness of fit with number of free parameters. AIC is computed via:

$$AIC_c = 2m + n\,\mathrm{In}(\frac{RSS}{n}) + \frac{2m(m+1)}{n-m-1} \tag{4.5}$$

where m is the number of parameters, n is the number of observations, and RSS is the residual sum of squares[108]. Thus, a minimum of 6 time points are required to evaluate the AIC for the two-component tumor type. To evaluate which model is most appropriate we compute the likelihood, L, as:

$$L = \exp^{AIC_i - AIC_{\min}} \tag{4.6}$$

where AIC_i is the AIC of the i^{th} model and AIC_{min} is the minimum AIC value for all models considered.

We sample the simulated 2D time course from day 1 to day t_f (t_f = 10, 11, 12, …, 60). We fit the sampled data to the model that contains only sensitive cells and the model that contains both phenotypes. Resistant cells are detected when the two component model is 10 times more likely (as determined by Eq. (4.6) than the model containing only sensitive cells. The AIC evaluation process is repeated 100 times for each condition.

4.4 Parameter extraction from 1D model

We first explore if the tumor growth model parameters may be accurately extracted from noisy DW-MRI images with a limited number of scans. As expected, for tumors containing a mixture of both sensitive and *de novo* resistant cells, N_T initially decreases until the maximal response time (indicated by the asterisk on each curve in Figure 4.2) at which point the growth of resistant cell number first exceeds the decay of sensitive cells. To explore fitting with a limited number of DW-MRI scans, we sample the simulated data every 8th day. Parameter extractions from fitting 1000 noisy realizations (c_v= 0.7% and c_v=3.3% noise) of the 1D tumor growth model with the initial resistant fraction N_{R0} = 10% are displayed in Figure 4.3. As expected, the parameter precision increases as more scans are used to estimate model parameters. When c_v=3.3%, with five scans, 40 days after treatment and well before the tumor shows growth compared to the initial tumor number, 95% of extracted $k_{S,d}$ and N_{S0} parameter values lie within a range from 0.6 to 2 times the actual value. For this tumor mixture, $k_{R,p}$ and N_{R0} parameter extractions are less precise, with 95% of values falling in a range from 0 to 22 times the actual value. Resistance is detected after seven scans (48 days) in 60% of the cases, determined by extracted parameters $N_{R0} > 0.01$ and $k_{R,p} > 0.01$.

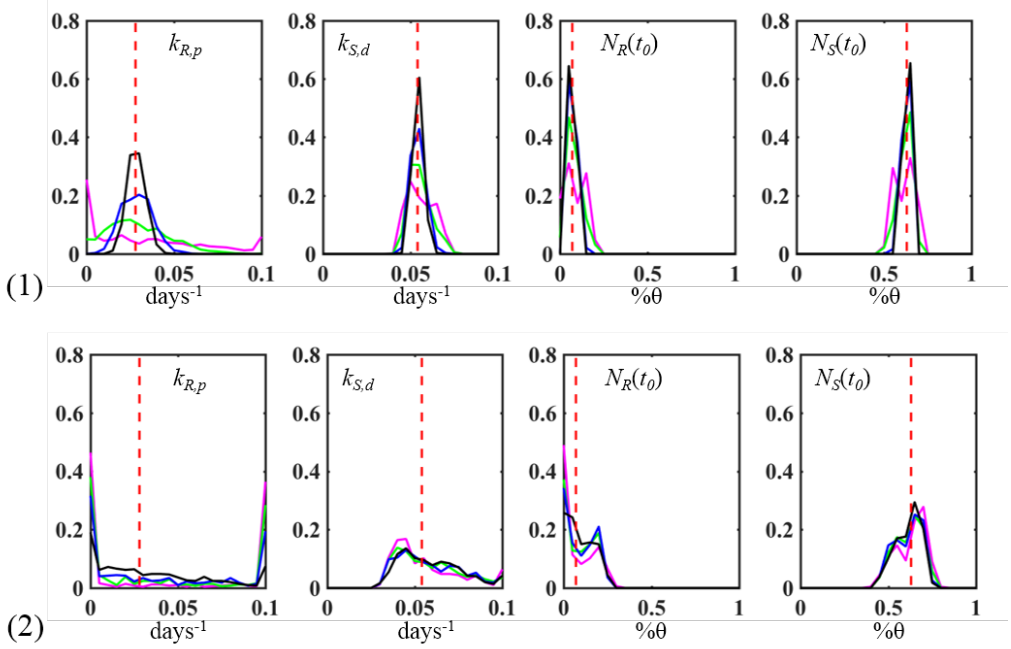

Figure 4.3 Normalized distribution of parameters from 1D model ($k_{R,p}$, $k_{S,d}$, $N_R(t_0)$ and $N_S(t_0)$) with (1) c_v=0.7% and (2) c_v=3.3% respectively. The total cell number data was sampled at 8 day intervals for a total of 32 (magenta), 40 (green), 48 (blue), and 56 (black) days. The red dashed line marks the true parameter value.

We use the extracted parameters to predict the tumor growth at a later time. As expected, the 95% confidence interval for the predicted total cell number increases as the noise level increases from c_v=0.7% to 3.3%, and decreases as the number of sampling before projection increases (see Figure 4.4). Without incorporating the detailed spatial cell density distribution, the prediction at the current clinical imaging noise level (c_v=3.3%) is very poor. More specifically, even when the total tumor cell counts after tumor inflation (day 56) are used for constraining the model, the 95% confidence interval bounds exceeds 150% deviation from the true value by day 80, and the deviation escalates soon after. Thus, such prediction is not valid for evaluating treatment outcomes.

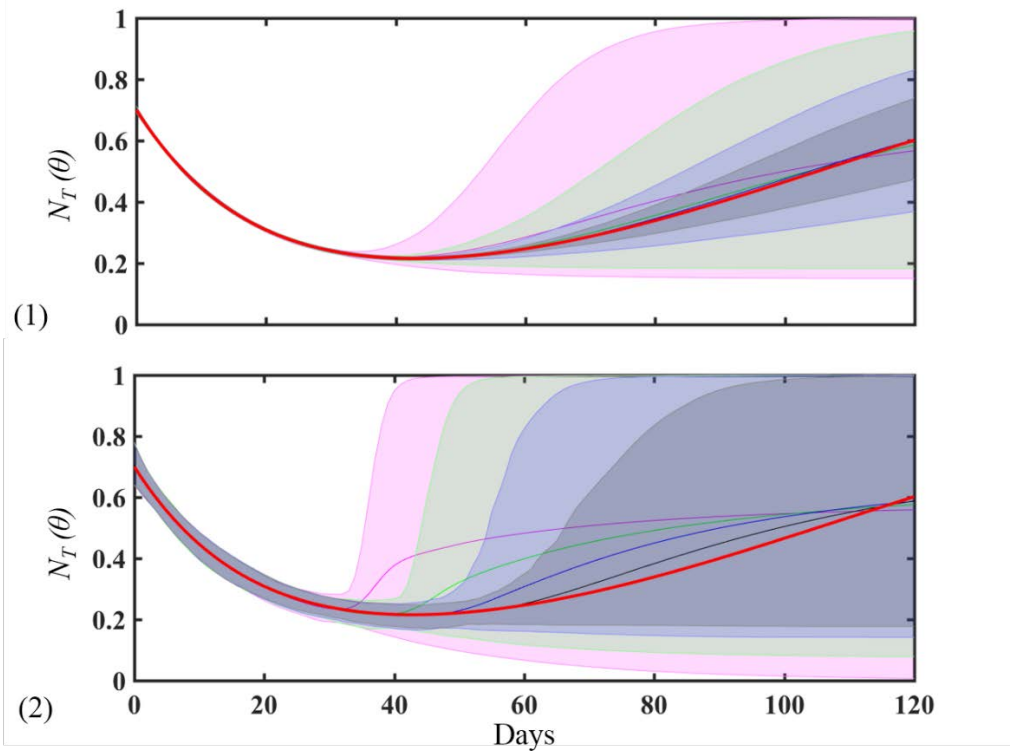

Figure 4.4 The 95% interval of projections of total tumor cell number N_T with simulation noise (1) c_v=0.7% and (2) c_v=3.3% respectively. The projections are made using parameters extracted from sampling at 8 days intervals for a total of 32 (magenta), 40 (green), 48 (blue), and 56 (black) days. The red line marks the true tumor growth.

4.5 Parameter extraction from 2D model spatially homogeneous model

DW-MR images provide N_T measurements on multiple voxels at each time point. Figure 4.3 (2) shows the parameters' density distribution extracted from the two-component tumor model implemented in 2D with the tumor mixture distributed homogeneously in space. The early time points were sampled every eight days and $k_{S,d}$, $k_{R,p}$, $N_S(t_0)$, $N_R(t_0)$, D were extracted. The distributions for the tumor growth parameters for 500 realizations are shown in Figure 4.5 (1). All four extracted parameters show improved precision over the 1D results. For example, for the

sampling span of 40 days, the 95% confidence interval of $k_{S,d}$ and $N_S(t_0)$ shrink to 0.72 and 1.6 times the actual value and $k_{R,p}$ and $N_R(t_0)$ to 0 and 4 times the actual value (see Table 4.1). The peaks in the distribution are shifted due to simultaneously fitting the diffusion constant in the presence of additive noise. Using the criteria for detection of resistance $N_{R0} > 0.01$ and $k_{R,p} > 0.01$, seven 2D scans (48 days) are sufficient to identify resistance in 91% of tumors.

4.6 Parameter extraction from 2D spatially heterogeneous model

We apply similar methodology to spatially heterogeneous tumor model. Figure 4.5 (2) displays simulated 2D DW-MRI maps of cell number density. In this simulation, the "tumor" was initialized with a total 10% of resistant cells distributed randomly across the whole tumor. The tumor growth was simulated in the size-exclusion tumor model (Equation (4.3) and (4.4)). Noise was added to the subsequent images and the early time points were sampled every eight days. With the assumption that $k_{R,p}$, and $k_{S,d}$ are constant in space, spatial heterogeneity in the initial distribution of resistant fraction moderately improves parameter extractions compared to the 2D spatially homogeneous model (Figure 4.5), decreasing the parameter distribution width by a factor of 2 (see Table 4.1). Regions with high initial sensitive cell numbers help constrain $k_{S,d}$ for all fits, leading to more accurate extractions of all four tumor parameters (Table 4.1).

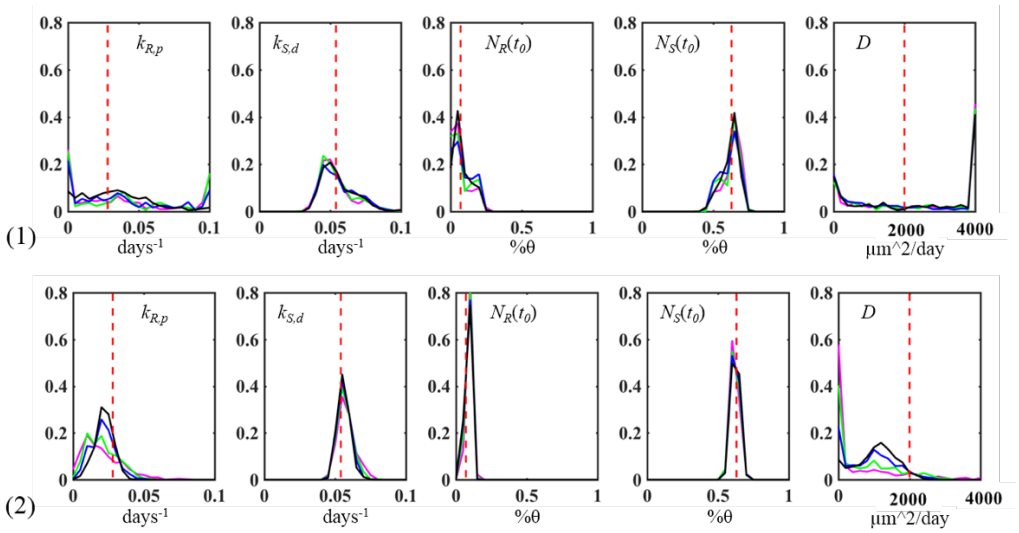

Figure 4.5 Normalized distribution of parameters from (1) 2D homogeneous mode (kR,p, kS,d , NR(t0), NS(t0), and D). (2) 2D heterogeneous model (kR,p, kS,d , NR(t0), NS(t0), and D). The total cell number data was sampled at 8 days intervals for a total of 32 (magenta), 40 (green), 48 (blue), and 56 (black) days. The red dashed line marks the true parameter value.

1D Model	$k_{S,d}$ (median)	$k_{S,d}$ (CI- 95%)	$k_{R,p}$ (median)	$k_{R,p}$ (CI-95%)	N_S (Median)	N_S (CI)	N_R (Mean)	N_R (CI)
	0.054	~	0.028	~	0.63	~	0.07	~
32Days	0.050	0.034, 0.113	0.019	0, 0.867	0.658	0.462, 0.748	0.027	0, 0.248
40Days	0.054	0.033, 0.106	0.023	0, 0.615	0.629	0.469, 0.742	0.075	0.001, 0.233
48Days	0.055	0.034, 0.103	0.026	0, 0.323	0.627	0.466, 0.728	0.076	0, 0.228
56Days	0.0562	0.033, 0.102	0.0264	0, 0.146	0.629	0.468, 0.722	0.075	0.001, 0.231

2D Uniform Model	$k_{S,d}$ (median)	$k_{S,d}$ (CI- 95%)	$k_{R,p}$ (median)	$k_{R,p}$ (CI-95%)	N_S (Median)	N_S (CI-95%)	N_R (Median)	N_R (CI-95%)	D (Median)	D (CI-95%)
	0.054	~	0.028	~	0.63	~	0.07	~	2000	~
32Days	0.051	0.038, 0.087	0.031	0, 0.1	0.65	0.48, 0.71	0.04	0.01, 0.22	3261	0, 10000
40Days	0.052	0.039, 0.084	0.037	0, 0.1	0.64	0.49, 0.71	0.05	0.01, 0.22	3081	0, 9887
48Days	0.054	0.038, 0.085	0.031	0, 0.1	0.63	0.49, 0.71	0.06	0.01, 0.21	2439	0, 9675
56Days	0.053	0.038, 0.083	0.032	0, 0.1	0.63	0.49, 0.70	0.06	0.01, 0.21	3088	0, 9523

2D Non-uniform Model	$k_{S,d}$ (median)	$k_{S,d}$ (CI- 95%)	$k_{R,p}$ (median)	$k_{R,p}$ (CI-95%)	N_S (median)	N_S (CI-95%)	N_R (median)	N_R (CI-95%)	D (median)	D (CI-95%)
	0.054	~	0.028	~	0.63	~	0.07	~	2000	~
32Days	0.057	0.048, 0.072	0.017	0,0.055	0.62	0.56,0.67	0.09	0.07, 0.12	40	0, 3080
40Days	0.057	0.048, 0.068	0.019	0.004, 0.043	0.62	0.57,0.67	0.08	0.07, 0.12	401	0, 2639
48Days	0.056	0.049, 0.066	0.021	0.007, 0.040	0.62	0.57,0.67	0.08	0.07,0.11	929	1, 2267
56Days	0.056	0.049, 0.065	0.022	0.008, 0.034	0.62	0.57,0.67	0.08	0.07,0.10	112	5, 2100

Table 4.1 Dependence of the extracted parameter values on the number of scans included in the fit for (1) 1D growth model, (2) a 2D model with N_R and *Ns* initially distributed homogeneously, and (3) a 2D model with N_R and N_S initially distributed heterogeneously. The noise level added to the simulated data was 3.3% of noise. 2D models were solved via the constrained diffusion method. Fitting 2D data vs. 1D data decreases the number of scans required for narrow 95% confidence intervals, however fitting D causes an overall shift in the extracted values.

When we use the extracted parameters to predict the tumor growth later, the 95% confidence interval for the predicted total cell number decreases significantly as the initial seeding density changes from homogeneously distributed to heterogeneously (see Figure 4.6). This illustrates that the high resolution MR imaging's capability of capturing cell density variation would aid the property diagnosis of the tumor of interest.

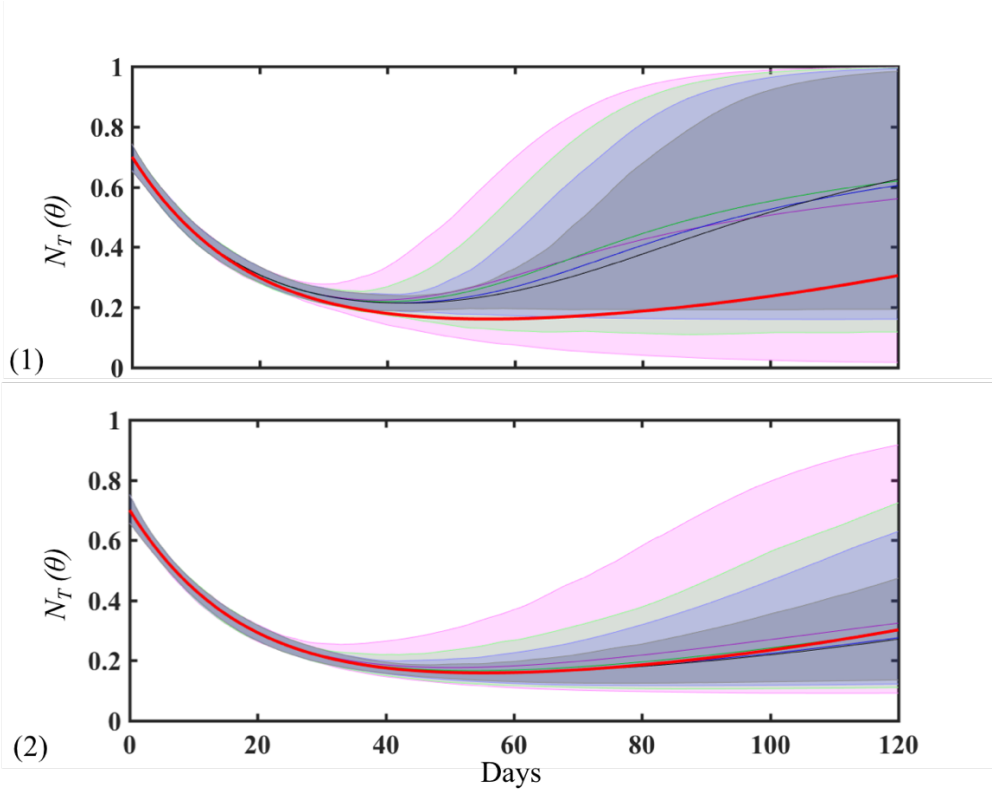

Figure 4.6 The 95% interval of projections of total tumor cell number, N_T, with (1) homogeneous and (2) heterogeneous resistant phenotype seeding. Similar to Figure 4.4, projections are made using parameters extracted from sampling at 8 days intervals for a total of 32 (magenta), 40 (green), 48 (blue), and 56 (black) days. The red line marks the true tumor growth.

We use the extracted parameters to seed the above 2D model. We then evaluate the model from 0 to 100 days and compare to the original time course, and iterate the process for 500 times to estimate the stochasticity caused by clinical level sampling noise. Figure 4.7 (1) shows the forward projection for the spatial distribution of resistant phenotype for high signal-to-noise scans. Figures 4.7 (2) and 4.7 (3) display comparisons between the true and projected N_T time course for two voxels with low (voxel 1) and high (voxel 2) initial resistance fraction.

Overall, the extracted model quantitatively captures the growth and spatial expansion of the resistance phenotype. For tumor voxel 2 (highlighted in Figure 4.7 (2) and Figure 4.7 (3)) that contains high percentage of initial resistance phenotype, the projection of tumor growth fits well within desired range, where the 95% confidence interval yields less than 8% deviation from true value by Day 100. However, for tumor voxel 1, where the initial resistance phenotype ratio is low, the projection yields more than 25% deviation. This indicates the accuracy of local tumor growth projection depends on the phenotype composition of local cells and that of neighboring cells. As cell density information from all sub regions are aggregated and utilized to derive the diagnosis of the overall tumor, the overall prediction out-performs the one that utilizes only the total tumor cell counts, even at 4 times more noise.

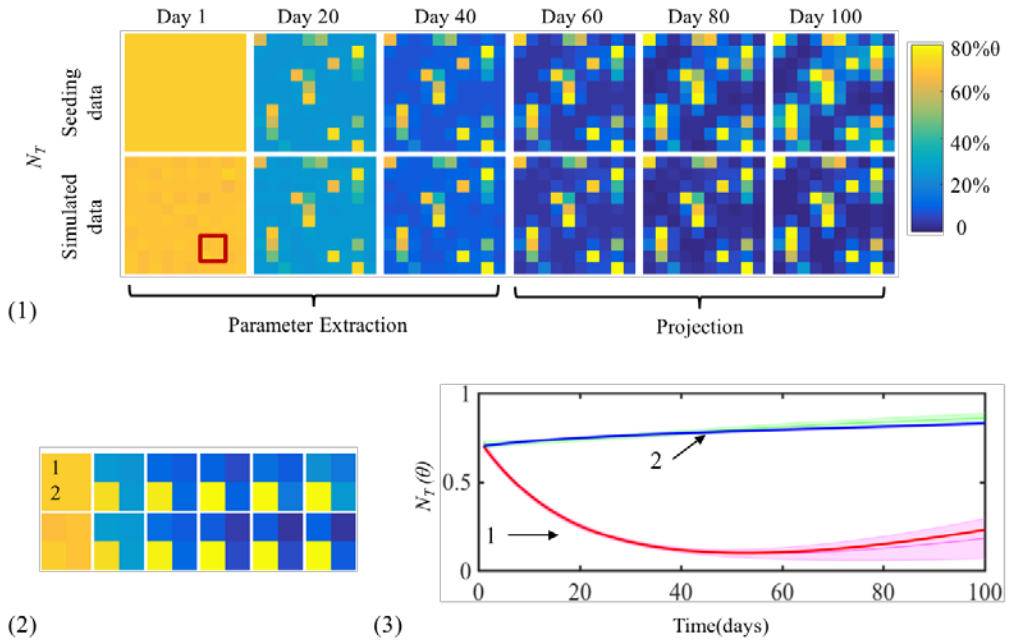

Figure 4.7 (1) (Top) Simulated $N_T(t)$ maps without additive noise. The simulation is initiated with a 10% initial resistant fraction distributed randomly across the field. Six different time points are shown. Simulated data with added noise is sampled every 8th day during the first 48 days. Voxel specific composition and overall tumor growth parameters are extracted and used to project the subsequent evolution of $N_T(t)$. (2) Magnified regions indicated by red box in (1). (3) Time course comparison of two voxels with low (voxel 1) and high (voxel 2) initial resistance fraction. Blue and red solid lines are corresponding to the value from true underlying model, and the green and magenta shades are the 95% confidence interval of the projections.

4.7 Early detection of the resistant phenotype

We next investigated whether statistical methods comparing serial imaging to two simple tumor models could accelerate the detection of a resistant fraction. We define the minimum day resistance can be detected as the point where a two-component model (Equation (3.6) and (3.7)) becomes 10 times more likely than a single component model (Equation (3.7) only). Figure 4.8 (1) summarizes

these results from the 1D model by plotting the log2 likelihood as a function of time after the initiation of therapy. Once each curve advances above the horizontal red line (at which point, L>10 in Equation (4.6)), resistance has been identified. In the inset, we indicate how the time to diagnose resistance increases with decreasing initial fraction of resistant cells and decreasing sampling frequency. For tumors that are sampled (i.e., imaged with DW-MRI) each day, and contain 10% or more resistant cells, the resistant phenotype may be detected within 24 days of the initiation of treatment—a factor of two shorter than the maximal response time. Due to the requirement of having sufficient observation numbers, at least six for a four parameter fit, the earliest detection time point increases with lower sampling frequencies. For example, sampling a 10% tumor every eight days detects resistance within the same time frame as model fitting, after 48 days.

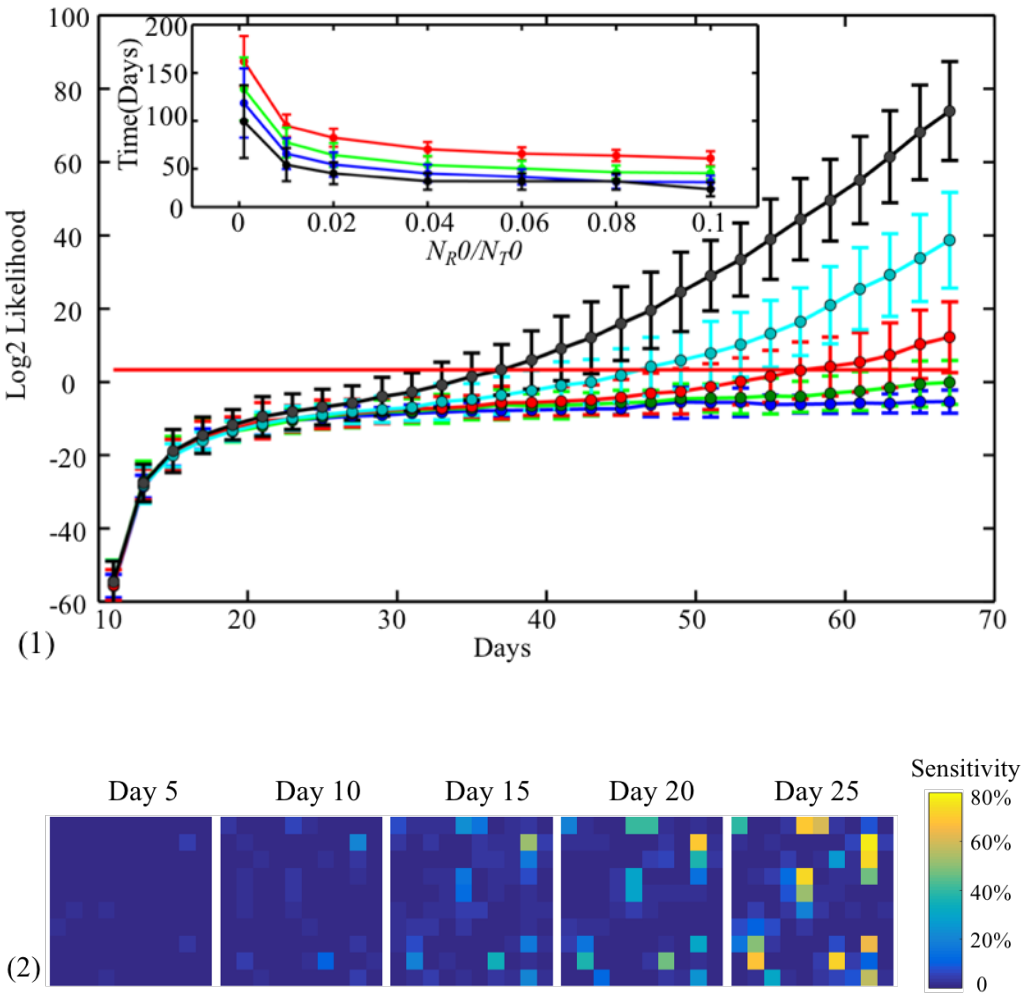

Figure 4.8 (1) The likelihood that a 1D tumor contains a resistant fraction as a function of measurement time and initial fraction of resistant cells. The bold horizontal red line denotes the confidence threshold ($\log_2 10$) for identifying resistance. The minimum time needed to identify resistance as a function of initial resistant fraction using AIC criteria (Insert). The four lines represent tumors sampled at different frequency of every 1, 2, 4 and 8 days. (2) The sensitivity of each pixel from 2D MR images to be identified as containing resistant phenotypes through the AIC criteria.

As expected, the time for identifying resistance increases as the initial resistant fraction decreases; for example, for a tumor with an initial population of 4% resistant cells, it takes 52 days to identify resistance if measurements are acquired every eight days. We note that at these detection times, the total tumor cell number is well below the initial tumor cell number. Assuming symmetric and compact tumor growth, such that tumor volume $V \sim N_T^3$, the RECIST criteria[46] would identify the tumor as progressive after the total cell number had increased beyond the initial cell number, > 136 days for the 10% initial resistant fraction (Figure 4.2).

We next apply the AIC to determine the presence of the resistant phenotype using the 2D information from a spatially heterogeneous simulated tumor. Figure 4.8 (2) shows the voxel based sensitivity for detecting the presence of a resistant fraction for the 10% tumor shown in Figure 4.7 (1), as we increase the daily samples from 5 days to 25 days. As early as 20 days of observation, several voxels indicate the highly likely presence of a resistant fraction. By 25 days, most regions with initial resistance seeding were detected with high likelihood using AIC. The heterogeneous distribution of resistance in the 2D tumor leads to local regions with high initial resistant fractions reducing the time required to detect resistance via the AIC criteria. Currently, imaging based methodologies for assessing the effectiveness of cancer therapies is based on high-resolution MRI or X-ray computed tomography measurements of the change in tumor size during therapy. In particular, the RECIST criteria[46] considers the change in the longest dimensions of "target" lesions before and after therapy and then places each patients' response into one of four pre-defined bins: 1) complete response (disappearance of all target lesions), 2) partial response (>30% decrease in the sum of the target lesions' diameters), 3) progressive disease (>20% increase in the sum of the target lesions' diameters), and 4) stable disease (none of the above). By incorporating spatial information of a MR image and applying AIC criteria, we can substantially enhance our ability to

identify resistant populations from early course of therapy. Compared to RECIST criteria[46], we assume that a solid tumor grows symmetrically and that the tumor volume is reflective of the number of tumor cells, $V \sim N_T^3$ and maximal dimension $R \sim N_T$. With this assumption, the method presented here identifies tumors containing a fraction of resistant cells well before the tumor increased in size, potentially outperforming RECIST[46] by several weeks.

4.8 Summary of the chapter

In this Chapter, we first introduce the use DW-MR imaging to measure tumor cell density distribution, and investigated the associated noise of such measure. We demonstrate how to apply those measurements to obtain estimate of tumor characteristics through 1D and 2D tumor models. The estimation accuracy increases as we increase the resolution and frequency of measurements, and introduce heterogeneity in the tumor.

Overall, we have presented a proof of principle study to use quantitative, noninvasive, and clinically obtainable imaging data to detect the presence of a resistant cell fraction. Given serial imaging data within the current noise standards, the methodology can detect resistance substantially earlier than current standard-of-care methods. In addition, the method may be applied to testing mathematical descriptions of tumor growth and response to therapy for *in situ* tumors.

5. EXAMINING THE TUMOR MIXING MODELS IN 2D

In Chapter 3, we motivated two possible models for the mixing and spread of a two component tumor, containing sensitive and resistant phenotypes. In Chapter 4, we explored whether such a two component tumor could be identified through DW-MR imaging and found that if the growth rates under therapy are significantly different then DW-MR imaging can determine the presence of resistance well before current clinical standards. As discussed, DW-MRI is only sensitive to total cell number, and the change in cell number over time is sensitive to all the parameters in the model, so DW-MRI is insufficient to determine which mixing model is most appropriate. In this chapter, we present an experimental effort, based on fluorescence microscopy, aimed to determine whether the free diffusion or the constrained diffusion model is most appropriate for tumor mixing in 2D layers. While examination of the cell scale fluorescence images does provide some support for the constrained diffusion model, global fitting to the data finds the two models produce equally poor RMS deviations from the data. We find that the resistant cell type shows much greater spread than the sensitive cell type, that the diffusion constant describing the spread of resistant cells decreases with cell density, and that the conversion from cell number to carrying capacity also depends on cell phenotype.

5.1 Experiments to test the candidate diffusion models

To experimentally test the efficacy of the diffusion model with size exclusion introduced in Chapter 3, we designed an experimental system that allowing observation of cell mixing process

of two phenotypes. Such experiments fill in the vacancy in the current literature to directly address the spatial interaction of multiple phenotypes.

5.1.1 Cell lines and cell culture

We use BR1 cell line and one discrete sublines DS9 for PC9 parental cell line obtained from Vito Quaranta lab (Vanderbilt University). The BR1 cell line is known for its resilient growth with or without erlotinib treatment. In contrast, DS9 is the most sensitive sublines to erlotinib among the PC9 sub cell line.

Both cell lines are fluorescently labeled with FUCCI (fluorescence ubiquitin cell cycle indicator) marker using lentivirus-mediated transduction [78]. FUCCI is a set of fluorescent probes: Fucci-G1-Orange that contains a fragment of human Cdt1 and Fucci-S/G2/M-Green that contains a fragment of human Geminin. The expression of Cdt1 and Geminin take turns to reach peak through each cell cyle, with Cdt1 during G1 phase and Geminin during S/G2/M phase.

Additionally, the BR1 and DS9 cell lines are labeled with CellTracker^{TM} Blue (Life Technologies) and CellTracker^{TM} Red (Life Technologies) fluorescent dyes respectively to allow differentiation from one another under fluorescent microscope. CellTracker^{TM} Red and Blue are molecular probes that once pass through cell membranes into cells can be retained in living cell cytoplasma for several generations.

Both cell lines were cultured in CO_2 (5%), temperature (at 37°C) and humidity controlled incubators. Before use, the cells were confirmed to be negative for mycoplasma using MycoAlert PLUS kit (Lonza). Cells were cultured in RPMI 1640 media supplemented with 10% FBS (Atlanta Biologicals) and Antibiotic/Antimycotic mix (Gibco). During imaging, the media was substituted

for OPTI-MEM media (Gibco) supplemented with 2% FBS and Antibiotic/Antimycotic mix to reduce background auto-fluorescence.

5.1.2 Experimental design

To observe the diffusion and mixing process of two cancer cell phenotypes, we design the experiment that initially cultures the two cell phenotype at close proximity, but separated. To observe the rate of mixing, we remove the barrier and image over time. We place a silicone insert (Ibidi Insert Family) of approximately 6mm in width with a defined cell-free gap into the middle of a 2cm by 2cm well. We culture inside the left chamber of the insert BR1 cells with cyan florescent protein labeled in the cytoplasma, and place DS9 cells with red florescent protein labeled inside the right chamber. Both cell lines are labeled with Histone B RGP at the nuclei. After each cell line grows to the desired density, we remove the Ibidi insert and image multiple times over 14 days. Given the size of the inserts and the well, and assuming the inserts are placed in the middle of the well, it leaves about 7mm width of empty space on both end of the well. Right after removing the insert, both cell phenotypes occupy a 3mm wide space, and are separated by a gap of width 0.5mm (see Figure 5.1 for the illustrated scale and placement of BR1 and DS9 cell lines).

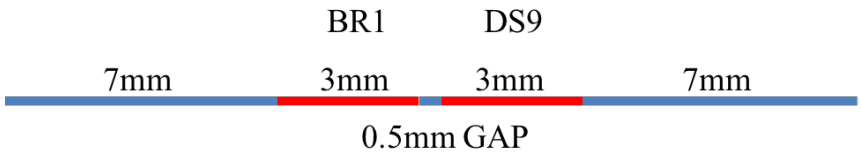

Figure 5.1 Illustration of the experimental set up's scale, and the corresponding BR1 and DS9 cell line placement.

Cells are seeded at three density levels before removal of the inserts ($7x10^5$ cells for well 1, $7x10^6$ cells for well 2, and $2.1x10^7$ for well 3), and recorded by epifluorescent imaging daily. Figure 5.2 (1), 5.3 (1), and 5.4 (1) shows the experimentally observed growth and cell mixing for three different initial seeding levels. Each image is a coarse grained composite, consisting of 78x34 pixels with each pixel equivalent to 60μmx60μm in space. We set up multiple replicates with three initial plating densities. Cells were allowed to adhere for 24 hours, then the inserts were removed and the cells were imaged. Each imaging window was 258μm x 258μm, and we acquired multiple images at 20X resolution that were subsequently stitched for future analysis. The image collection was repeated for 14 consecutive days, except for day 6 and day 13.

5.1.3 Expected outcome

Based on our experimental setup and the previous knowledge of our cell lines, we parameterize both diffusion models to evaluate the expected outcome from the experiments. We set the initial seeding density for the two cell lines both as 10% of the carrying capacity, BR1's growth rate $k_{R,p}$ as 0.6 day^{-1}, DS9's growth rate $k_{S,p,}$ as 0.35 day^{-1}, BR1's diffusion Rate D_R as 3000 μm^2/day, and DS9's diffusion rate D_S as 300 μm^2/day. As shown in Figure 5.2, by 14^{th} day of experiment, we expect to see significant wider expansion of the BR1 into DS9's region from independent diffusion than from size-exclusion diffusion.

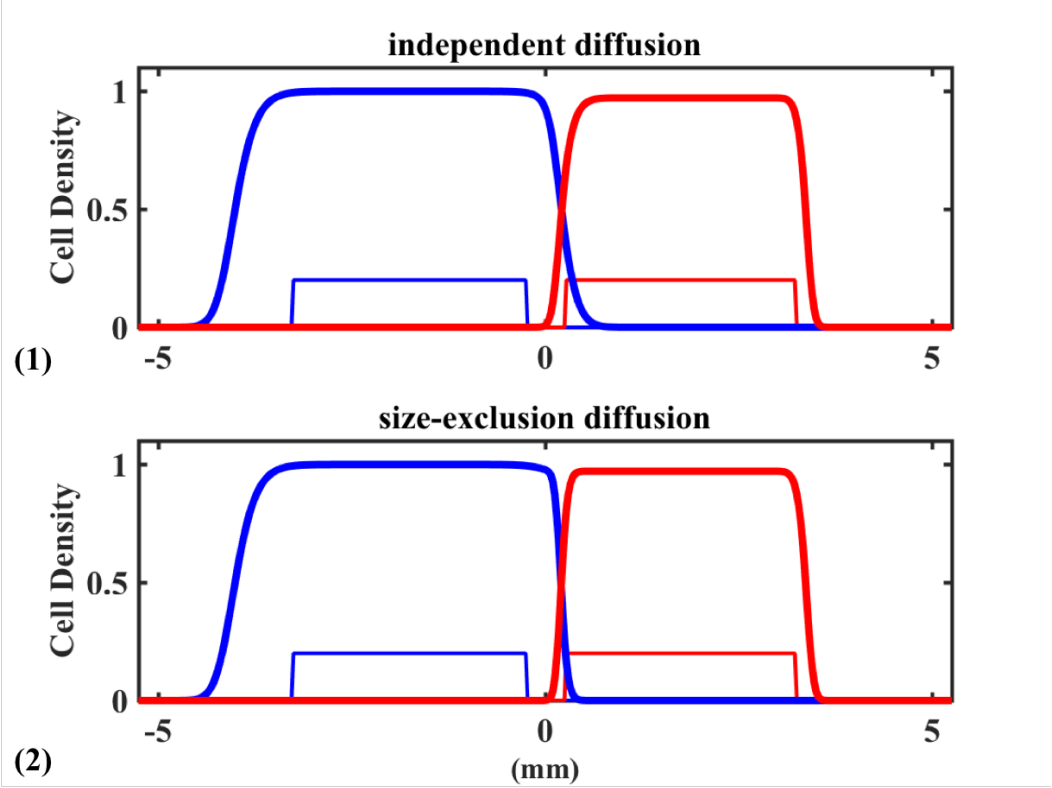

Figure 5.2 Expected 1D outcome of cell growth and diffusion in 14 days based on independent diffusion (1) and size-exclusion diffusion (2) model respectively. The thick lines are the outcome at 14th day, and the thinner lines are the initial seeding. Blue lines represent the BR1 cell line with blue cytoplasma, and red lines the DS9.

5.1.4 Conversion from average intensity to cell counts

The stitched images provide a day-to-day record of the intensity in each pixel in both the red, green, and blue channels. To compare to the model predictions, we need to map fluorescence intensity to cell density. As the background intensity varied from day to day, we first scaled all channels by their maximum then set the total dynamic range to be from 0 to 256. As both cell types have red fluorescence in the Nuclei, we followed the following procedure to account for each cell line's density:

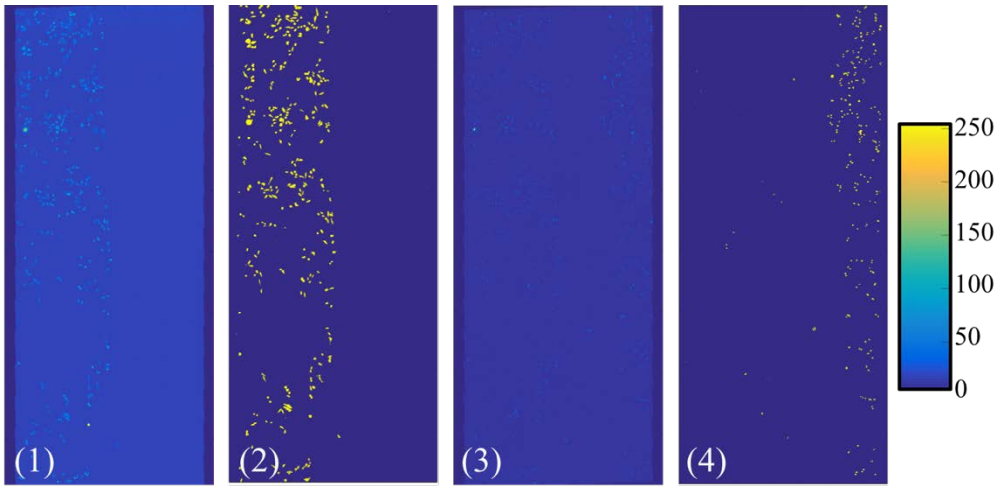

Figure 5.3 (1) Raw image from blue channel. (2) Binary mask created for blue cytoplasma BR1 cells. (3) Raw image from red channel of the same well (4) Binary mask created for red cytoplasma DS9 cells.

(1) Set the red channel threshold. The DS9 cells (sensitive) have both the nuclei and cytoplasm labeled to emit fluorescence in the red channel, but no label to strongly emit fluorescence in the blue channel. To distinguish DS9 cells, we divide the red channel intensity by the blue channel intensity and find regions in the image that are greater than a threshold, typically 2.0. The actual values varied for each stitched images.

(2) Set the blue channel threshold. The BR1 cells cytoplasm is labeled such that it fluoresces in the blue channel. Blue cells are then identified by being above a threshold intensity in the blue channel and the ratio of red intensity to blue intensity being significantly less than for a sensitive cell (typically < 1.0). The actual values varied for each stitched images.

(3) Correct for the background. Background pixels may past both filters, such that if a pixel was found true for both the red mask and the blue mask, it was removed from either mask. Care was taken by the user to choose the threshold such that dim cells were not dropped from day to day and

that cells clearly identified as either red or blue in the time points before and after the current image remained identified as red or blue in the current image.

(4) Set the conversion of nuclei intensity in the blue channel. Used a *MATLAB* script to identify the nuclei in 10 randomly chosen 100 by 100 portions of each stitched imaging multiplied by the blue mask. The sum of the red intensity over all 10 count of all 10 determined the conversion from intensity to cell number. The red channel multiplied by the red mask was treated similarly. We checked the error in this by choosing 10 other random regions from each stitched imaging and comparing the human counted cell number with the cell number from intensity conversion.

5.1.5 Error of cell counts

We summarize the error analysis for cell counts in Figure 5.4. For regions where the number of cells are clearly identifiable, we show how the conversion matches a hand count. The two cell counts are strongly correlated with correlation coefficient (CC) equal to 0.93. The first degree linear model fitting returns an intercept of 0.59 and slope 1.13, and the r-square is 0.87. The average intensity conversion method has a mean 24% deviation from human identification. As the cells become denser, and possibly grow out of the plane, the above method is also subject to increased error in cell count by the user.

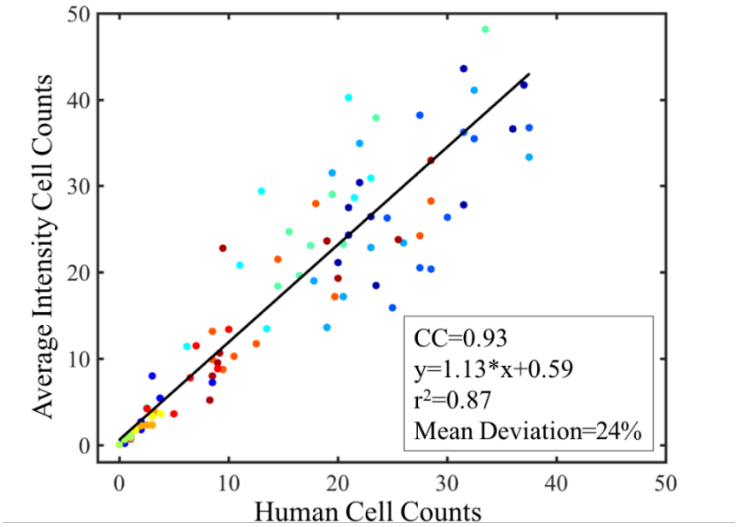

Figure 5.4 Comparison between human cell counts and cell counts from average intensity conversion method. Points sharing the same color denotes regions from the same stitched image. The correlation coefficient (CC) of the two counts is 0.93, and linear correlated with r-square value of 0.87.

5.2 Parameterization for the two models

In the above described experiment, as there is no drug treatment, we assume both BR1 and DS9 follow logistic growth. Thus, we replace Equation 4.14-4.15 and Equation 4.19-4.20 with Equation 5.1-5.2 and Equation 5.3-5.4.

$$\frac{\partial N_R(x,y,t)}{\partial t} = D_R \nabla^2 N_R(x,y,t) + k_{R,p} N_R(x,y,t)\left(1 - \frac{N_T(x,y,t)}{\theta}\right) \tag{5.1}$$

$$\frac{\partial N_S(x,y,t)}{\partial t} = D_S \nabla^2 N_S(x,y,t) + k_{S,p} N_S(x,y,t)\left(1 - \frac{N_T(x,y,t)}{\theta}\right) \tag{5.2}$$

$$\frac{\partial N_R(x,y,t)}{\partial t} = D_R((1-\frac{N_T}{\theta})\nabla^2 N_R(x,y,t) + \frac{N_R}{\theta}\nabla^2 N_T(x,y,t)) + k_{R,p} N_R(x,y,t)(1-\frac{N_T}{\theta}) \quad (5.3)$$

$$\frac{\partial N_S(x,y,t)}{\partial t} = D_S((1-\frac{N_T}{\theta})\nabla^2 N_S(x,y,t) + \frac{N_S}{\theta}\nabla^2 N_T(x,y,t)) + k_{S,p} N_S(x,y,t)(1-\frac{N_T}{\theta}) \quad (5.4)$$

Where N_R is the cell density of resistant BR1 cell line, N_S of the sensitive DS9 cell line, D_R and D_S diffusion rate, and $k_{R,p}$ and $k_{S,p}$ the growth rate respectively for the two cell lines.

From examination of the experimental images, we find that single cell size differs between BR1 and DS9. In an ideal 2D environment, the carrying capacity θ should be inversely proportional to cell's projection area on the 2D surface. Thus, cells of different phenotype with different cell size will yield different carrying capacity θ_R and θ_S.

$$\theta_R = \eta / A_R \quad (5.5)$$

$$\theta_S = \eta / A_S \quad (5.6)$$

Where $\eta = 0.9069$ is the packing fraction for 2D circles, A_R the 2D area of BR1 and A_S that of DS9.

The overall percentage occupancy of space ranging from 0 to 1 (thus, θ is normalized to 1), and the normalized N_T should be the sum of percentage occupancy of both phenotypes, hence

$$N_R / \theta_R = N_R * A_R / \eta \quad (5.7)$$

$$N_S / \theta_S = N_S * A_S / \eta \quad (5.6)$$

$$N_T = N_R * A_R / \eta + N_S * A_S / \eta \quad (5.9)$$

Substitute 5.7-5.9 into Equation 5.1-5.4, and take

$$\kappa = A_S / A_R \quad (5.10)$$

$$\gamma = \eta / A_R \quad (5.11)$$

we arrive at for the independent diffusion:

$$\frac{\partial N_R(x,y,t)}{\partial t} = D_R \nabla^2 N_R(x,y,t) + k_{R,p} N_R(x,y,t)(1 - \frac{N_R + \kappa N_S}{\gamma}) \quad (5.12)$$

$$\frac{\partial N_S(x,y,t)}{\partial t} = D_S \nabla^2 N_S(x,y,t) + k_{S,p} N_S(x,y,t)(1 - \frac{N_R + \kappa N_S}{\gamma}) \quad (5.13)$$

and for the size exclusion diffusion:

$$\frac{\partial N_R}{\partial t} = D_R((1 - \frac{N_R + \kappa N_S}{\gamma})\nabla^2 N_R + N_R \nabla^2(\frac{N_R + \kappa N_S}{\gamma})) + k_{R,p} N_R((1 - \frac{N_R + \kappa N_S}{\gamma})) \quad (5.14)$$

$$\frac{\partial N_S}{\partial t} = D_S((1 - \frac{N_R + \kappa N_S}{\gamma})\nabla^2 N_S + N_S \nabla^2(\frac{N_R + \kappa N_S}{\gamma})) + k_{R,p} N_S((1 - \frac{N_R + \kappa N_S}{\gamma})) \quad (5.15)$$

We combine Equation 5.12-5.15 and the three sets of 2D time series image of cell growth find optimal values for BR1's growth rate $k_{R,p}$, DS9's growth rate $k_{S,p,}$, BR1's diffusion Rate D_R, DS9's diffusion rate D_S, the cell size ratio κ, and carrying capacity γ of BR1. To optimally rule out the experimental noise, we drop certain days of experimental images based on overall image intensity normality and regional normality. As a result, 11 images from Well 1 and Well 2 respectively, and 8 images from Well 3 are selected for model parameterization. We use first available day of images as initial condition, and use *MATLAB* build in function *lsqnonlin()* for optimization.

5.3 Comparison of the two models

In experimental setup, both BR1 and DS9 cells lines' nuclei are labeled with red fluorescent protein. In addition, the BR1 cytoplasm is labeled with CFP and can be observed through the CFP dichroic; the DS9 cytoplasm is labeled with red fluorescent protein and can be observed through the RFP dichroic set. We use the previously described method to convert light intensity to cell number, and used the obtained cell density distribution for each cell lines to fit into tumor growth

model. For illustration purpose, in order to increase the contrast in the merged image of BR1 and DS9 density distribution, we use red color to mark the DS9 cell line, and the green to mark the BR1 cell line. The comparison between experiment and simulation of the two models are shown in Figure 5.5, 5.6, and 5.7. We hand drew the fronts of both cell lines, and marked the longest migration position in each horizontal direction where the cell density is at least 5 cells per pixel. Both models qualitatively capture the growth and spatial expansion of the two phenotypes, though the detailed density feature is lost in both models.

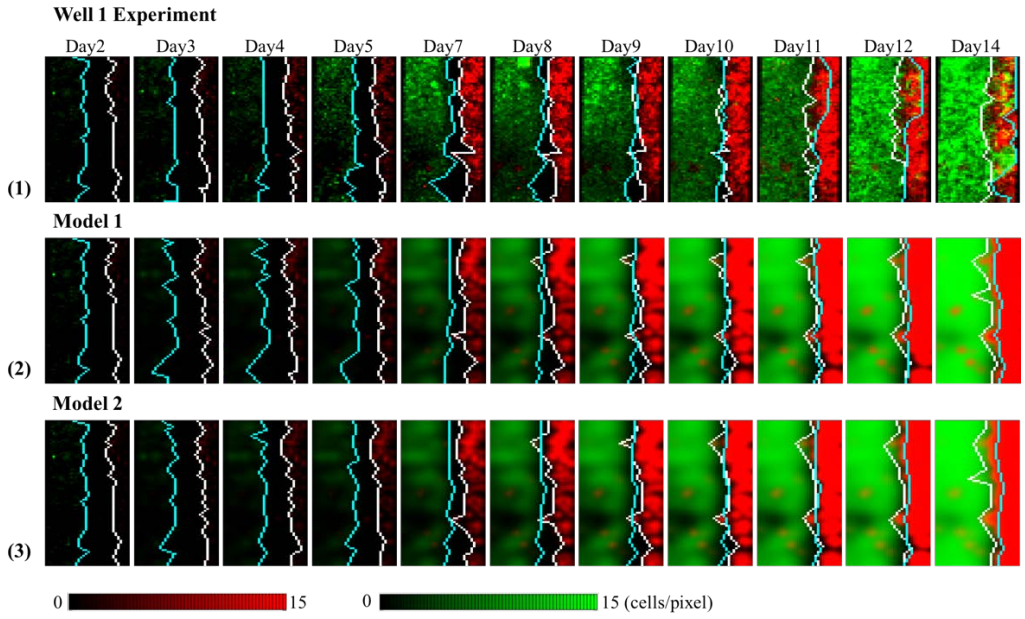

Figure 5.5 Experimental images recorded at well 1 and the corresponding simulations. (1) 2D time series of BR1 and DS9's growth. BR1 is highlighted in green and DS9 highlighted in red. (2) Simulation of the BR1 and DS9 using the size exclusion diffusion model. (3) Simulation of the BR1 and DS9 using the independent diffusion model. Cyan lines are the hand drawn fronts of BR1(green) cells, and the white lines are the hand drawn fronts of DS9 (red) cells. Each image is 4.68mm in height and 2.04mm in width.

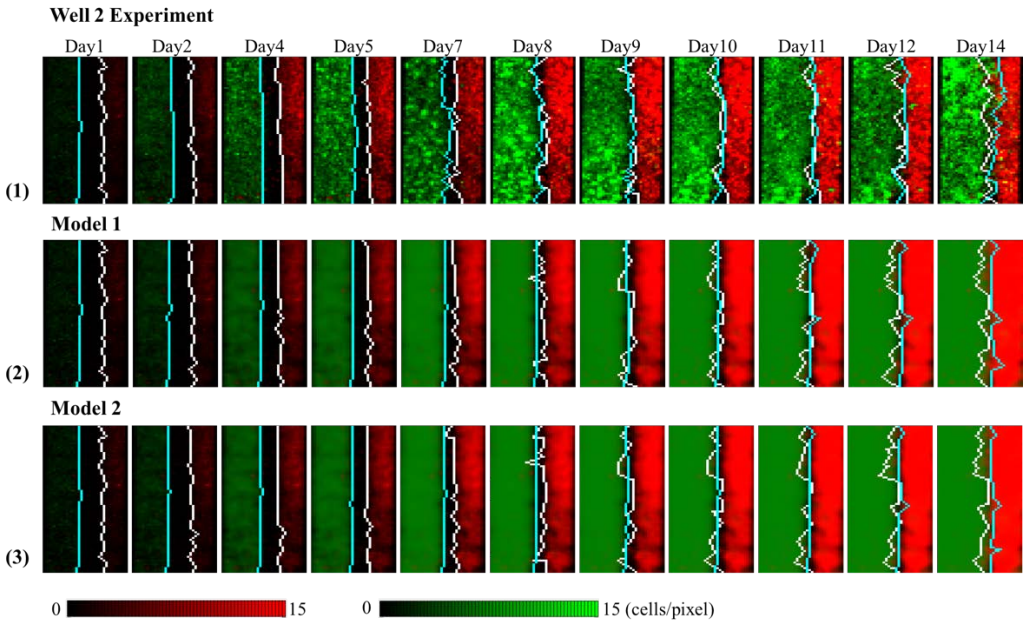

Figure 5.6 Experimental images recorded at well 2 and the corresponding simulations. (1) 2D time series of BR1 and DS9's growth. BR1 is highlighted in green and DS9 highlighted in red. (2) Simulation of the BR1 and DS9 using the size exclusion diffusion model. (3) Simulation of the BR1 and DS9 using the independent diffusion model. Cyan lines are the hand drawn fronts of BR1(green) cells, and the white lines are the hand drawn fronts of DS9 (red) cells. Each image is 4.68mm in height and 2.04mm in width.

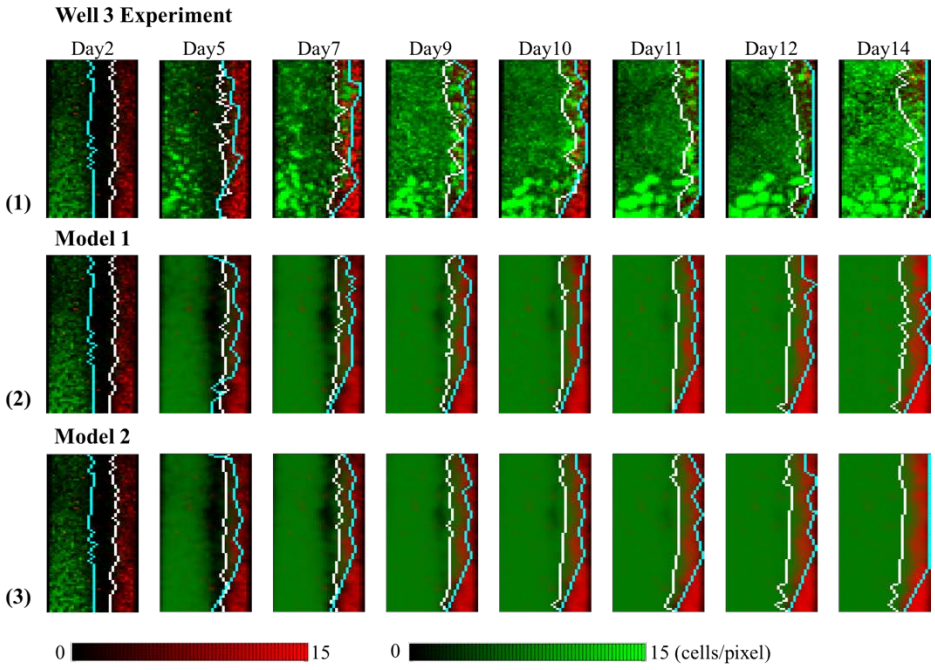

Figure 5.7 Experimental images recorded at well 3 and the corresponding simulations. (1) 2D time series of BR1 and DS9's growth. BR1 is highlighted in green and DS9 highlighted in red. (2) Simulation of the BR1 and DS9 using the size exclusion diffusion model. (3) Simulation of the BR1 and DS9 using the independent diffusion model. Cyan lines are the hand drawn fronts of BR1(green) cells, and the white lines are the hand drawn fronts of DS9 (red) cells. Each image is 4.68mm in height and 2.04mm in width.

In Figure 5.8, we show the root mean squared deviation (RMSD) of the two models from the experimental observation. The RMSD was determined by a voxel by voxel subtraction of the best fit model prediction from the observed cell counts, the results were squared and the mean determined from the entire snapshot. For all wells in observation, the two models have overlapping deviation for the first 9 days. The independent diffusion model performs slightly better at long times, however the difference in the overall RMSD residuals are all less than 2%.

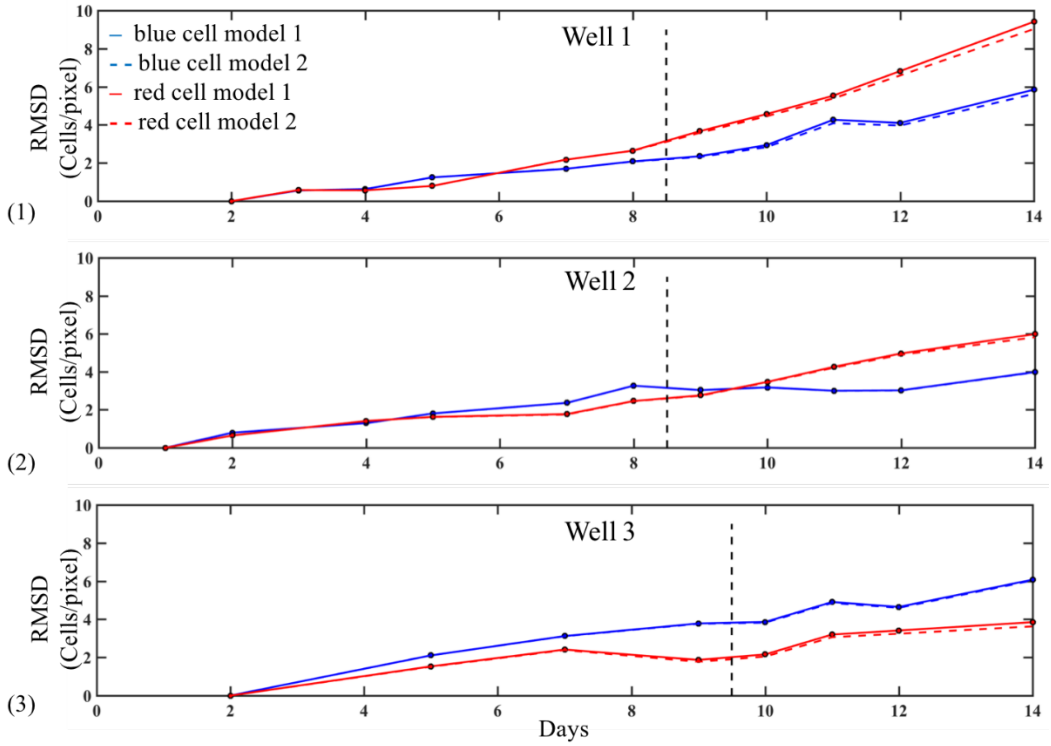

Figure 5.8 Root mean squared deviation (RMSD) between the model prediction and experimental observation. The solid blue line shows the RMSD of model 1 blue fluorescent cell BR1, the dashed blue line shows the RMSD of model 2 BR1, the solid red line of model 2 red fluorescent cell DS9, and the dashed red line of model 1 DS9. Measurements before date specified by the black dashed line are used for parameter extraction and measurements after are used for prediction and observation comparison.

We also quantify the difference between the model estimated location of the cell propagation fronts and the experimental observed location (see Figure 5.9). The difference between model estimation and experimental observation has no consistent bias. Positive mean difference represents that model predicted cell propagation is faster than experimental observed propagation. Negative mean difference represents that model predicted cell propagation is slower than experimental observed propagation Both tumor models tend to overestimate the propagation of DS9 cell line, and

underestimate that of BR1. As expected, standard deviation of the difference tends to increase in later days of experiment.

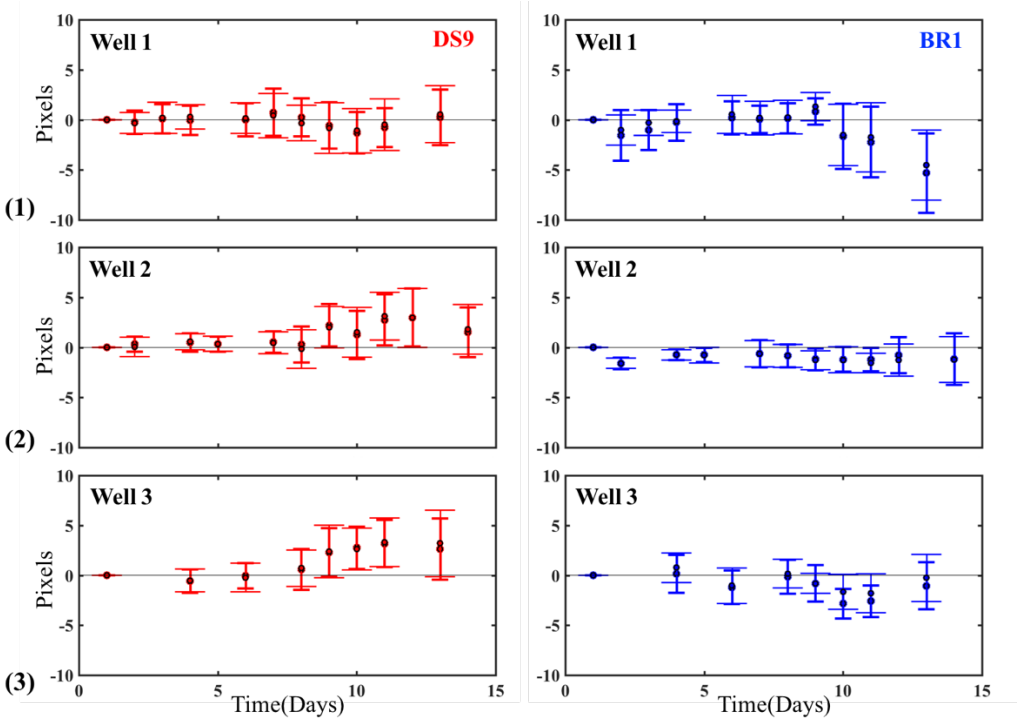

Figure 5.9 Error bar of difference between model estimated fronts location and experimental observed one in (1) Well 1, (2) Well 2, and (3) Well 3 respectively. Red error bars correspond to the DS9 cell line, and blue error bars to the BR1.The thick and short error bars correspond to the size exclusion model, and thin and long error bars correspond to the independent diffusion model.

From examination of the cell count data, we find two surprising features – the sensitive cells do not advance, and they grow to higher density. Such observations are reflected in the optimized

parameters summarized in Table 5.1: (1) the 2D size ratio κ (A_S/A_R) is consistently estimated to be less than 1, especially in well 3, it is estimated to be 0, meaning no constraint for the DS9 cells as they can potentially expand vertically to the third dimension. (2) The diffusion rates of resistant cells are 10, 20, and 1.5 times larger than the sensitive cells in well 1, well 2, and well 3 respectively. As the initial seeding density increases from well 1 to well 3, the estimated diffusion rate decreases monotonically.

	Well 1		Well 2		Well 3	
	Model 1	Model 2	Model 1	Model 2	Model 1	Model 2
$k_{R,p}$ *(/day)*	0.56	0.56	0.74	0.74	0.58	0.59
$k_{S,p}$ *(/day)*	0.67	0.70	0.37	0.38	0.01	0.01
D_R *(μm^2/day)*	5019	6600	1401	1646	335	304
D_S *(μm^2/day)*	637	481	79	61	271	215
γ *(cells/pixel)*	10.5	10.8	7.4	7.3	7.3	7.2
κ	0.85	0.87	0.39	0.39	0.00	0.00

Table 5.1 Summarized optimal parameters for experiment conducted in Well 1, Well 2 and Well 3 using both size exclusion diffusion (Model 1) and independent diffusion (Model 2).

Finally, we use Akaike Information Criteria (*AIC*) to determine the likelihood of these two models. We calculate a set 27 relative AIC (AIC2-AIC1) values through using subset of image series. For example, well 1 has in total 11 eligible images for parameter fitting, we choose a subset of first two to first eleven images for each relative AIC calculation, and end up with 10 relative AIC values

for well 1. We then plot the 27 relative AIC values against the ratio of overlapping area of for the two phenotypes in the image of last day (see Figure 5.10). We find that when the ratio of overlapping area is less than 0.025, the relative AIC values can be both positive and negative, with no strong preference toward either model. However, when the ratio of overlapping is larger than 0.025, the relative AIC becomes definitely negative, favoring the independent diffusion model.

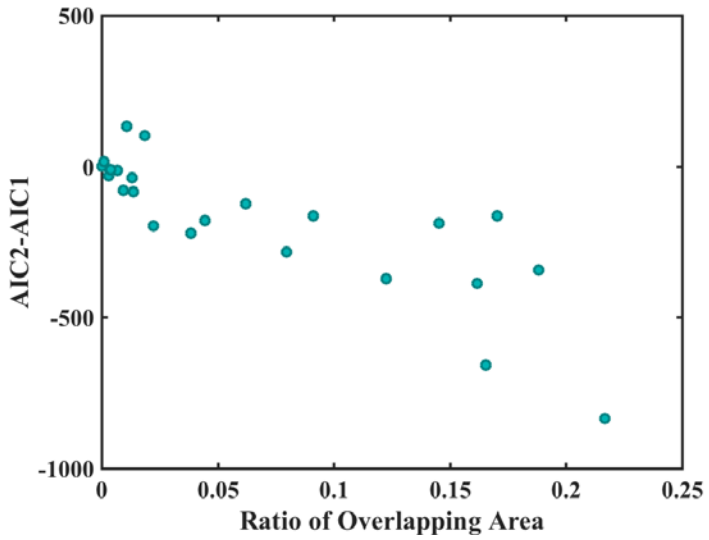

Figure 5.10 The relative AIC (AIC2-AIC2) as a function of ratio overlapping Area for 27 sets of experimental image series.

As the diffusion coefficient of BR1 is significantly larger than that of DS9, the overall fitting suggests, as the two phenotypes merge together into shared space, BR1 would grow into space occupied by DS9 with limited restriction. However, when we zoom in selected area in Well 2, we find that the initially closely seeded BR1 and DS9 tend to grow around each other and not

overlapping (see Figure 5.11). The size exclusion diffusion model captures such growth pattern more closely to the experiment than the independent diffusion model.

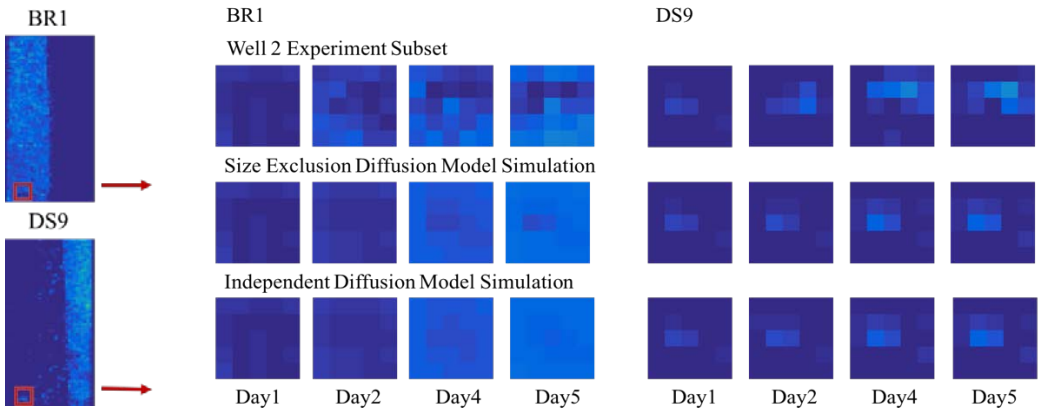

Figure 5.11 Subsets of BR1 and DS9's growth pattern time series comparison between the experiment and the two models from Day1 to Day5.

As the two models are indistinguishable based on our current sets of experiment, we explore the two models' influence on the framework proposed in chapter 4. The simulations are set up similar to methods and initial conditions described in section 4.3 for the heterogeneous model with a few exceptions. We use Equation 5.12 and Equation 5.13 for the independent diffusion, and Equation 5.14 and Equation 5.15 for size exclusion diffusion. We also choose D_R =2000 μm^2/day, D_R =300 μm^2/day, κ =0.40 based on the experimentally estimated values from this chapter. We first simulated the MRI measures assuming the true tumor growth model is the size exclusion model, and add experimental noise described in chapter 4. We apply the first 48 days of generated images

with an interval of 8 days to both models and find that the two models' RMSD for a duration of 80 days are nearly identical (Figure 5.12).

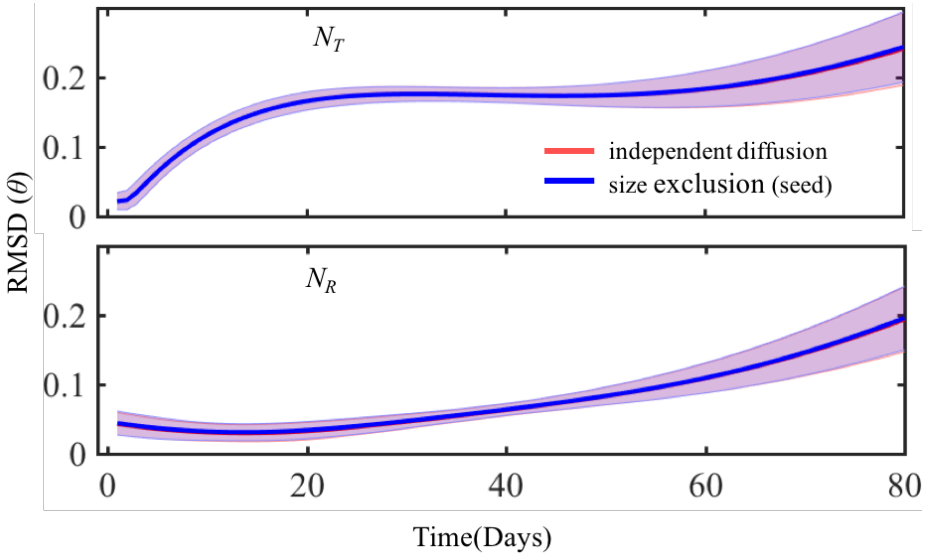

Figure 5.12 RMSD for N_T and N_R of the two models based on images generated from size exclusion diffusion model. Red lines and error bars correspond to the fitting from independent diffusion model, and blue correspond to size exclusion model.

Conversely, we simulate the MRI measures using independent diffusion model, apply them to the two models and find the same result (Figure 5.13). Our simulation indicates the influence of experimental noise exceed the influence of model difference. Under the current medical imaging condition, these two models are exchangeable.

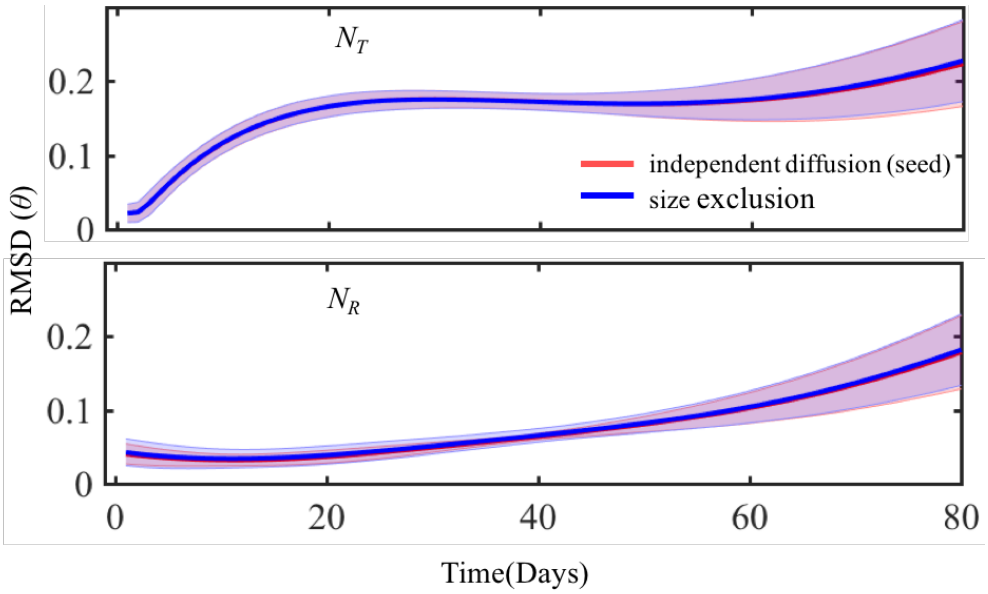

Figure 5.13 RMSD for N_T and N_R of the two models based on images generated from independent diffusion model. Red lines and error bars correspond to the fitting from independent diffusion model, and blue correspond to size exclusion model.

5.4 Summary of the chapter

In this chapter, we present a set of 2D experiments based on fluorescence microscopy to test the efficacy of the two tumor mixing models outlined in chapter 3. We find that resistant and sensitive cells diverge both in carrying capacity and diffusion constant. The sensitive phenotype reaches higher cell density compared to the resistant phenotype, and the resistant phenotype spreads and mixes faster than the sensitive phenotype often by an order of magnitude. Although we find supporting evidence for the size-exclusion model through local microscopic examination, there is no significant advantage for either model from global parameter fitting. Under the noise level of current DW-MR imaging condition, these two models are exchangeable.

6. CELLS IN MICRO ENVIRONMENT

with Halina Onishko, Austin Oleskie, Katie Jamenson, Darren Tyson, Vito Quaranta, and Erin Rericha

In chapter 2, we presented research that indicated drug response to targeted therapy is heterogeneous from cell to cell and sensitive to the surrounding environment. In chapter 3 and 4, we demonstrate how simplified two component mathematical models and available imaging measurements could be combined for early detection of drug resistance. In this chapter, we present experimental data that bridge the theoretical hypothesis and the eventual implementation. Assayed by time-lapsed fluorescent microscopy, we monitor the cell proliferation under targeted therapy. More specifically, we introduce our study of PC9 cell line in 2D and 3D culture. We quantify the drug sensitivity of 4 PC9 sublines in the relation to stiffness of the extracellular matrix, and find that the cell lines become more resistant to the EGFR inhibitor erlotinib as the cell culture environment becomes stiffer. Work in this chapter provides experimental evidence for sensitivity of tumor model parameters on environmental conditions and further establishes the need for patient-specific modeling related to clinical imaging.

6.1 Introduction

The PC9 cell line is representative of non-small cell lung cancer (NSCLC), and is derived from human lung adenocarcinoma. Like many examples of clinical NSCLC, the PC9 cell line is oncogene addicted through mutations of the kinase domain of the Epidermal Growth Factor Receptor (EGFR). Continued proliferation of PC9 cells generally requires activity of the EGFR

receptor. As such, the PC9 cell line is sensitive to inhibitors of the EGFR such as erlotinib and gefitinib[109, 110].

Previously, Quaranta's lab isolated 89 single-cell derived discrete sublines (DS) from the commonly studied PC9 cell line by monitoring the distribution of cell fates (division, quiescence, and cell death) and the drug-induced proliferation (DIP) rate under erlotinib treatment. Interestingly, they found that cells that derived from the same parental PC9 cell line display heterogeneous proliferation and sensitivity to erlotinib[78, 79], with some sublines continuing to proliferate in the presence of erlotinib. These results point to *de novo* resistance due to heterogeneity as an important component to the poor long term treatment response for patients undergoing erlotib thereapy[111] (See Figure 6.1 from unpublished work by Quaranta Lab).

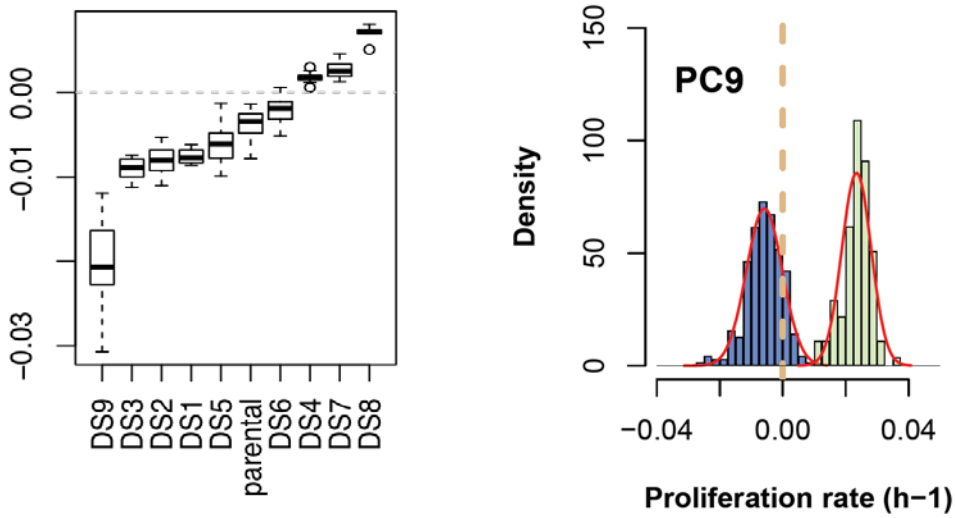

Figure 6.1 (1) The doubling rate of PC9 parental cell lines and 9 discrete sublines in 2D petri dish culture. (2) The distribution of PC9 discrete sublines' doubling rate. Lime colored lines are those without erlotinib treatment, and blue lines that under erlotinib treatment.

In this chapter, we present experimental data linking the DIP rate of PC9 sublines to the activity of known regulators of cell proliferation and cell fate e.g. EGFR, c-Met, integrins, and the carrying capacity. We focus on four of the 89 sublines: DS3, DS7, DS8 and DS9, that were found to span from most sensitive to most resistant to erlotinib treatment in 2D culture among the 89 sublines. We study how the change of environmental condition from 2D to 3D, as well as the stiffness of extracellular matrix, could influence the drug sensitivity. In addition, we find that c-Met expression positively correlates with DIP rate under therapy. Inspired by these results, we motivate a model for the heterogeneous DIP rate in PC9. While the model presented here is qualitative and in the spirit of many biological signaling models, we outline how to connect the model with quantitative predictions through progression of the cell cycle.

The experimental results and modeling presented in this chapter are preliminary and more experiments are required to provide solid evidence. However, my role in this work was to participate in experimental design, develop the data processing capability to analyze the data, perform the data analysis, and participate in the interpretation. In addition, these finding provide motivation for the modeling and analysis in the next two chapters. Here, we show that tumor cell growth and response to therapy is sensitive to the physical environment and is hence likely to vary from patient to patient.

6.2 Results

6.2.1 Tumor cell growth and drug response in 2D

We first confirmed the Quaranta lab result for the DS8 and DS9 sublines. Briefly, cells were plated at low initially density onto cell culture plastic and the total cell number was measured as a function

of time. In Figure 6.2 we plot the growth of the culture in terms of population doublings. The slope of the straight line fit is then the population DIP rate. As expected, under the control DMSO conditions, both the DS8 and DS9 cell populations have positive DIP rate ($0.047h^{-1}$ and $0.045h^{-1}$ respectively) and under erlotinib therapy both DIP rates ($0.019h^{-1}$ and $-0.017h^{-1}$ respectively) decreased (see Figure 6.2 (1)). The negative DIP rate for the DS9 population corresponds to a shrinking culture and would hence be considered clinically sensitive. DS8 in contrast, continued to proliferate in the presence of DS8, though at a decreased rate, and is hence termed resilient.

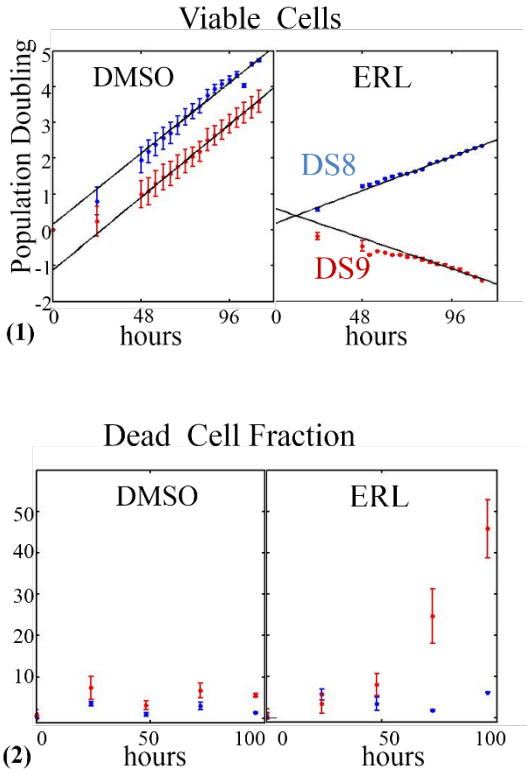

Figure 6.2 (1) Population doubling of DS8 and DS9 under 120 hrs observation for both without erlotinib treatment (DMSO) and with erlotinib treatment (ERL). (2) Percentage of DS8 and DS9 dead cells under 100 hours untreated condition and treated condition. Blue data points are corresponding to DS8, and Red to DS9.

To confirm the health of the culture, we use Trypan Blue which stains the nuclei of cells with compromised cell membranes. As expected, in the control conditions between 5%-10% of the cells are dead or dying. Under erlotinb therapy, the percent of DS9 cells that are dying increases with time. These results are consistent with the Quaranta lab finding, that DS8 is a resilient cell line under erlotinb therapy.

6.2.2 Tumor cell in 3D Collagen, Matrigel and Hydrogel

The cell culture environment, including composition and concentration of the extracellular matrix, frequently impacts the cell growth. To ascertain whether the PC9 sublines growth rate were sensitive to these environmental conditions, we observed cells embedded as single cells and at low density in three common extracellular matrices: type 1 collagen, 80% Matrigel, and HA Hydrogel. We find that both sublines grow in all three matrices, with mild differences in the cluster shape. Cells were found to grow to larger clusters in the 80% Matrigel.

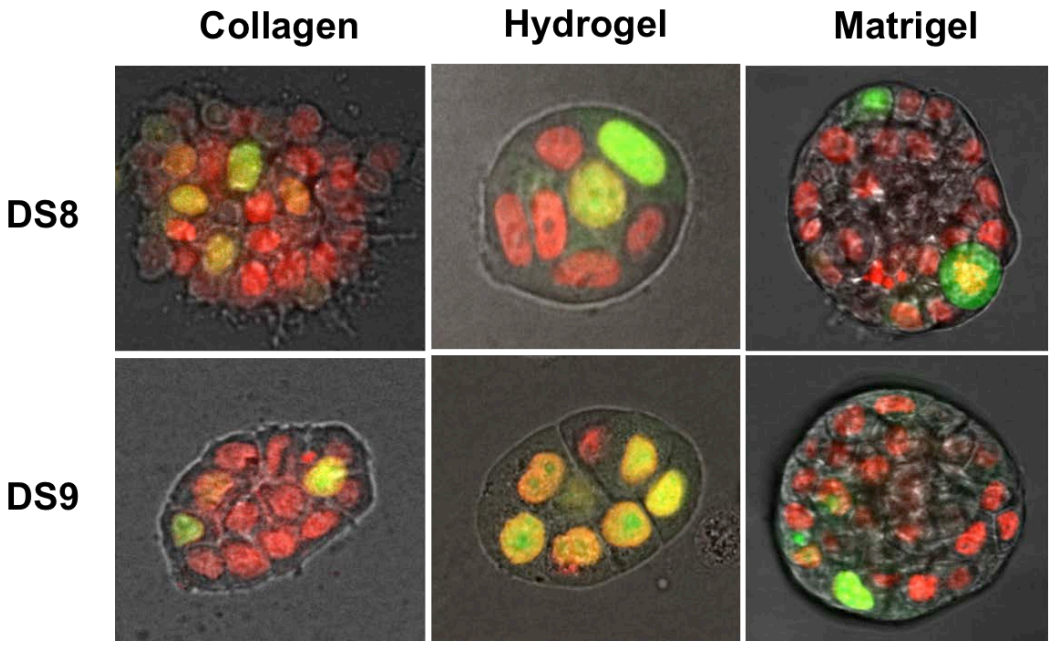

Figure 6.3 2D projection of typical DS8 and DS9 cluster in 3D Collagen, Hydrogel and Matrigel extracellular matrices after 6 Days culturing.

In order to compare the erlotinib treatment response of cells suspended in ECM to cells grown in 2D on cell culture plastic, we first tracked the fraction of dead cells within the suspended culture. Similar to the 2D conditions, the control (DMSO) treated suspended cultures showed minimal accumulation of dead cells over time. The DS9 subline showed clear sensitivity to erlotinb therapy (cell death reaching 50% or more 4 days after treatment) in all three ECM's examined. Surprisingly, the DS8 subline also acquired a substantial fraction of dead cells overtime in all three ECM's, indicating that the DS8 resilience is modulated by cell culture condition. As the 80% Matrigel environment showed the least accumulation of cell death, we focused on this ECM for the remainder of the study.

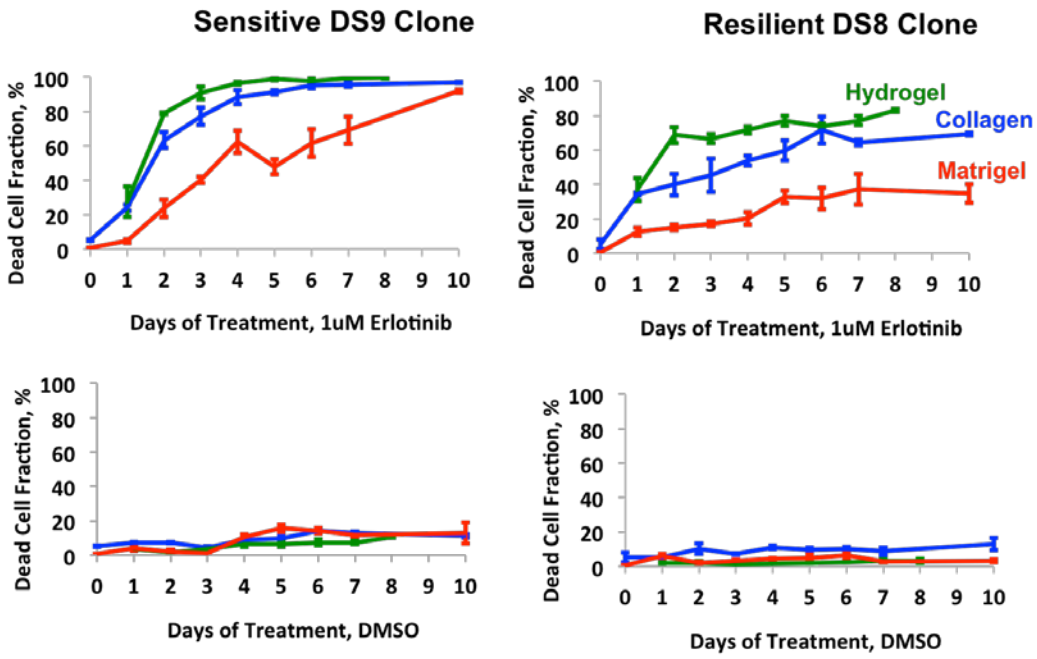

Figure 6.4 Dead cell fractions of DS8 and DS9 under 10 days' control and erlotinib treatment in Collagen (blue), Hydrogel (green) and Matrigel (red) ECM respectively.

6.2.3 Tumor cell growth and drug response in 3D through single cluster tracking

Instead of sacrificing the matrix each day for cell counting (as that used in Figure 6.4), we later improved the setup that allows the monitoring of the same 3D spheroid regions over time. We select 40 random cell clusters from four sublines DS3, DS7, DS8 and DS9, and track their growth through 3D confocal imaging on a daily basis. We also developed an algorithm to segment, count, and determine cell fate from confocal stacks of the PC9 clusters (see methods session at 6.4). Using the segmentation routine, we identify and count the viable cells within each cluster and compute the DIP rate based on 6 days of growth in the presence and absence of therapy for each cluster. Figure 6.5 displays the histograms of the data. We find that the spread in the DIP rate is substantial within each data set. Even in controlled conditions, more than 10% of the clusters of DS3, DS7,

and DS9 do not grow beyond 2 cells. Under the control conditions, the distributions are reasonably close: both p values from the T-test and Kolmogorov–Smirnov test (K-S test) dedicated to differentiate the DIP rate distribution of these four cell lines indicate that only DS7 and DS8 are significant different to each other. However, under erlotinib therapy, the p-values show that the DS9's DIP rate is significantly more negative, and the rest three shows similar DIP distribution with a mean value of approximately -0.01 hr^{-1}. Note that in 2D treated experiment (see, Figure 6.1), the expected DIP rate for both DS7 and DS8 are positive, but in 3D culture they both exhibit reduced growth close to DS3 with overall negative proliferation. The solid green line indicates the measured DIP rate from the 2D culture conditions. In control, the cluster growth is slightly decreased compared with 2D, however, the 3D growth is substantially reduced for all conditions compared to 2D.

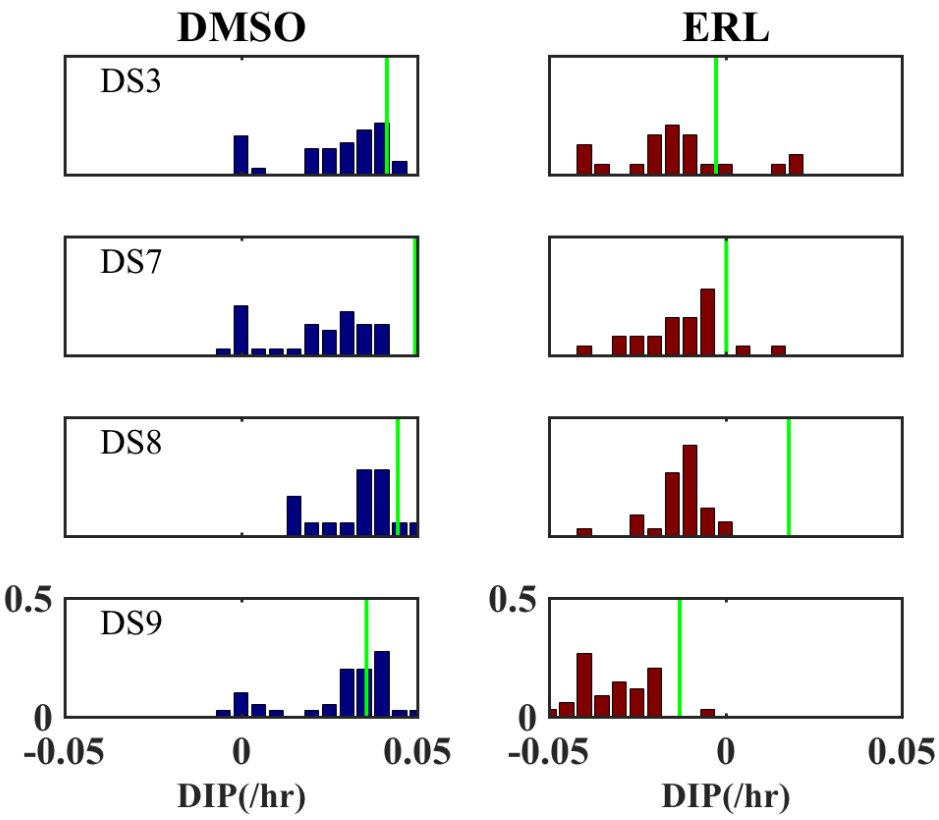

Figure 6.5 Comparison of tumor cell growth and drug response in 2D and 3D. Blue (DMSO) and red (ERL) histograms are based on the DIP rate of 40 clusters each, and are normalized to an area of 1. Green lines are the averaged DIP rate of tumor clusters in 2D.

p-value t-test	DS3	DS7	DS8	DS9
DS3	1	0.179	0.100	0.551
DS7	0.179	1	0.007	0.054
DS8	0.100	0.007	1	0.261
DS9	0.551	0.054	0.261	1

p-value ks-test	DS3	DS7	DS8	DS9
DS3	1	0.423	0.228	0.674
DS7	0.423	1	0.016	0.065
DS8	0.228	0.016	1	0.653
DS9	0.674	0.065	0.653	1

Table 6.1 p-values from t-test and ks-test under controlled condition (DMSO). P values less than 0.05 are highlighted in red.

p-value t-test	DS3	DS7	DS8	DS9
DS3	1	0.618	0.458	0.002
DS7	0.618	1	0.860	0.000
DS8	0.458	0.860	1	0.000
DS9	0.002	0.000	0.000	1

p-value ks-test	DS3	DS7	DS8	DS9
DS3	1	0.742	0.144	0.000
DS7	0.742	1	0.481	0.000
DS8	0.144	0.481	1	0.000
DS9	0.000	0.000	0.000	1

Table 6.2 p-values from t-test and ks-test under erlotinib treated condition. P values less than 0.05 are highlighted in red.

6.2.4 Tumor cell in hanging drop

Moving from 2D plate culture to 3D suspended culture in ECM modulates numerous factors including the chemistry of the environment, the amount of contact among cells, and the stiffness of the growth environment. We next sought to isolate these variables. Cells cultured in 3D hanging drop spheroids are devoid of ECM chemical stimulations, yet remain suspended and have increased cell-to-cell contact compared to 2D. We found that the fraction of dead cells substantially increased in the hanging drop culture compared to both 2D and 3D 80% Matrigel conditions. The

hanging drop experiment strongly suggests that the chemical composition of the ECM is not solely responsible to the shift in sensitivity.

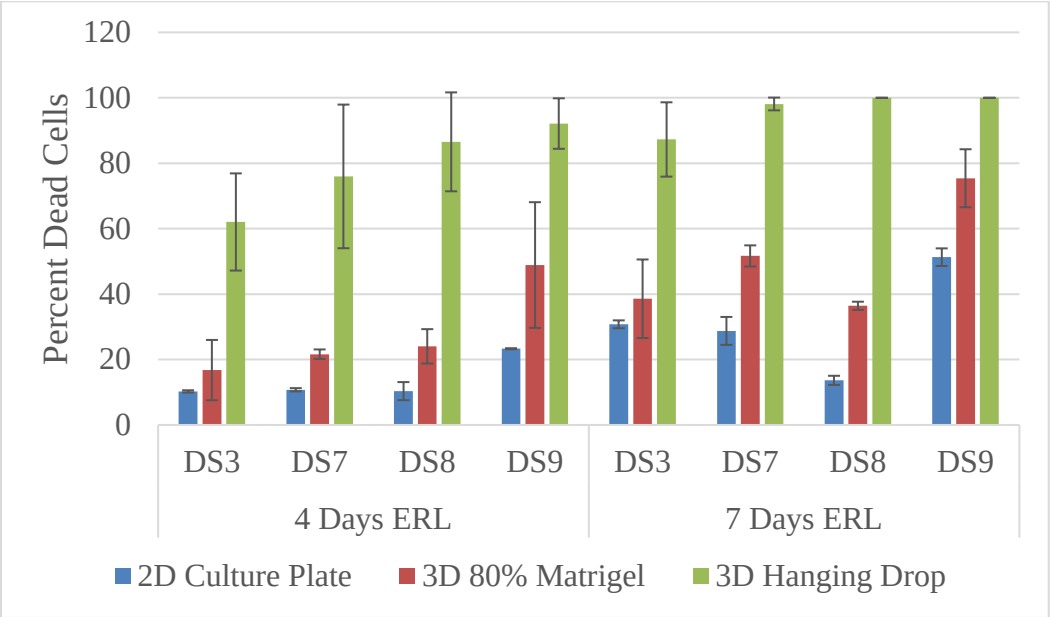

Figure 6.6 Dead cell percentage in 2D culture plate, 3D 80% Matrigel and 3D hanging drop for DS3, DS7, DS8 and DS9 after 4 Days and 7 Days of erlotinib treatment respectively.

6.2.5 Change in 2D substrate stiffness recapitulates the increased sensitivity in 2D

2D cell culture plastic provides a stiff substrate for cell growth (approximately 2-4GPa). It is well known that cells are mechanosensitive and that substrate stiffness influences a wide range of cellular behaviors including the actin cytoskeleton, the expression and activity of integrin, and the differentiation of the cells[112]. The hanging drop cell culture environment is substantially less stiff than the 80% Matrigel ECM which is less stiff than the 2D culture plastic, suggesting that erlotinb response might be strongly modulated by stiffness.

Human tissues vary substantially in stiffness. For example, brain and lung tissue are less than 0.8kPa, skeletal muscle is around 12kPa, and bones are similar to that of plastic and glass(4MPa) [112]. We set up an experiment using polyacrylamide (PA) gels which allow for controllable stiffness of the surface for cultured cells when varied concentration. Inspired by Cretu [113], we cross linked PA gels with type 1 collagen to create 2D cell culture conditions with variable stiffness (0.68kp, 59kpa, 86kpa). In Figure 6.7, we summarize 11 sets of independent experiments used to obtain the DIP rate of DS8 and DS9 under erlotinb therapy in stiffness of 0.68kPa, 59kPa, 86kPa and that of Glass(4MPa). The DIP rates under erlotinib inversely correlate to substrate stiffness for both DS8 and DS9. From our preliminary experiments, the obtained DIP shows a linear correlation with the logarithm of surface stiffness.

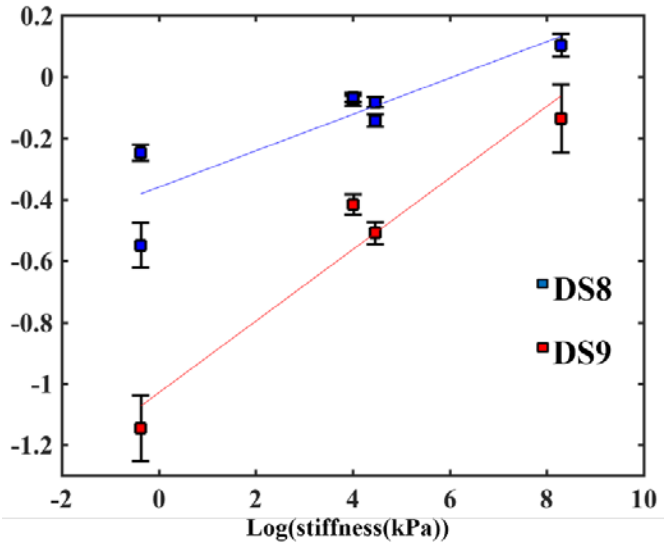

Figure 6.7 DIP rate under erlotinib treatment vs the logarithm of stiffness produced in PA gel and glass. Results from DS8 and DS9 are labeled with blue and red respectively.

6.2.6 Difference in morphology prior to treatment correlate with treatment?

Through the tracking of DS3, DS7, DS8, and DS9 3D clusters, we find that cluster shape varies between sub cell lines and within sub cell lines. We consider whether the characteristics of morphology can be an indicator to treatment sensitivity. To quantify our observation, we use radial distribution function (RDF) to identify the most likely cell-cell distance within each cell cluster. Our analysis covers 40 clusters in each cell line in controlled conditions. Note that we only apply RDF analysis only to clusters that have more than 8 cells (usually after Day 4), so that first peaks in RDF is more distinct, thus, the interpretation more relevant. Figure 6.8 shows the captured most likely cell to cell distance in each cell line versus the number of cells in each cluster. We then perform linear fitting of the two variables as shown in the black solid line in the figure. The coefficient of determination (R-squared value) for all four linear fitting is less than 0.06, indicating no significant correlation between the cluster size and cell-cell distance. We find that DS3 and DS7 have relatively shorter cell-cell distance (around 11μm), while DS8 and DS9 have most likely cell-cell distance of 14μm. This indicates that the maximum carrying capacity—a key parameter in Chapter 4 and 5—should be a variable specific to each cell line.

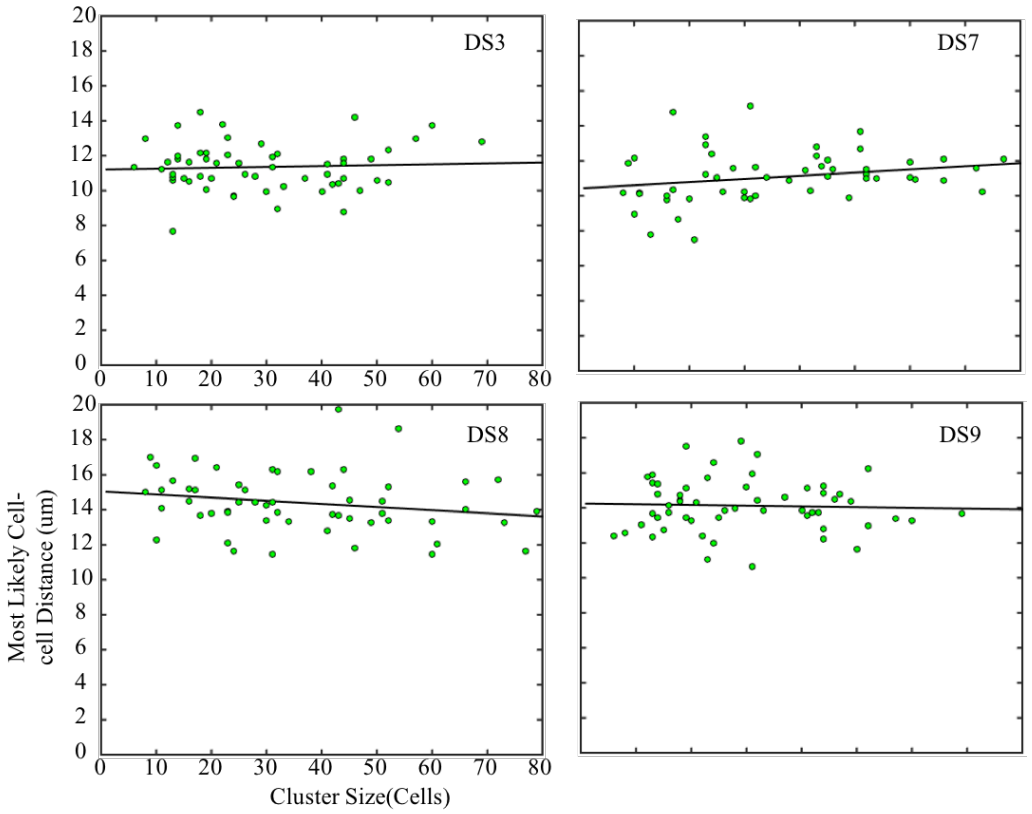

Figure 6.8 Plot of the most likely cell-cell distance Vs the size (number of cells) of cluster. Black lines are the linear fitting of the green dots in each plot.

6.2.7 Connection to *in vivo*

In the last two decades, multiple cellular functions have been found to be sensitive to the substrate stiffness in monolayer culture conditions. Simultaneously, more methods have been developed for measurements of human tissue including indentation by AFM, tension, and elastography[114]. The elastic modulus of lung tissue typically falls within 400 -600 Pa and increases in stiffness with age. At this stiffness, we would predict that DS8 cells had a slight negative DIP rate under erlotinb therapy with DS9 being primarily negative.

In a complementary research effort, the Quaranta lab investigated whether the difference in DIP rate between DS8 and DS9 sublines observed in 2D culture, on cell culture plastic, persisted *in vivo*. They used the common subcutaneuous tumor model, where DS8 or DS9 cells are resuspended in Matrigel and injected between the muscle and the skin of the mouse's back. The growth of the subsequent tumor was monitored by capillary measurement as well as by ultrasound. Total tumor cell number was inferred from these measures of cell volume and the results shown in Figure 6.9. Under control (DMSO) both cell lines grew at approximately 1/6th the rate as the *in vitro* experiment.

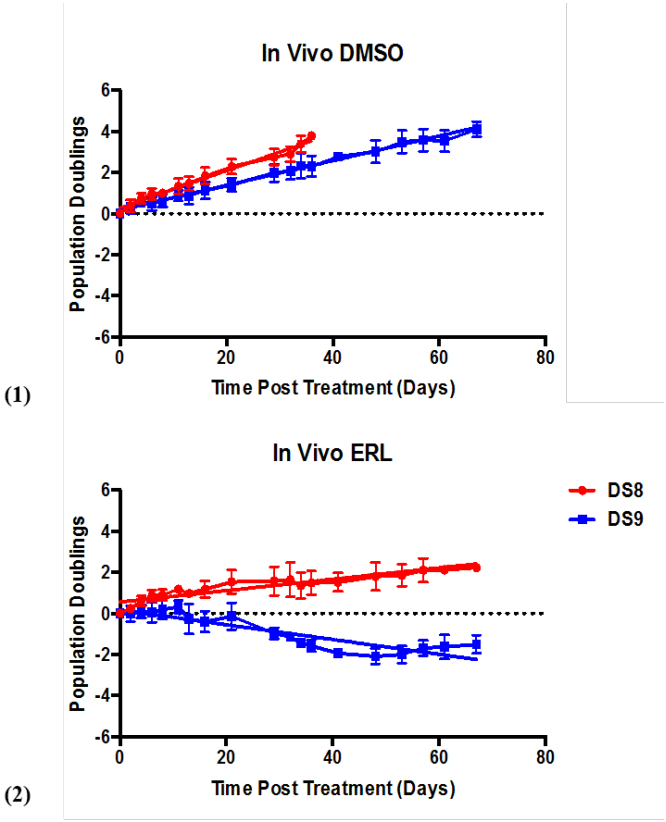

Figure 6.9 (1) Population doubling of DS8 and DS9 tumor cells in subcutaneous mouse model without erlotinib treatment. (2) Population doubling of DS8 and DS9 tumor cells in subcutaneous mouse model under erlotinib treatment.

Four mice where tumors were allowed to initially grow, were treated with daily injections of erlotinib and the tumor size post treatment similarly monitored. Similar to the 2D stiff substrates condition, tumors composed entirely of DS9 decreased in volume whereas tumors composed entirely of DS8 on average increased. While it is difficult to infer the substrate of a subcutaneous tumor, measurements of the Young's modulus of skeletal muscle report measurements from 12-45 kPa[115]. At this stiffness, the polyacrylamide experiments above suggest that the DS8 DIP rate would be slightly positive, consistent with the *in vivo* measurements.

6.2.8 Variations in protein concentration prior to treatment correlate with treatment outcome

Interestingly, in all of the above perturbations, the DIP ordering of the cell lines was consistent. DS8 subline maintained a higher DIP rate than the DS9 subline, with the DS3 and DS7 remaining in between. Working with our collaborators, we next considered whether the ordering of DIP rates could be predicted by cell factors prior to treatment. The heterogeneous response to erlotinb therapy across the PC9 cell line could be understood in the context of regulators of the cell cycle and hence a platform for quantitatively testing cell cycle / cell fate models.

Evidence collected from Darren Tyson and Katie Jameson (see Figure 6.10) suggested that c-Met expression prior to drug treatment correlated with DIP rate under erlotinb therapy, with DS8 having considerably higher c-Met expression than DS9. This result is consistent with previous findings in the literature suggesting that c-Met provides can confer resistance to erlotinb therapy[116].

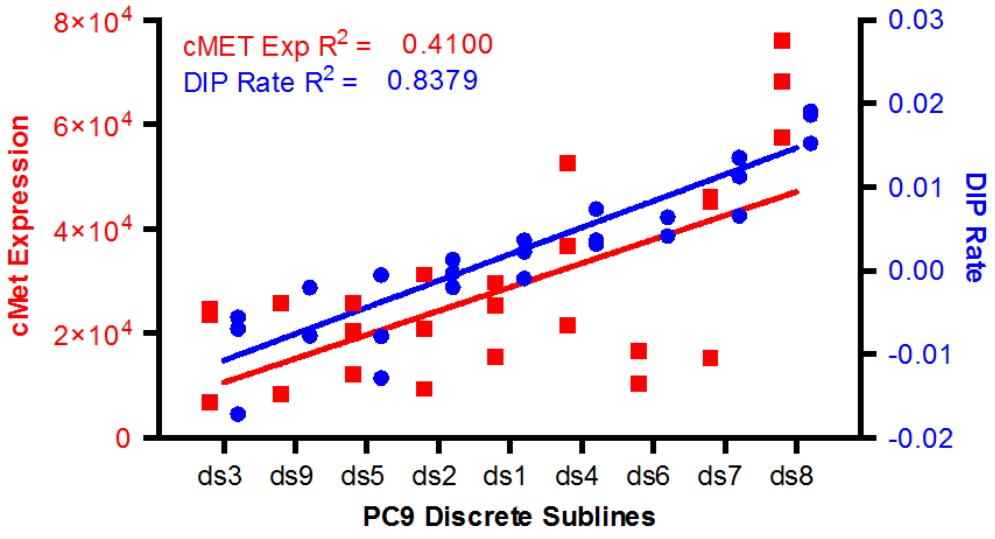

Figure 6.10 Synchronized y axes plot of c-Met expression (red) and DIP rate (blue) under erlotinib treatment from DS1 to DS9 sub cell lines.

This data predicted that drug inhibition of c-Met in the presence of erlotinb should cause a reduction in DIP rate in all sublines. Darren Tyson and Katherine Jameson applied foretinib, a c-Met inhibitor, in the presence of erlotinb. Under these condition DIP rates in general decreased, with the DS8's asymptotic growth becoming negative (see Figure 6.11).

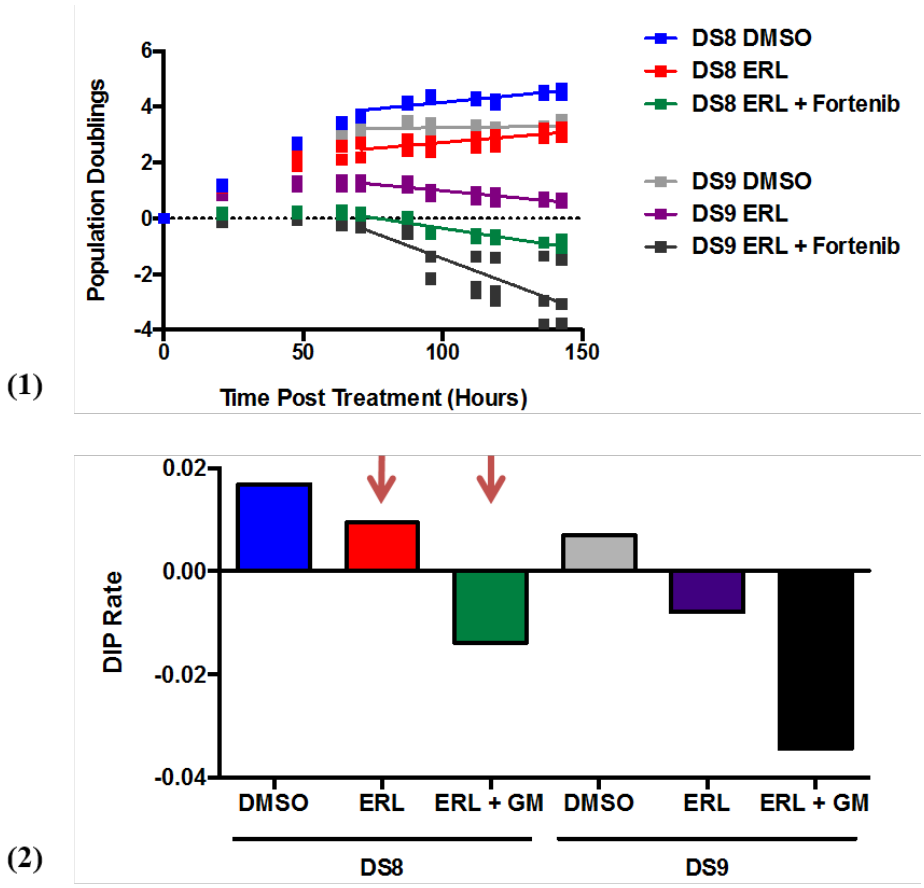

Figure 6.11 (1) Plot of population doubling for DS8 and DS9 under DMSO condition, erlotinib treatment, and Foretinib added erlotinib treatment. (2) Plot of corresponding DIP rate in (1). Red arrows highlight the shift in DS8 from positive to negative DIP rate once the c-Met inhibitor foretinib is added.

We next sought to confirm the c-Met DS8 link via Western blotting and asked whether increased c-MET activity continued to distinguish DS8 and DS9 in two culture conditions on 2D glass (stiff) and 3D Matrigel (soft) (see Figure 6.12). We find that the expression of pMet/Met and Met/tubulin is consistently higher in DS8 and in DS9 under both cell culture conditions, however, higher c-Met activity was not sufficient to predict DIP rate, as the ratio of pMet/Met substantially increased for DS8 in Matrigel, but the DIP rate under drug treatment decreased. In contrast, the

expression of pAkt(Thr308)/Akt and FAK/Tubulin correlate with both the resistance level of each cell line and the stiffness of the external environment, suggesting a link to DIP rate. This analysis predicted that drug inhibition of c-Met in the presence of erlotinb should cause a reduction in DIP rate in all sublines, and potentially most strongly impact DS8.

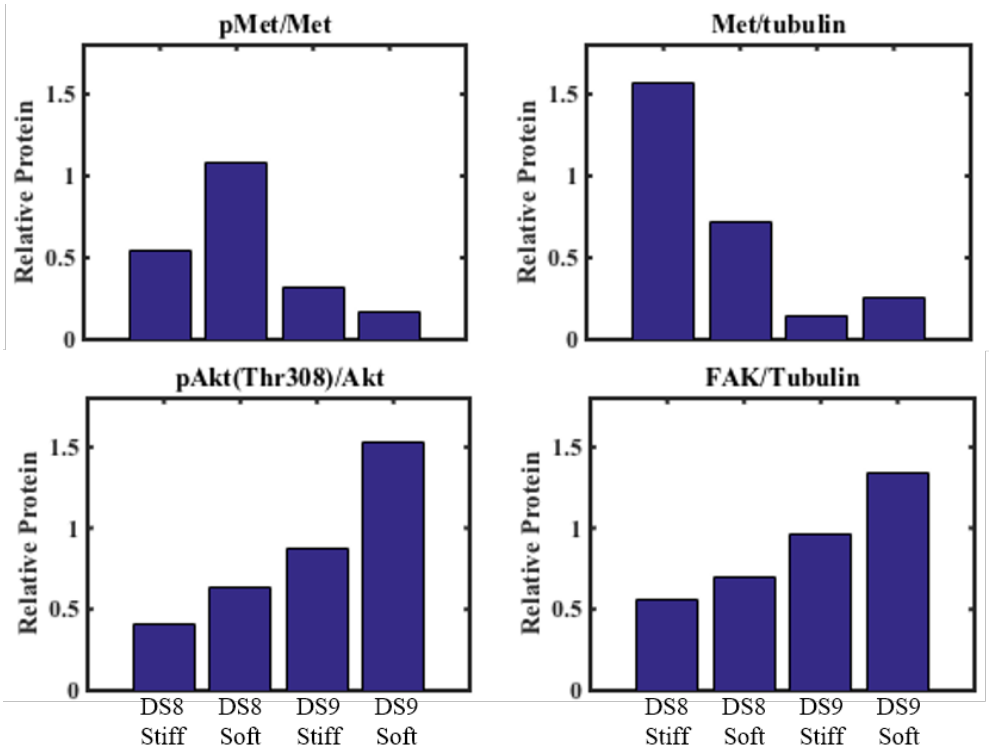

Figure 6.12 Quantified results of electrophoresis from western blotting experiments under four experimental conditions– DS8 stiff, DS8 soft, DS9 stiff and DS9 soft. The four quantification metrics used are pMet/Met, Met/tubulin, pAkt(Thr308)/Akt and FAK/Tubulin.

6.3 Experimental Setup

6.3.1 Cell culture and cell lines

PC9 discrete sublines were obtained from Vito Quaranta lab (Vanderbilt University School of Medicine). They were derived as single cell clones from parental PC9 cell line, expanded in drug-free media, and fluorescently labeled with FUCCI marker (same as that used in Chapter 5 experiments) using lentivirus-mediated transduction as previously described[78]. Cells were cultured in CO_2 (5%), temperature (at 37°C) and humidity controlled incubators. On a daily basis, the cells were incubated with dead cell marker SYTOX blue (Life Technologies) for 10 minutes, washed with PBS and supplied with fresh media. Before use, the cells were confirmed to be negative for mycoplasma using MycoAlert PLUS kit (Lonza). Cells were cultured in RPMI 1640 media supplemented with 10% FBS (Atlanta Biologicals) and Antibiotic/Antimycotic mix (Gibco). During imaging, the media was substituted for OPTI-MEM media (Gibco), supplemented with 2% FBS, and Antibiotic/Antimycotic mix to reduce background auto-fluorescence. The growth rate was confirmed to be the same for these sublines in both types of media.

6.3.2 2D plastic and glass

In 2D experiments, cells were plated on either plastic Falcon 96-well imaging plates (Corning, 353219) or collagen-coated 25mm glass coverslips (Fisher) immobilized on 6-well culture plates. After an overnight incubation, cells were treated with either DMSO for 1 week or 1-3μM erlotinib for 2-3 weeks. Media was changed every 3 days.

6.3.3 Cells in 3D ECM

We primarily use 80% Matrigel (Corning) as the base material to form 3D ECM. 5x104 cells/ml were embedded in either 4 or 8-well 1.5 glass bottom Lab Teck II chambers (Fisher). The ECM was reconstituted and polymerized according to the manufacturer's instructions. OPTI-MEM media supplemented with 2% FBS and Antibiotic/Antimycotic mix (Gibco) was added on top after matrix polymerization, and generally it takes 3 days for cells to form 6-10 cell clusters. Distinct from 2D experiment, cells in 3D EGM can form organized yet diverse structures. Figure 6.13 shows the cell cluster formation and spatial distribution in 3D EGM after 5 days of incubation. Cell locations are extracted from 49 (7 x 7) stitched confocal imaging Z-stacks using methods described in the cell segmentation section of the Chapter. Each stack is of dimension 258μm x 258μm x 250μm. 0 in the z axis corresponds to the bottom of the well, where flat distribution of cells can be observed. As shown in Figure 6.13, cell clusters vary largely in shape and size.

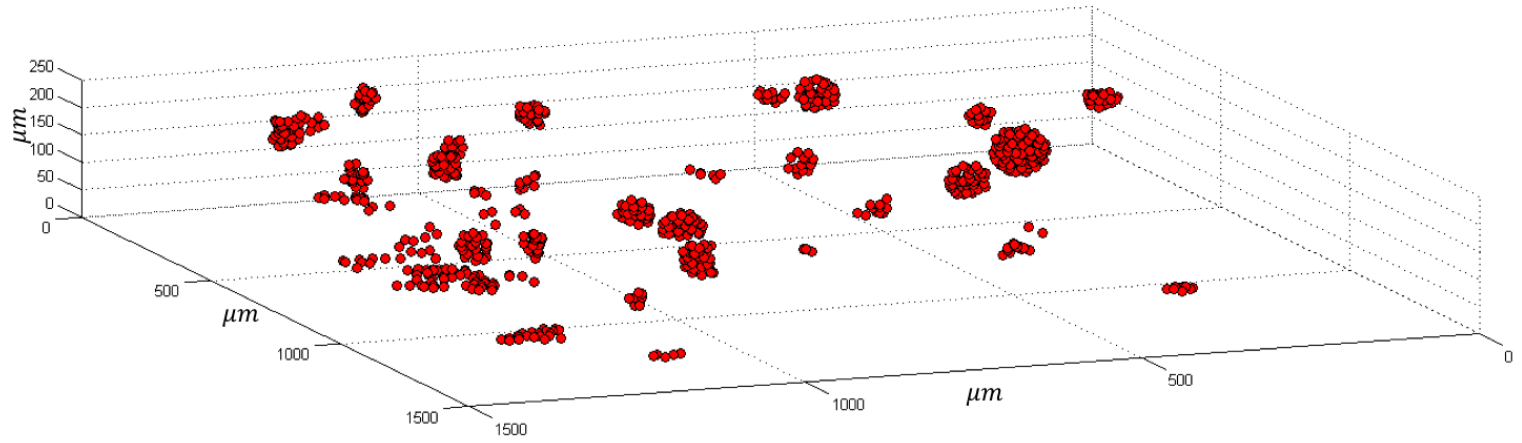

Figure 6.13 Cell cluster formation and spatial distribution in 3D EGM after 5 days of incubation. Cell location are extracted from stitched 3D confocal image.

In control conditions without treatment, cells in 3D ECM are allowed to grow for 7-10 days with daily media change. A typical 3D tumor cluster captured by confocal imaging is shown in Figure 6.14 from day 1 to day 8 of incubation. This cluster is close to spheroid, and going through active growth indicated by the green fluorescent cells in the cluster.

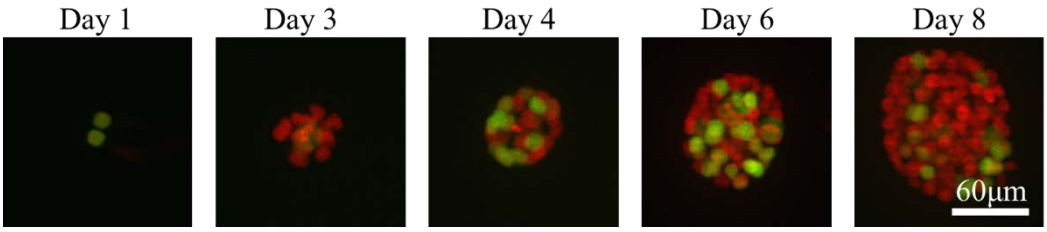

Figure 6.14 Projection of 3D cell cluster growth without drug treatment in 80% Matrigel captured by confocal imaging. Red (in S/M/G2 phase) and green fluorescence (in G1 phase) indicates cell nuclei location.

As for the design of treated experiment (see Figure 6.15 (1)), cells are first allowed to grow without treatment for 3 days to form 6-10 cell cluster. Imaging (if applicable) begins at last day of untreated condition, and then 1μM erlotinib is added to the media daily for 3 weeks along with media change. Figure 6.15 (2) and (3) show the typical tumor cell clusters' response for resilient (DS8) and sensitive (DS9) cell lines respectively from day 2 to day 14. The resilient DS8 cell line remains in active proliferation state through the course of treatment, as marked by the green fluorescent cells. The sensitive DS9 cell line starts to show cell disintegration as early as day 4 of the treatment, as indicated by the SYTOX blue fluorescent cells. By day 14, while there are still lingering cells in the DS8 cluster, all the cells in the DS9 cluster has dead and disintegrated.

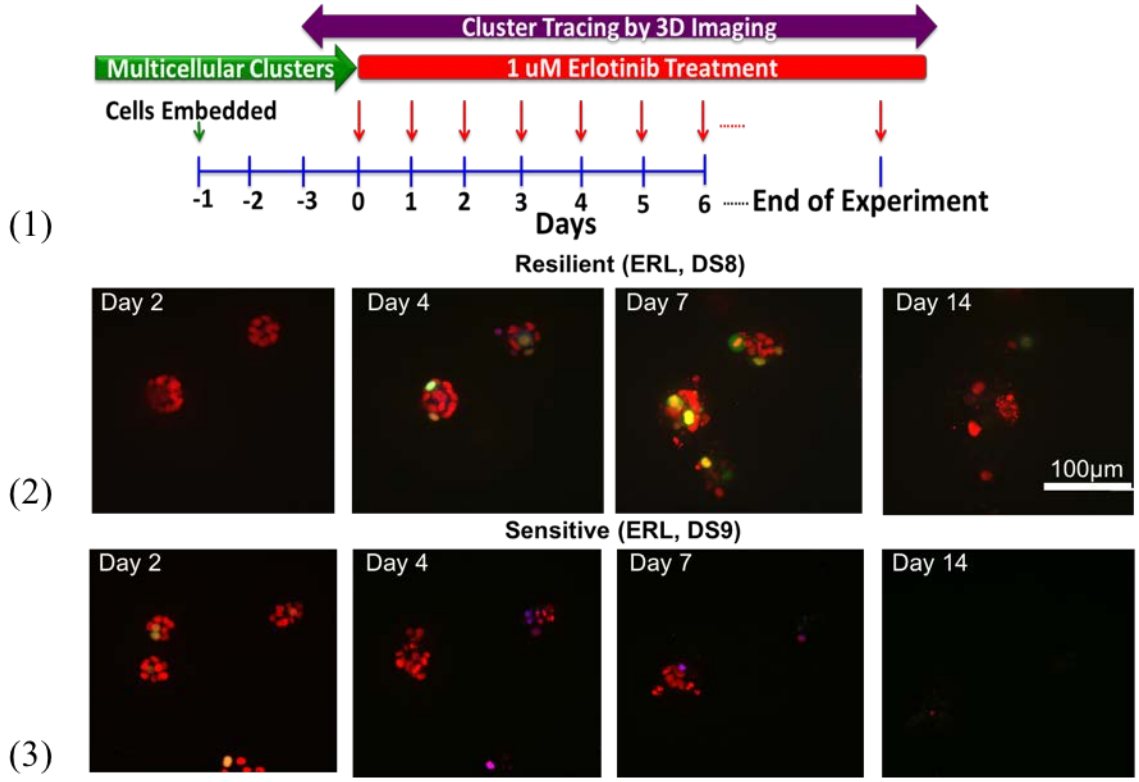

Figure 6.15 (1) Experimental design of tumor cluster response to erlotinib. Experimental design of tumor cluster response to erlotinib. Cells are embedded three days before treatment, and imaging starts one day before. (2) and (3) are typical tumor cell cluster response drug treatment by resilient and sensitive cell lines respectively. Image are generated from z-projection of z stack images.

Two methods of cell counting are used:

(1) For fast quantification that doesn't require spatial information, the matrix was disrupted with an appropriate agent on a daily basis. For example, Dispase (BD Biosciences) were used as the reagent to disrupt 3D Matrigel. Cells were dissociated, washed with PBS, and stained with 0.4% trypan blue dye (Fisher). Using hemocytometer, the viable (clear) and dead (blue) cell numbers were counted, and the dead cell fraction over time was determined.

(2) For quantification that includes cell spatial information, we use Zeiss confocal microscopy to acquire 3D stacks of the same cell clusters with 20X objective, and the total (H2B-RFP), proliferating (mAg-GFP) and dead (SYTOX blue-CFP) cells were counted using segmentation methods described in later chapter.

6.3.4 Cells in 3D hanging drop spheroids

3D hanging drop experimental design (see Figure 6.16 for the schematic drawing of experimental setup) allows cells to form 3D structure assisted by water pressure, yet is devoid of ECM's chemical influence. 3D hanging drop spheroids are set up in Perfecta3D 96-well hanging drop plates according to the manufacturer's specifications (3D Biomatrix). $5x10^3$ cells/drop were suspended in 40µl of either RPMI (with 10% FBS and Antibiotic/Antimycotic) or OPTI-MEM (with 2% FBS and Antibiotic/Antimycotic) media with no ECM added. Similar to 3D ECM experiment, spheroids were allowed to form overnight, and the treatment started the next day with either DMSO or 1µM erlotinib for 7 days with daily media refreshment. Spheroids are harvested on day 4 and 7, dissociated with 0.25% trypsin, washed with PBS, and stained with 0.4% trypan blue. Using hemocytometer viable (clear) and dead (blue) cells were counted, and dead cell fraction within each sample was determined.

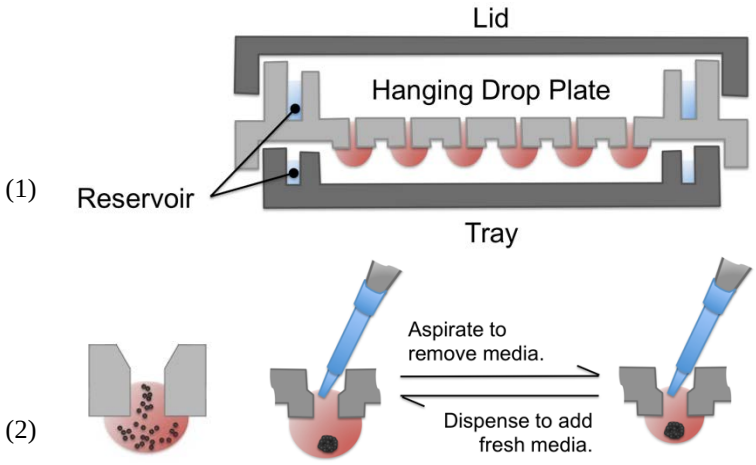

Figure 6.16 Schematic plot of the design of hanging drop experiment. (1) The overall layout of the hanging drop plate. Red ball shapes are the hanging water drops that culture the cell growth. The lid and reservoir keep the hanging drop protected from water evaporation. (2) Cell culturing within a single hanging drop. Initially the cells are suspended in the media, seeded into a single droplet, and later on cultured through media change.

6.3.5 2D polyacrylamide (PA) gels

The 2D PA gels experiment is conducted to test the impact of surface stiffness to erlotinib sensitivity, as the PA gels allows for controllable surface stiffness for cultured cells when varied concentration. The PA gels were set up as described in the reference [113]. Briefly, polyacrylamide gels of different stiffness (86kPa-0.68kPa) were cross-linked to 3-APTMS coated coverslips. Incorporation of N- hydroxysuccinimide ester into the PA solution allowed for cross-linking of ECM (collagen type I) to the gel. Coverslips with gels were immobilized on the bottom of the 6-well plates, and cells were plated at the starting density of $1x10^5$ cells/well in OPTI-MEM media supplemented with 2% FBS and Antibiotic/Antimycotic mix (Gibco). After an overnight incubation, the fixed positions (4x4 mosaic images) of cells were imaged daily on Zeiss confocal microscope (20X magnification) and then stitched and quantified using ImageJ software. Imaging

and treatment last for 7-10 days for DMSO and for 3 weeks for erlotinib treated cells with daily media change.

6.3.6 Western blotting

We conduct western blotting experiments to identify protein expressions that are closely related to cell-cycle signaling pathway. Cells were rinsed with PBS and scraped off the gels in M-PER lysis buffer (Pierce) supplemented with protease and phosphatase inhibitor cocktails (Sigma). Cell lysates of equal protein amount were separated on 10% NuPAGE Novex Bis-Tris SDS-PAGE gels (Life Technologies) and transferred to 0.2μm Pure Nitrocellulose Membrane (BioRad). Immunoblotting was performed with the following antibodies: Met (Cell Signaling, 8198), phospho-Met (Tyr1234/1235, Cell Signaling, 3126), Akt (Cell Signaling, 9272), phospho-Akt (Ser473, Cell Signaling, 4058), phospho-Akt (Thr308, Cell Signaling, 2965), FAK (Cell Signaling, 3285), integrin beta 1 (Abcam, ab30394), and beta tubulin (Sigma, T0198). For visualization of signal, the blots were incubated for 1 minute with SuperSignal West Pico Chemiluminescent Substrate (Thermo Scientific), and images were acquired with ChemiDoc Touch Imaging System (BioRad), see Figure 6.17 and quantified with ImageJ.

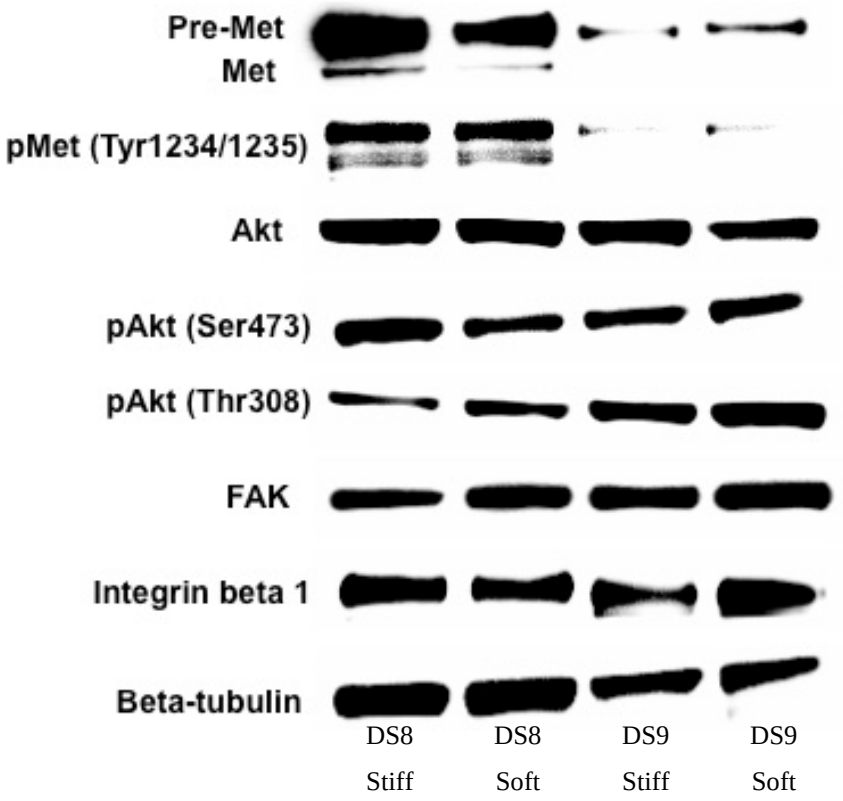

Figure 6.17 Electrophoresis result from western blotting experiments used to test pathways that are related to proliferation. Four sets of experimental conditions– DS8 stiff, DS8 soft, DS9 stiff and DS9 soft– are set to determine the influence of sub cell lines and ECM stiffness.

6.3.7 Image acquisition

For 3D experiments, images are taken on Axio Observer Z1 spinning disk confocal microscope (Zeiss, serial # 3834004261). During imaging, the cells are maintained in incubation conditions of 5% CO_2, 37°C temperature and humidity. Z-stacks of 2μm per slice were acquired with 20X objective at the following laser settings – 561λ at 12% laser power and 100ms exposure, 488λ at 1% laser power and 125ms exposure, and 458λ at 100% laser power and 400ms exposure. The volume of 258μm x 258μm x 250μm was imaged such that each spheroid was centered in the middle. The position of each cell cluster was marked and imaged daily for the duration of the

treatment. For 2D and PA gel experiments, the magnification and laser settings are the same as that in 3D experiment.

6.4 Quantification methods

6.4.1 DIP rate and dead cell fraction

We use drug induced proliferation (DIP) rate as our major quantification of drug response for our cell culture work. DIP rate is the doubling rate of cell proliferation as described in Equation

$$N(t) = N_0 2^{k_{DIP}t} \tag{6.1}$$

where $N(t)$ is the cell number at time t, and N_0 is the seeding cell number at time t=0, k_{DIP} is the DIP rate of cell proliferation. k_{DIP} can be calculated as

$$k_{DIP} = \log_2(N(\Delta t)) - \log_2(N_0)/\Delta t \tag{6.2}$$

See Figure 6.18 as example of how DIP rate calculated for DMSO and drug response respectively. Notice only the exponential phase is considered for the calculation of DIP rate.

Under the drug treated condition, alternative to the DIP rate calculation, simple quantification of dead cells fraction can be used to determine the drug efficacy. We use the dead cells fraction to compare the cell drug sensitivity under three experimental conditions—2D glass, 3D 80% Matrigel and hanging drop experiment.

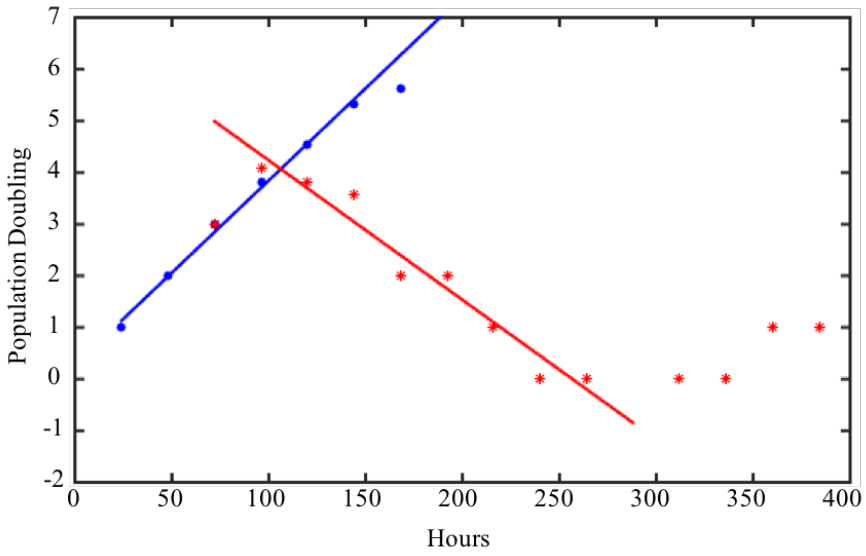

Figure 6.18 Example of DIP quantification. Blue and red dots represent log2 (population doubling) of cell number change along time for DMSO growth environment and erlotinib treated. DIP rate are based on linear part of log2(N) change only. DIP rate is the slope of the fitted line shown.

6.4.2 Radial distribution function

Within a system of particles, such as molecules in liquid, Radial Distribution Function (RDF) is often used to describe how particles are radially packed around each other. We define the average density of other particles in distance r to a given particle is defined as $\rho(r)$. We then normalize $\rho(r)$ by the average density of the system, ρ, and obtain the dimensionless RDF $g(r)$, defined as

$$g(r) = \rho(r) / \rho \qquad (6.3)$$

Notice that for an infinite system, because other particles cannot occupy the same space, as the given particle as r approaches to 0, $g(r)$ is approximated to 0; because $\rho(\infty)$ is approximated to system ρ, as r approached to ∞, $g(r)$ is approximated to 1. See Figure 6.19 (1) as example of the

radial distribution function for the monatomic Lennard-Jones liquid[117]. The first peak represents the most likely atom-to-atom distance.

For a homogeneous isotropic system, RDF only depends on the relative distance between particles. That is, we can further derive

$$\int_{r=0}^{\infty} \rho(r) 4\pi r^2 dr = N - 1 \tag{6.4}$$

$$\int_{r=0}^{\infty} g(r) \rho 4\pi r^2 dr = N - 1 \tag{6.5}$$

Consider the average number of particles inside the shells from distance *r* from every given particle:

$$\int_{r}^{r+\Delta r} \rho g(r) 4\pi r^2 dr = (N-1) \int_{r}^{r+\Delta r} \sum_{i=1}^{N} \sum_{k \neq i}^{N} p(r \leq | \vec{r}_k - \vec{r}_i | < r + \Delta r) dr \tag{6.6}$$

Thus in practice, we can calculate *g(r)* as

$$g(r) = \frac{N-1}{4\pi r^2 \rho} \sum_{i=1}^{N} \sum_{k \neq i}^{N} p(| \vec{r}_k - \vec{r}_i | = r) \tag{6.7}$$

In Figure 6.19 (2), we show the RDF of the 3D cell cluster. We use the location of the first peak as the estimated most likely cell to cell distance.

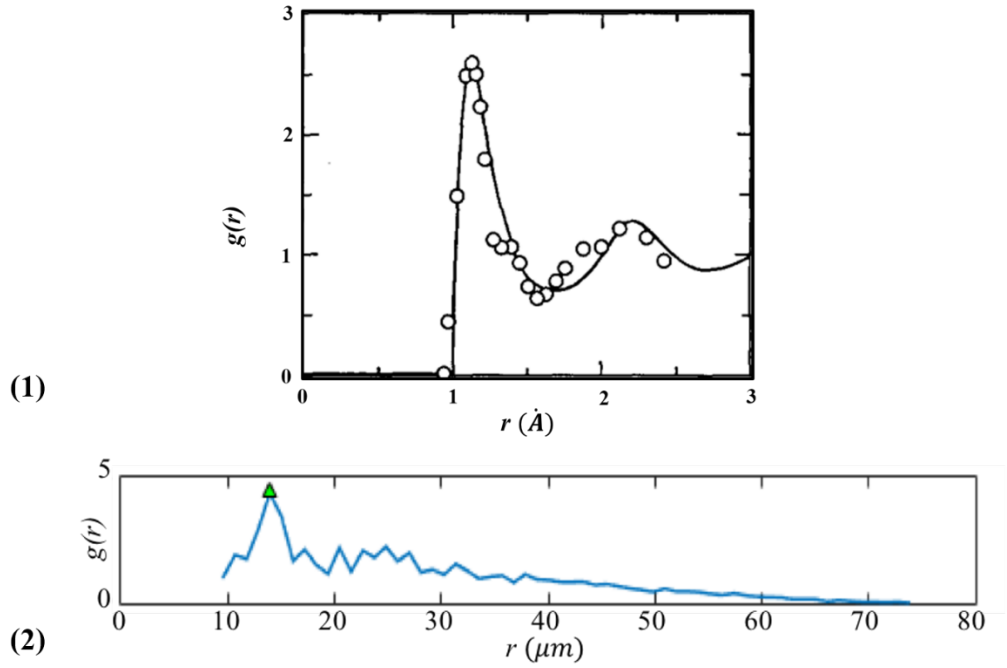

Figure 6.19 Examples of radial distribution function. (1) Typical radial distribution function for the monatomic Lennard-Jones liquid. Å stands for Angstrom. Solid line is from theoretical simulation, and dots are from experiments[117]. (2) Radial distribution function of a typical DS7 cell cluster with 69 cells. The peak, at approximately 14μm, marks the most likely cell-cell distance within this cluster.

6.5 Summary of the chapter

In this chapter, we presented the study of lung cancer growth and response to erlotinib therapy in both 2D and 3D culture. We find cells in 3D culture are generally more sensitive to erlotinib, with DS8 sub lines more significant than others. Our work shows that besides the structural changes from 2D to 3D, increased stiffness of the environmental are inversely correlated to increase in drug sensitivity. Further protein expression investigation points to a classic cell cycle model modulated by EGFR, integrin and c-Met.

7. CONCLUSIONS AND DISCUSSION

We started this work aiming to extend the application of mathematical models in medical imaging to design rational treatment schedule that optimizes therapy output. We established the rationale of our approach through observations of the *in vitro* cell culture experiments, simulation test of modeling methods, and cross validation between experiments and modeling. We identified mathematical models that both capture a wide range of tumor cell growth, and yet simple enough to be used for parameter extraction and drug response prediction. We combined tumor models of drug response with *in silico* clinical DW-MR imaging to suggest frequency and constraints of tumor condition that allow effectively identifying resistance in early course of targeted therapy. To bridge the gap between model testing and experimental application, we studied the PC9 lung cancer cell lines in 3D environment in the vision of a 3D controllable cell culture that can be used to test and improve tumor model. We found that the PC9 lung cancer cell lines tend to be more sensitive to erlotinib in 3D culture compare to 2D, and obtained preliminary evidence that establishes the correlation between drug sensitivity and stiffness of cell environment. In this chapter, we will summarize the results of each chapter, and suggest further work needed in theoretical development, experiments and quantification methods.

7.1 Two-state tumor model and cell diffusion model

Cancer modeling research often suffers from the drawback that sophisticated models of tumor growth involve too many parameters that are unobtainable in a single experimental setup. As one step towards simplifying, yet preserving the effectiveness of tumor models, we proposed and

validated the efficacy of a two-state tumor model that composes of both sensitive and resistant phenotypes. We proved that for either sensitive phenotype that follows exponential decay curve, or resistant phenotype that has logistic growth curve, the summation of many cell lines with a range of growth or decay rates can be grouped and represented by a single growth or decay rate. This model is particularly helpful in the context of clinical imaging where information about the sub cell lines within the tumor tissue is often not measurable. The model can also be used in combination of multi-scale *in vitro* cell culture, where researchers can cross validate the observations from both micro and macro levels.

7.2 Testing the diffusion models

There is currently a vacancy in literature observing the spatial interaction of multi-phenotype cancer cells. The current widely used diffusion model is similar to that of ideal gas and unsuitable to describe the random motion of tumor cells on the macro scales, especially in cases where multiple phenotypes are present. We introduced a new application of diffusion model in cell culture. Our proposed model from Burger et al[92] assumes the random migration of one phenotype is constrained by others that occupy adjacent space, and yet conserves the cell counts for each phenotype. In this thesis, we introduced our preliminary experimental effort to test and compare these two diffusion models. The statistical analysis of the conducted experiments indicated no significant advantage of either model. There are two key aspects to improve the experimental setup. First, we need to create an effective blockage to prevent cells from growing in vertical dimension in the 2D setup or set up experiment in 3D. We observed that in our 2D experimental setups, both cell lines tend to grow above the observation plane. It significantly increased the difficulty to obtain accurate cell counts as well as set the carrying capacity for the

2D model. Secondly, it's preferable to use other separate method that narrows the initial set-up gap between two cell lines (currently around 500μm) to allow the immediate observation of cell invasions to adjacent space once the blockage is removed.

7.3 Application of tumor modeling in clinical imaging

Empowered by the advances in clinical imaging, such as MRI, physicians can conveniently obtain the 3D high resolution tumor information non-invasively. Using *in silico* simulations, we demonstrated how medical available imaging such as diffusion-weighted MRI coupled with mathematical models of tumor drug response can be used to achieve early detection of drug resistance and predict tumor drug response from early course of neo-adjuvant therapy.

One significant, yet often ignored, factor to consider is the type and level of noise in the MRI system, and the rigorous methods to simulate the MRI noise of the interested experimental system. We found that the level of MRI noise significantly influences the accuracy of detecting the tumor resistance to targeted therapy. Though there are several literatures [101] [102] [103] [104] [105] that have investigated the noise level of DW-MRI *in vitro* and *in vivo*, they are mostly on the aggregated total tumor scale, not on the single pixel or voxel scale. As the use of mathematical modeling to diagnose and forecast tumor drug response becomes more ubiquitous and influential, it is important to establish more rigorous approach on simulating the fundamentals of MRI noise.

7.4 Tumor cells in 3D environment

From the series of experiments conducted in Chapter 6, a few key factors in modulating the DIP

rate stand out: ECM stiffness (manifested in integrin expression and activation), EGFR blockage (ie. erlotinib treatment), and the innate difference between discrete sub cell lines (highlighted by the difference in c-MET expression). Indeed, these factors are well recognized in cell-cycle related signaling pathways studied in molecular biology[118-120]. As shown in Figure 7.1, either the activation of c-Met, integrin, or EGFR could stimulate the FAK-PI3K-Akt pathway, thus promoting unlimited and deregulated cell proliferation though the activation of Cyclin B and D, and escape apoptosis through the eventual inhibition of BDX[121]. Similarly, either c-Met or EGFR expression could modulate the Ras-Raf-MEK-ERK pathway to achieve heightened cell proliferation and reduced apoptosis. There are existing quantitative cell proliferation cycle[122, 123] and cell apoptosis models[124] available in the literature that take input from the core upstream factors such as Akt, ERK and BDX. These factors are known to be influenced by experimentally controllable conditions such as the ECM stiffness, EGFR inhibition, and c-Met activation.

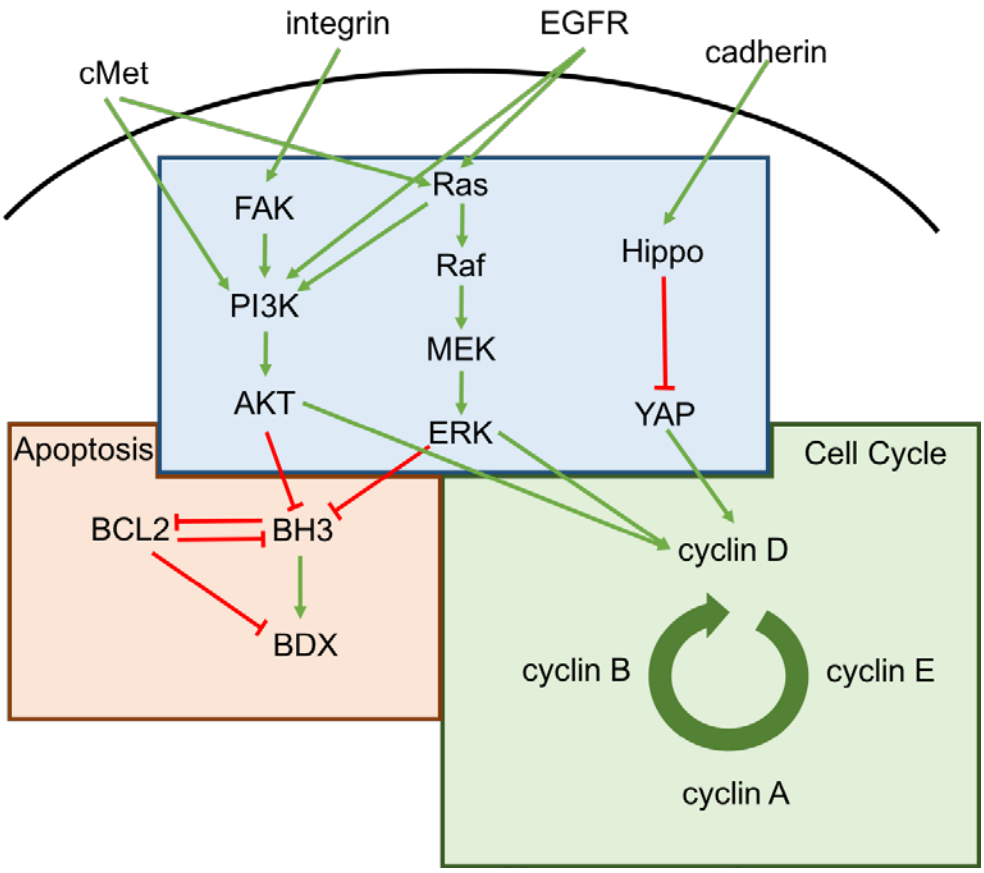

Figure 7.1 Cell signaling pathways related to cell proliferation and apoptosis mediated by c-Met, integrin, EGFR and cadherin expression. The result graph is synthesized from reference[118-125].

To further enhance the application of our cell studies result, we propose the following steps to build a comprehensive signaling pathway model that predicts tumor proliferation (ie. range of DIP rates) given biopsy or non-invasive imaging measurements.

(1) Adapt and combine existing cell-cycle modules to our experimental needs. Cell cycle modeling is an extensively studied area. Cell phase transition can be modeled as sequential activation of the network of cyclin-dependent kinases (Cdks)[122, 123]. Correspondingly, cell

death can be modeled as the activation of proapoptotic protein BDX[124]. Factors such as focal adhesion kinase (FAK), protein kinase B (Akt), the MAPK/ERK pathway and YAP pathway are known to play a key role in the balance between apoptosis, quiescence, and proliferation. These factors are directly mediated by extracellular signals that are associated with experimental set up. A stochastic model modulated by FAK, Akt, and YAP pathway states and that generates cell fates such as mitosis, quiescence and apoptosis is important to bridge experimental conditions and the corresponding DIP rates.

(2) Map experimental stiffness with DIP rate for sub cell lines, and record the subsequent key protein expression using western blotting. In Chapter 6, we presented our preliminary experiments that investigate the influence of surface stiffness to DIP rate in DS8 and DS9. Erlotinib treatment blocks EGFR activation, and the consequent DIP rates are modulated mainly by integrin and c-Met expression level. For each discrete sub line (relatively controlled c-Met expression), we found the erlotinib treated DIP rates are positively and linearly correlated with the logarithm of surface stiffness (integrin activation). As we learned from previous experiments by the Quaranta group, one can add the c-Met inhibitor foretinib to isolate the influence from c-Met expression and establish direct mapping from ECM condition to corresponding DIP rates. Two more sets of experiments using PA gel modulated surface stiffness around 7.5kPa and 665kPa will further validate (or overturn) our existing finding. Additionally, in order to link the stiffness to DIP rates in modeling, it is important to record corresponding key protein expression such as c-Met, Akt, BDX and FAK under each experimental setting for later modeling analysis.

(3) Reproduce step (2) measured DIP under each stiffness condition using models built in step (1). Through tuning parametersin models built in step (1), one can identify the corresponding

Akt and BDX expression levels that optimally reproduce experimentally observed DIP distribution in step (2). Through the mapping from stiffness condition and c-Met expression to Akt and BDX expressions, we not only can interpret the previous experiments, but use it for prediction of DIP distribution under unexplored conditions.

(4) Predict DIP rates in new cell lines. As factors such as integrin expression are believed to be mostly the consequence of external stimuli, c-Met expression are distinctly and innately different in DS8 and DS9. c-Met is known for influencing proliferation, migration, invasion, and angiogenesis[120]. We propose to use measured c-Met activation and surface stiffness in Young's modulus to predict the DIP rates in new cell lines.

In addition to the above described future steps, it would also be interesting to investigate the influence of contact inhibition on carrying capacity. In this thesis, we used a logistic growth model to capture change in tumor growth rate, where cell growth is mediated by growth rate k at low cell density and proliferate significantly slower when tumor cells reach carrying capacity. From both previously conducted experiments in 2D and 3D, we found that carrying capacity is distinct between sub cell lines. By measuring the protein expression levels in Hippo-YAP pathways[125] of each sub line, it's promising to interpret the difference in the observed carrying capacity. This would overall provide the bridge to link long term cell population to the cell lines of interest.

7.5 3D cell tracking

In the course of spatial information extraction from 3D confocal images, we also developed segmentation methods to effectively obtain cell location information in 3D space. Our approach is logic based, and consequently is still vulnerable to significant changes in imaging condition and noise level. Recent development in machine learning, especially deep learning based image

analysis techniques, has shown robust accuracy against distinct image settings in other areas of visual recognition[126-128]. We suggest future development of image analysis techniques to incorporate methods such as linear regression classifier, supporting vector machine, and neural network[129-132] to address image analysis needs.

7.6 Conclusions

Our work showed the promise of harnessing non-invasive imaging and modeling towards early detection of tumor resistance to targeted therapy. We described our experimental findings in this direction that bridges the gap between theory and implementation. More direct experimentations are required to test the hypothesis proposed in the thesis. The project to build an *in vitro* system, such as bioreactor that cultures mammalian cells and allows for both Optical Microscopy and Magnetic Resonance Imaging, is ongoing under collaboration between Yankeelov, Quranta, and Rericha lab at Vanderbilt University. We can apply knowledge gained from our series of 2D *in silico* experiments described in this thesis to the bioreactor system, and use bioreactor system to directly test our framework of early resistance detection.

APPENDIX

Cell Segmentation

A.1 2D cell segmentation

Key measures of the growth or drug response of tumor cells is the evolution of cell counts in time. For cells growing in the 2D environment, the cell nuclei labeled with Red Fluorescent Protein appear mostly to be spatially separated oval objects in the red channel. Occasionally, these oval objects can overlap with each other mainly due to two factors: (1) when cells go through the mitosis process (so called M phase), two nuclei are physically connected; (2) the point spread function [133] (the blurring of a point object due to the nature of the imaging system) of the imaging system creates the illusion of connected nuclei when two nuclei are close enough to each other.

To count the number of spatially separated cells, one can use *MATLAB* built-in function *imfindcircles(): (1)* create binary image by thresholding the original image; (2) clear out small noisy particles; (3) count the number of connected regions.

To count the number of spatially connected cells involves more steps. We create effective segmentation algorithm by combing and adjusting the segmentation algorithm described in references[130, 134, 135]. Briefly, one needs to first apply smooth filters to the image of interest, and this step will be helpful to obtain smoother boundaries at later stages. One can then create binary images and clear out small noisy particles. Next, as a critical step, one will need to find out the boundaries of the larger connected regions, and identify concave points at the boundary. If

more than two concave points exist, one can create segmentation paths following rules described in the references[134, 135].

A.2 3D cell segmentation

As for cell segmentation in 3D, steps and functions used are similar to segmentation in 2D with a few exceptions. In the 3D stacks, z direction represents the vertical direction compared to the horizontal plane (x-y plane). Consequently, 3D stacks are also called z-stacks. At first, we loop through each x-y plane and segment each x-y plane's 2D image using the 2D segmentation method. During testing, we found that for images at different horizontal planes, the 2D segmentation line may shift, and eventually results in the unsuccessful segmentation in 3D. We dealt with this issue using three steps (1) we applied stricter rules (such as higher convex value, and lower point to point distance) to generate segmentation lines. (2) in occasions where segmentation paths in the 2D were generated based on the concave points, a vertical plane,Z plane (mathematically, a 2D matrix), that contains the segmentation path was generated. (3) generate a 3D segmentation by converting pixels that are both within the Z plane region and also contain the segmentation path from TRUE to FALSE. After all the regions in the x-y plane and each x-y plane in the z-stack are iterated, we filtered out small 3D objects (usually 10- 20 pixels) created during the process of segmentation. Refer to Figure A1 (3) for 3D segmentation steps.

We implemented segmentation methods inspired by works of [130, 134, 135]. The basic procedures employed in our segmentation method for 2D images are as follows. A typical raw gray image is shown in Fig A1 (1).

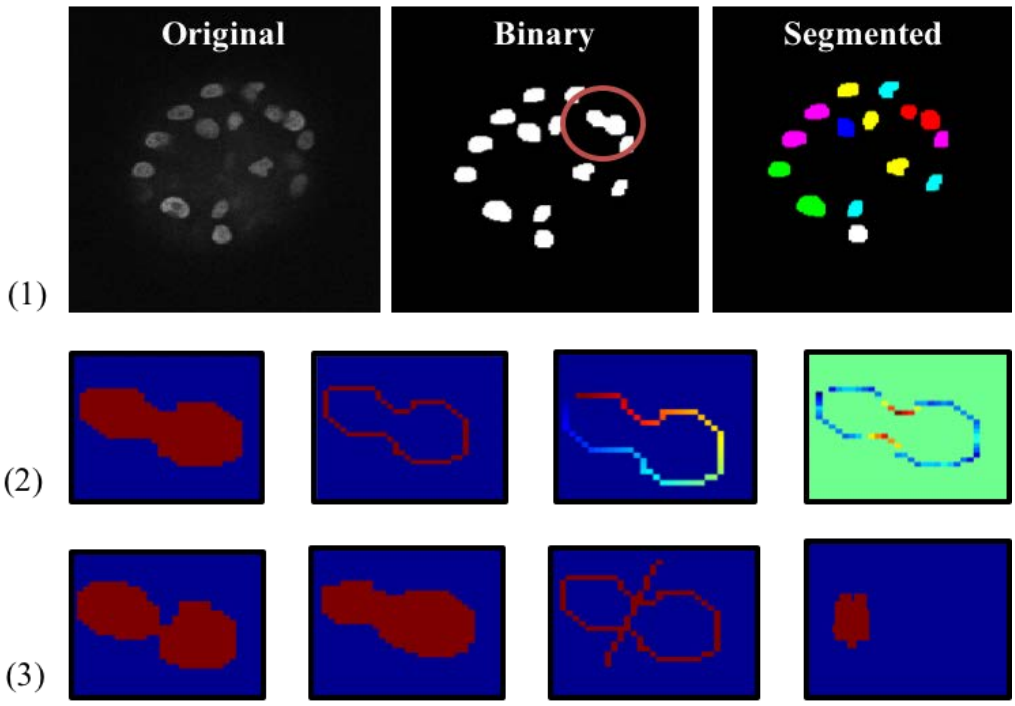

Figure A1 (1) progression of cell segmentation process. From left, the process starts with the original gray image. Secondly, the gray image is smoothed and thresholded into binary image. The red circle marked region is of interest to be further segmented into two individual cells. Finally, we show the result of using segmentation algorithm to generate cluster with independent and disconnected individual cells for further quantification and analysis. (2) The boundary processing of the segmentation algorithm. Starting with the connected two cells in the binary image, the first step is to identify the boundary for the region of interest (second from the left). Secondly, all the points at the boundary are ordered in a counter clock wise (third form the left) manner to establish the basis of identifying concave points (the right most). The concave points in the right most image are marked as red due high concave value. (3) Segmentation path generation and final segmentation based on the boundary processing in (2). From the left, binarized image on the Z-1 plane of the same region. Second from the left, binarized image on the Z+1 plane of the same region. Third from the left, Bresenham line is generated using the two concave points found in (2). Right most, view from the Bresenham line along the Z direction. The region shown in the final graph is nullified as no cell region to finalize the segmentation.

(1) we filter the raw image using *MATLAB* built-in median filter *medfilt2()*. Based on the quality of image, one can adjust the length and height of the filtering window. In the work of this thesis, we generally used windows of 3x3 or 4x4 pixels.

(2) we binarize the image after the smoothing process in step 1 by setting a threshold. Choosing a proper threshold is critical for later stages of boundary creation and segmentation. To achieve this effectively, we use *MATLAB* built-in function *multithresh()* and *imquantize()* to visualize automatically generated multi-level thresholds' effect on the image using widely adopted Otsu method. After a proper threshold (a certain pixel intensity) is selected, we apply *imquantize()* again to finish up the binarization process. Imquantize takes in user specified threshold value between 0 and the maximum value in the image.

Alternatively, one may also use *im2bw()* to choose a threshold between 0 and 1. Though *im2bw()* gives a more intuitive choice, through practice, we find *imquantize()* gives a more desired result.

(3) we clear out small noise particles using *MATLAB*'s built-in function *imopen()* in combination with *strel()*. One can use *strel()* to create desired shapes, such as diamond and disc, and size of the noise particles to be eliminated, and then use *imopen()* to filter out the noise particles.

(4) we use *bwlabel()* to label distinct connected regions in the binary image after it is processed in step 3. For example, in Figure A1 (1) and Figure A2 the original binary images are then converted double precision matrix, and each distinct color corresponds to different unconnected regions. The *bwlabel()* function employs standard and widely cited grouping procedure outlined in the reference.

(5) We create loop through the distinct regions, to use *bwmorph()* in ‘erode’ mode to find out the boundaries of each region. Each loop contains step (5) to (8).

(6) For each boundary of interest, we first re-order the boundary points in clockwise manner, see Figure A1 (2) and calculate the corresponding curvature value and convex property of each point, see Figure A1 (2).

(7) If two or more convex points that above the convex value threshold (eg. 30 degree) appears within one boundary, see Figure A1 (2), we use opposition metrics described in previous work[134, 135] as well as the direct and peripheral distance between points to generate the pairing score[134, 135] that gives out the optimal pairing of all the convex points.

(8) Each pair of convex points is used to generate connected lines as the segmentation line for the connected regions. We use Bresenham’s line algorithm[136] to generate the segmentation path. When pixels on the segmentation path are identified, they are converted from TRUE to FALSE, which creates a gap within the initially connected regions, thus segmented one region into two or more regions. Refer to Figure A1 (3) for generated Bresenham line.

(9) After segmentation, we apply *bwconncomp()* to the binarized image, and it outputs connected components, *CC.* One can then use built-in *MATLAB* function *regionprops()* to collect the number of CC and their corresponding center of mass as well as other properties.

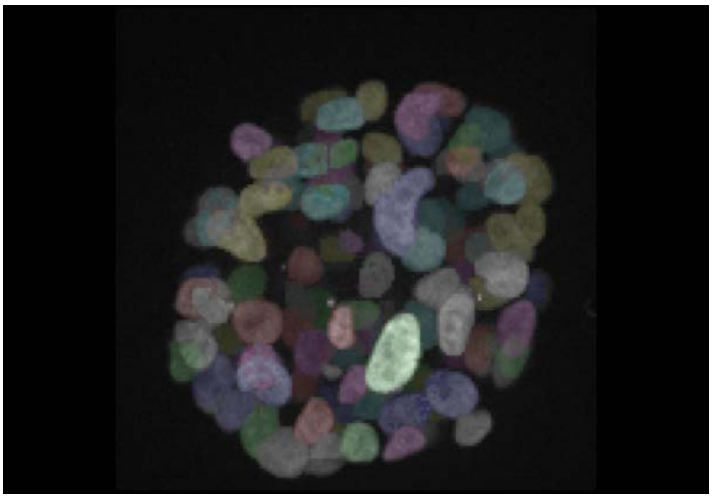

Figure A2 Y-Projection of the 3D cell cluster after segmentation. Each individual cells are labeled with distinct color to separate from the neighboring of the cells in the cluster. There are 104 cells in total in the shown cluster.

REFERENCES

[1] A. C. Society, *Global Cancer Facts and Figures 3rd Edition*. Atlanta: American Cancer Society, 2015.

[2] A. C. Society, *Cancer Facts and Figures*. Atlanta: American Cancer Society, 2017.

[3] W. S. Halsted, "I. A Clinical and Histological Study of certain Adenocarcinomata of the Breast: and a Brief Consideration of the Supraclavicular Operation and of the Results of Operations for Cancer of the Breast from 1889 to 1898 at the Johns Hopkins Hospital," *Annals of Surgery,* vol. 28, no. 5, pp. 557-576, 1898.

[4] W. S. Halsted, "I. The Results of Radical Operations for the Cure of Carcinoma of the Breast," *Annals of Surgery,* vol. 46, no. 1, pp. 1-19, 1907.

[5] "National Surgical Adjuvant Breast and Bowel Project (NSABP)," 1998.

[6] B. Fisher *et al.*, "Ten-Year Results of a Randomized Clinical Trial Comparing Radical Mastectomy and Total Mastectomy with or without Radiation," *New England Journal of Medicine,* vol. 312, no. 11, pp. 674-681, 1985.

[7] R. Demicheli, M. W. Retsky, W. J. M. Hrushesky, M. Baum, and I. D. Gukas, "The effects of surgery on tumor growth: a century of investigations," *Annals of Oncology,* vol. 19, no. 11, pp. 1821-1828, 2008.

[8] A. H. Compton, "A Quantum Theory of the Scattering of X-rays by Light Elements," *Physical Review,* vol. 21, no. 5, pp. 483-502, 1923.

[9] S. Gu *et al.*, "Applying a patient-specific bio-mathematical model of glioma growth to develop virtual [18F]-FMISO-PET images," *Math Med Biol,* vol. 29, no. 1, pp. 31-48, 2012.

[10] R. C. Rockne *et al.*, "A patient-specific computational model of hypoxia-modulated radiation resistance in glioblastoma using 18F-FMISO-PET," *Journal of The Royal Society Interface,* vol. 12, no. 103, 2014.

[11] M. D. Szeto *et al.*, "Quantitative metrics of net proliferation and invasion link biological aggressiveness assessed by MRI with hypoxia assessed by FMISO-PET in newly diagnosed glioblastomas," *Cancer research,* vol. 69, no. 10, pp. 4502-4509, 2009.

[12] S. N. Gardner, "Cell cycle phase-specific chemotherapy: computational methods for guiding treatment," *Cell Cycle,* vol. 1, no. 6, pp. 369-374, 2002

[13] R. S. Day, "A branching-process model for heterogeneous cell populations," *Mathematical Biosciences,* vol. 78, no. 1, pp. 73-90, 1986.

[14] R. S. Day, "Treatment Sequencing, Asymmetry, and Uncertainty: Protocol Strategies for Combination Chemotherapy," *Cancer Research,* vol. 46, no. 8, pp. 3876-3885, 1986.

[15] A. A. Katouli and N. L. Komarova, "The Worst Drug Rule Revisited: Mathematical Modeling of Cyclic Cancer Treatments," *Bulletin of Mathematical Biology,* vol. 73, no. 3, pp. 549-584, 2010.

[16] V. T. DeVita and E. Chu, "A History of Cancer Chemotherapy," *Cancer Research,* vol. 68, no. 21, pp. 8643-8653, 2008.

[17] C. Khanna, M. Rosenberg, and D. M. Vail, "A Review of Paclitaxel and Novel Formulations Including Those Suitable for Use in Dogs," *Journal of Veterinary Internal Medicine,* vol. 29, no. 4, pp. 1006-1012, 2015.

[18] J. S. Lanni, S. W. Lowe, E. J. Licitra, J. O. Liu, and T. Jacks, "p53-independent apoptosis induced by paclitaxel through an indirect mechanism," *Proceedings of the National Academy of Sciences,* vol. 94, no. 18, pp. 9679-9683, 1997.

[19] B. Fisher, "From Halsted to prevention and beyond: advances in the management of breast cancer during the twentieth century," *European Journal of Cancer,* vol. 35, no. 14, pp. 1963-1973, 1999

[20] O. Tacar, P. Sriamornsak, and C. R. Dass, "Doxorubicin: an update on anticancer molecular action, toxicity and novel drug delivery systems," *Journal of Pharmacy and Pharmacology,* vol. 65, no. 2, pp. 157-170, 2013.

[21] H. Mizutani, S. Tada-Oikawa, Y. Hiraku, M. Kojima, and S. Kawanishi, "Mechanism of apoptosis induced by doxorubicin through the generation of hydrogen peroxide," *Life Sciences,* vol. 76, no. 13, pp. 1439-1453, 2005.

[22] NCI. (2016). *Milestones in Cancer Research and Discovery*.

[23] J. D. Watson and F. H. C. Crick, "A Structure for Deoxyribose Nucleic Acid," *Nature,* vol. 171, pp. 737-738, 1953.

[24] D. Hanahan and R. A. Weinberg, "The Hallmarks of Cancer," *Cell,* vol. 100, no. 1, pp. 57-70, 2000.

[25] D. Hanahan and Robert A. Weinberg, "Hallmarks of Cancer: The Next Generation," *Cell*, vol. 144, no. 5, pp. 646-674, 2011.

[26] M. C. Muller *et al.*, "Dynamics of BCR-ABL mRNA expression in first-line therapy of chronic myelogenous leukemia patients with imatinib or interferon [alpha]//ara-C," *Leukemia*, vol. 17, no. 12, pp. 2392-2400, 2003.

[27] F. Michor *et al.*, "Dynamics of chronic myeloid leukaemia," *Nature*, vol. 435, no. 7046, pp. 1267-1270, 2005.

[28] R. I. Nicholson, J. M. W. Gee, and M. E. Harper, "EGFR and cancer prognosis," *European Journal of Cancer*, vol. 37, pp. 9-15, 2001.

[29] S. Mukherjee, *The Emperor of All Maladies: A Biography of Cancer*. Scribner, 2010, p. 608.

[30] B. Goodman, "Cancer: emperor of all maladies," ed: Public Broadcasting Service, 2015.

[31] J. Furth, M. C. Kahn, and C. Breedis, "The Transmission of Leukemia of Mice with a Single Cell," *The American Journal of Cancer*, vol. 31, no. 2, pp. 276-282, 1937.

[32] E. J. Freireich, M. Karon, and E. Frei Iii, "Quadruple combination therapy (VAMP) for acute lymphocytic leukemia of childhood," 1964, vol. 5, p. 20.

[33] P. Castorina, D. Carcò, C. Guiot, and T. S. Deisboeck, "Tumor growth instability and its implications for chemotherapy," *Cancer research*, vol. 69, no. 21, pp. 8507-8515, 2009.

[34] L. Norton, "Cancer log-kill revisited," *American Society of Clinical Oncology Education Book*, pp. 3-7, 2014.

[35] J. Foo and F. Michor, "Evolution of resistance to targeted anti-cancer therapies during continuous and pulsed administration strategies," *PLoS Comput Biol*, vol. 5, no. 11, Nov 2009.

[36] A. J. Coldman and J. H. Goldie, "Role of mathematical modeling in protocol formulation in cancer chemotherapy," *Cancer treatment reports*, vol. 69, no. 10, pp. 1041-1048, 1985.

[37] S. Benzekry *et al.*, "Classical Mathematical Models for Description and Prediction of Experimental Tumor Growth," *PLoS Computational Biology* vol. 10, no. 8, 2014.

[38] L. G. d. P. E. A. Sarapata "A Comparison and Catalog of Intrinsic Tumor Growth Models," *Bulletin of Mathematical Biology*, vol. 76, no. 8, pp. 2010-2024, 2014.

[39] V. G. Vaidya and F. J. Alexandro Jr, "Evaluation of some mathematical models for tumor growth," *International Journal of Bio-Medical Computing*, vol. 13, no. 1, pp. 19-35, 1982.

[40] P. Gerlee, "The Model Muddle: In Search of Tumor Growth Laws," *Cancer Research,* vol. 73, no. 8, pp. 2407-2411, 2013.

[41] M. Abercrombie, "Contact inhibition and malignancy," *Nature,* vol. 281, no. 5729, pp. 259-262, 1979.

[42] L. A. Dethlefsen, J. M. S. Prewitt, and M. L. Mendelsohn, "Analysis of Tumor Growth Curves," *Journal of the National Cancer Institute,* vol. 40, no. 2, pp. 389-405, 1968.

[43] A. K. Laird, "Dynamics of Tumour Growth," *British Journal of Cancer,* vol. 18, no. 3, pp. 490-502, 1964.

[44] L. von Bertalanffy, "Problems of organic growth," *Nature,* vol. 163, no. 4135, pp. 156-158, 1949.

[45] L. Norton and J. Massague, "Is cancer a disease of self-seeding?," *Nat Med,* vol. 12, no. 8, pp. 875-878, 2006.

[46] E. A. Eisenhauer *et al.*, "New response evaluation criteria in solid tumours: revised RECIST guideline (version 1.1)," *Eur J Cancer,* vol. 45, no. 2, pp. 228-47, 2009.

[47] R. Simon and L. Norton, "The Norton-Simon hypothesis: designing more effective and less toxic chemotherapeutic regimens," *Nature Clinical Practice Oncology,* Clinical report vol. 3, p. 406, 2006.

[48] A. R. A. Anderson and M. A. J. Chaplain, "Continuous and discrete mathematical models of tumor-induced angiogenesis," *Bulletin of Mathematical Biology,* vol. 60, no. 5, pp. 857-899, 1998.

[49] H. M. Byrne, "Dissecting cancer through mathematics: from the cell to the animal model," *Nat Rev Cancer,* vol. 10, no. 3, pp. 221-230, 2010.

[50] V. Cristini, X. Li, J. S. Lowengrub, and S. M. Wise, "Nonlinear simulations of solid tumor growth using a mixture model: invasion and branching," *Journal of mathematical biology,* vol. 58, no. 4-5, pp. 723-763, 2009.

[51] H. B. Frieboes *et al.*, "Prediction of drug response in breast cancer using integrative experimental/computational modeling," *Cancer research,* vol. 69, no. 10, pp. 4484-4492, 2009.

[52] H. B. Frieboes, F. Jin, Y. L. Chuang, S. M. Wise, J. S. Lowengrub, and V. Cristini, "Three-Dimensional Multispecies Nonlinear Tumor Growth–II: Tumor Invasion and Angiogenesis," *Journal of theoretical biology,* vol. 264, no. 4, pp. 1254-1278, 2010.

[53] S. M. Wise, J. S. Lowengrub, H. B. Frieboes, and V. Cristini, "Three-dimensional multispecies nonlinear tumor growth--I Model and numerical method," *J Theor Biol,* vol. 253, no. 3, pp. 524-43, 2008.

[54] H. P. Greenspan, "Models for the Growth of a Solid Tumor by Diffusion," *Studies in Applied Mathematics,* vol. 51, no. 4, pp. 317-340, 1972.

[55] J. A. Madri and B. M. Pratt, "Endothelial cell-matrix interactions: in vitro models of angiogenesis," *Journal of Histochemistry & Cytochemistry,* vol. 34, no. 1, pp. 85-91, 1986.

[56] M. E. Orme and M. A. J. Chaplain, "A mathematical model of vascular tumour growth and invasion," *Mathematical and Computer Modelling,* vol. 23, no. 10, pp. 43-60, 1996.

[57] K. R. Swanson, C. Bridge, J. D. Murray, and E. C. Alvord, Jr., "Virtual and real brain tumors: using mathematical modeling to quantify glioma growth and invasion," *Journal of the Neurological Sciences,* vol. 216, no. 1, pp. 1-10, 2013.

[58] D. A. I. Hormuth *et al.,* "Predicting in vivo glioma growth with the reaction diffusion equation constrained by quantitative magnetic resonance imaging data," *Physical Biology,* vol. 12, no. 4, p. 046006, 2015.

[59] J. A. Weis *et al.,* "A mechanically coupled reaction-diffusion model for predicting the response of breast tumors to neoadjuvant chemotherapy," *Physics in medicine and biology,* vol. 58, no. 17, pp. 5851-5866, 2013.

[60] R. A. Gatenby and E. T. Gawlinski, "A Reaction-Diffusion Model of Cancer Invasion," *Cancer Research,* vol. 56, no. 24, pp. 5745-5753, 1996.

[61] K. R. Swanson, E. C. Alvord, and J. D. Murray, "A quantitative model for differential motility of gliomas in grey and white matter," *Cell Proliferation,* vol. 33, no. 5, pp. 317-329, 2000.

[62] D. L. Silbergeld and M. R. Chicoine, "Isolation and characterization of human malignant glioma cells from histologically normal brain," *Journal of Neurosurgery,* vol. 86, no. 3, pp. 525-531, 1997.

[63] P. Tracqui, G. C. Cruywagen, D. E. Woodward, G. T. Bartoo, J. D. Murray, and E. C. Alvord, "A mathematical model of glioma growth: the effect of chemotherapy on spatio-temporal growth," *Cell Proliferation,* vol. 28, no. 1, pp. 17-31, 1995.

[64] T. E. Yankeelov *et al.*, "Clinically Relevant Modeling of Tumor Growth and Treatment Response," *Science Translational Medicine,* vol. 5, no. 187, pp. 187ps9-187ps9, 2013-05-29 00:00:00 2013.

[65] J. Folkman and M. Klagsbrun, "Angiogenic factors," *Science,* vol. 235, no. 4787, pp. 442-447, 1987.

[66] T. T. Puck and P. I. Marcus, "Action of X-rays on mamalian cells," *The Journal of Experimental Medicine,* vol. 103, no. 5, pp. 653-666, 1956.

[67] H. D. Thames, S. M. Bentzen, I. Turesson, M. Overgaard, and W. Van den Bogaert, "Time-dose factors in radiotherapy: a review of the human data," *Radiotherapy and Oncology,* vol. 19, no. 3, pp. 219-235, 1990.

[68] R. G. Dale and B. Jones, "The assessment of RBE effects using the concept of biologically effective dose," *International Journal of Radiation Oncology,* vol. 43, no. 3, pp. 639-645, 1999.

[69] D. J. Brenner, "Point: The linear-quadratic model is an appropriate methodology for determining iso-effective doses at large doses per fraction," *Seminars in radiation oncology,* vol. 18, no. 4, pp. 234-239, 2008.

[70] M. Stuschke and H. D. Thames, "Hyperfractionated radiotherapy of human tumors: Overview of the randomized clinical trials," *International Journal of Radiation Oncology,* vol. 37, no. 2, pp. 259-267, 1997.

[71] B. J. Baujat B, Blanchard P, Overgaard J, Ang KK, Saunders M, A, Bernier J, Horiot JC, Maillard E, Pajak TF, Poulsen MG, Bourredjem A, O'Sullivan B, Dobrowsky W, Andrzej H, Skladowski K, Hay JH, Pinto LHJ, Fu KK, Fallai C, Sylvester R, Pignon JP, MARCH Collaborative Group, "Hyperfractionated or accelerated radiotherapy for head and neck cancer," *Cochrane Database System Reviews,* no. 12, 2000.

[72] W. R. Lee, "Prostate Cancer and the Hypofractionation Hypothesis," *Journal of Clinical Oncology,* vol. 31, no. 31, pp. 3849-3851, 2013.

[73] D. J. Brenner, A. A. Martinez, G. K. Edmundson, C. Mitchell, H. D. Thames, and E. P. Armour, "Direct evidence that prostate tumors show high sensitivity to fractionation, similar to late-responding normal tissue," *International Journal of Radiation Oncology,* vol. 52, no. 1, pp. 6-13, 2002.

[74] R. Miralbell, S. A. Roberts, E. Zubizarreta, and J. H. Hendry, "Dose-Fractionation Sensitivity of Prostate Cancer Deduced From Radiotherapy Outcomes of 5969 Patients in Seven International Institutional Datasets," *International Journal of Radiation Oncology,* vol. 82, no. 1, pp. 17-24, 2012.

[75] E. E. Yeoh, R. J. Botten, J. Butters, A. C. Di Matteo, R. H. Holloway, and J. Fowler, "Hypofractionated Versus Conventionally Fractionated Radiotherapy for Prostate Carcinoma: Final Results of Phase III Randomized Trial," *International Journal of Radiation Oncology,* vol. 81, no. 5, pp. 1271-1278, 2011.

[76] M. Zaider, "There is no mechanistic basis for the use of the linear-quadratic expression in cellular survival analysis," *Medical Physics,* vol. 25, no. 5, pp. 791-792, 1998.

[77] E. E. P. Box and N. R. Draper, *Empirical Model-Building and Response Surfaces* New York City, New York John Wiley & Sons, 1987.

[78] P. L. Frick, B. B. Paudel, D. R. Tyson, and V. Quaranta, "Quantifying heterogeneity and dynamics of clonal fitness in response to perturbation," *Journal of Cellular Physiology,* vol. 230, no. 7, pp. 1403-1412, 2015.

[79] D. R. Tyson, S. P. Garbett, P. L. Frick, and V. Quaranta, "Fractional Proliferation: A method to deconvolve cell population dynamics from single-cell data," *Nature methods,* vol. 9, no. 9, pp. 923-928, 2012.

[80] C. Holohan, S. Van Schaeybroeck, D. B. Longley, and P. G. Johnston, "Cancer drug resistance: an evolving paradigm," *Nat Rev Cancer,* vol. 13, no. 10, pp. 714-726, 2013.

[81] P. B. Gupta, C. L. Chaffer, and R. A. Weinberg, "Cancer stem cells: mirage or reality?," *Nat Med,* vol. 15, no. 9, pp. 1010-1012, 2009.

[82] C. Chen, W. T. Baumann, R. Clarke, and J. J. Tyson, "Modeling the estrogen receptor to growth factor receptor signaling switch in human breast cancer cells," *FEBS Letters,* vol. 587, no. 20, pp. 3327-3334, 2013.

[83] Y. Liu, D. el-Ashry, D. Chen, I. Ding, and F. Kern, "MCF-7 breast cancer cells overexpressing transfected cerbB-2 have an in vitro growth advantage in estrogen-depleted conditions and reduced estrogen-dependence and tamoxifensensitivity in vivo.," *Breast Cancer Research Treatment,* vol. 34, no. 2, pp. 97-117, 1995.

[84] C. Tomasetti and D. Levy, "Role of symmetric and asymmetric division of stem cells in developing drug resistance," *Proceedings of the National Academy of Sciences of the United States of America,* vol. 107, no. 39, pp. 16766-16771, 2010.

[85] A. Hochhaus *et al.,* "Six-year follow-up of patients receiving imatinib for the first-line treatment of chronic myeloid leukemia," *Leukemia,* vol. 23, no. 6, pp. 1054-1061, 2009.

[86] I. Bozic, B. Allen, and M. A. Nowak, "Dynamics of targeted cancer therapy," *Trends in Molecular Medicine,* vol. 18, no. 6, pp. 311-316, 2012.

[87] V. Almendro *et al.,* "Inference of Tumor Evolution during Chemotherapy by Computational Modeling and In Situ Analysis of Genetic and Phenotypic Cellular Diversity," *Cell Reports,* vol. 6, no. 3, pp. 514-527, 2013.

[88] I. Roeder, M. Horn, I. Glauche, A. Hochhaus, M. C. Mueller, and M. Loeffler, "Dynamic modeling of imatinib-treated chronic myeloid leukemia: functional insights and clinical implications," *Nat Med,* vol. 12, no. 10, pp. 1181-1184, 2006.

[89] H. Kitano, "Cancer robustness: Tumour tactics," *Nature,* vol. 426, no. 6963, pp. 125-125, 2003.

[90] H. C. Berg, *Random Walks in Biology* (Princeton paperbacks). Princeton University Press, 1993.

[91] A. Okubo and S. A. Levin, *Diffusion and Ecological Problems: Modern Perspectives* (Interdisciplinary Applied Mathematics). Springer New York, 2002.

[92] M. D. F. Martin Burger, Jan-Frederik Pietschmann, and Bärbel Schlake, "Nonlinear Cross-Diffusion with Size Exclusion," *SIAM Journal on Mathematical Analysis,* vol. 42, no. 6, pp. 2842-2871, 2010.

[93] A. W. Anderson, J. Xie, J. Pizzonia, R. A. Bronen, D. D. Spencer, and J. C. Gore, "Effects of cell volume fraction changes on apparent diffusion in human cells," *Magn Reson Imaging,* vol. 18, no. 6, pp. 689-95, 2000.

[94] H. Lyng, O. Haraldseth, and E. K. Rofstad, "Measurement of cell density and necrotic fraction in human melanoma xenografts by diffusion weighted magnetic resonance imaging," *Magn Reson Med,* vol. 43, no. 6, pp. 828-36, 2000.

[95] Y. Hayashida *et al.*, "Diffusion-weighted imaging of metastatic brain tumors: Comparison with histologic type and tumor cellularity," *American Journal of Neuroradiology,* vol. 27, no. 7, pp. 1419-1425, 2006.

[96] K. Kono *et al.*, "The role of diffusion-weighted imaging in patients with brain tumors," *AJNR Am J Neuroradiol,* vol. 22, no. 6, pp. 1081-8, 2001.

[97] R. Mills, "Self-diffusion in normal and heavy water in the range 1-45.deg," *The Journal of Physical Chemistry,* vol. 77, no. 5, pp. 685-688, 1973.

[98] C. A. Nkiruka, C. G. John, and E. Y. Thomas, "The integration of quantitative multi-modality imaging data into mathematical models of tumors," *Physics in Medicine and Biology,* vol. 55, no. 9, p. 2429, 2010.

[99] L. R. A. Nkiruka C. Atuegwu, Xia Li, E. Brian Welch, Bapsi A. Chakravarthy, John C. Gore and Thomas E. Yankeelov, "Integration of diffusion-weighted MRI data and a simple mathematical model to predict breast tumor cellularity during neoadjuvant chemotherapy," *Magn Reson Med,* vol. 66, no. 6, pp. 1689-1696, 2011.

[100] N. A. Thomas E. Yankeelov, David Hormuth, Jared A. Weis, Stephanie L. Barnes, Michael I. Miga, Erin C. Rericha, Vito Quaranta, "Clinically Relevant Modeling of Tumor Growth and Treatment Response," *Science Translational Medicine,* vol. 5, no. 187, p. 5, 2013.

[101] M. Grech-Sollars *et al.*, "Multi-centre reproducibility of diffusion MRI parameters for clinical sequences in the brain," *NMR in Biomedicine,* vol. 28, no. 4, pp. 468-485, 2015.

[102] K. Miyazaki *et al.*, "Demonstration of the reproducibility of free-breathing diffusion-weighted MRI and dynamic contrast enhanced MRI in children with solid tumours: a pilot study," *European Radiology,* vol. 25, no. 9, pp. 2641-2650, 2015.

[103] M. E. Miquel, A. D. Scott, N. D. Macdougall, R. Boubertakh, N. Bharwani, and A. G. Rockall, "In vitro and in vivo repeatability of abdominal diffusion-weighted MRI," *The British Journal of Radiology,* vol. 85, no. 1019, pp. 1507-1512, 2012.

[104] J. G. Whisenant, G. D. Ayers, M. E. Loveless, S. L. Barnes, D. C. Colvin, and T. E. Yankeelov, "Assessing reproducibility of diffusion-weighted magnetic resonance imaging studies in a murine model of HER2+breast cancer," *Magnetic Resonance Imaging,* vol. 32, no. 3, pp. 245-249, 2014.

[105] D. Malyarenko *et al.*, "Multi-system repeatability and reproducibility of apparent diffusion coefficient measurement using an ice-water phantom," *Journal of magnetic resonance imaging : JMRI,* vol. 37, no. 5, pp. 1238-1246, 2013.

[106] J. M. Bland and D. G. Altman, "Statistics Notes: Measurement error proportional to the mean," *BMJ,* vol. 313, no. 7049, p. 106, 1996.

[107] C. M. Das, F. Becker, S. Vernon, J. Noshari, C. Joyce, and P. R. C. Gascoyne, "Dielectrophoretic Segregation of Different Human Cell Types on Microscope Slides," *Analytical Chemistry,* vol. 77, no. 9, pp. 2708-2719, 2005.

[108] H. Akaike, "A new look at the statistical model identification," *IEEE Trans Auto Control.,* no. 19, pp. 716-23, 1974.

[109] W. Pao *et al.,* "EGF receptor gene mutations are common in lung cancers from ‚Äúnever smokers‚Äù and are associated with sensitivity of tumors to gefitinib and erlotinib," *Proceedings of the National Academy of Sciences of the United States of America,* vol. 101, no. 36, pp. 13306-13311, 2004.

[110] T. J. Lynch *et al.,* "Activating Mutations in the Epidermal Growth Factor Receptor Underlying Responsiveness of Non–Small-Cell Lung Cancer to Gefitinib," *New England Journal of Medicine,* vol. 350, no. 21, pp. 2129-2139, 2004.

[111] J. Tang, R. Salama, S. M. Gadgeel, F. H. Sarkar, and A. Ahmad, "Erlotinib resistance in lung cancer: current progress and future perspectives," *Front Pharmacol,* vol. 4, p. 15, 2013.

[112] D. T. Butcher, T. Alliston, and V. M. Weaver, "A tense situation: forcing tumour progression," *Nature reviews. Cancer,* vol. 9, no. 2, pp. 108-122, 2009.

[113] A. Cretu, P. Castagnino, and R. Assoian, "Studying the Effects of Matrix Stiffness on Cellular Function using Acrylamide-based Hydrogels," no. 42, p. 2089, 2010.

[114] J. F. Greenleaf, M. Fatemi, and M. Insana, "Selected methods for imaging elastic properties of biological tissues," *Annu Rev Biomed Eng,* vol. 5, pp. 57-78, 2003.

[115] A. M. Collinsworth, S. Zhang, W. E. Kraus, and G. A. Truskey, "Apparent elastic modulus and hysteresis of skeletal muscle cells throughout differentiation," *Am J Physiol Cell Physiol,* vol. 283, no. 4, pp. C1219-1227, Oct 2002.

[116] E. Gherardi, W. Birchmeier, C. Birchmeier, and G. Vande Woude, "Targeting MET in cancer: rationale and progress," *Nat Rev Cancer,* vol. 12, no. 2, pp. 89-103, 2012.

[117] J. G. Kirkwood, V. A. Lewinson, and B. J. Alder, "Radial Distribution Functions and the Equation of State of Fluids Composed of Molecules Interacting According to the Lennard - Jones Potential," *The Journal of Chemical Physics,* no. 20, pp. 929-938, 1952.

[118] P. Moreno-Layseca and C. H. Streuli, "Signalling pathways linking integrins with cell cycle progression," *Matrix Biol,* vol. 34, pp. 144-53, 2014.

[119] G. Chen, P. Kronenberger, E. Teugels, I. A. Umelo, and J. De Grève, "Targeting the epidermal growth factor receptor in non-small cell lung cancer cells: the effect of combining RNA interference with tyrosine kinase inhibitors or cetuximab," *BMC Med,* vol. 10, p. 28, Mar 2012.

[120] J. R. Sierra and M. S. Tsao, "c-MET as a potential therapeutic target and biomarker in cancer," *Ther Adv Med Oncol,* vol. 3, pp. S21-35, Nov 2011.

[121] F. Chang *et al.*, "Involvement of PI3K/Akt pathway in cell cycle progression, apoptosis, and neoplastic transformation: a target for cancer chemotherapy," *Leukemia,* vol. 17, no. 3, pp. 590-603, Mar 2003.

[122] C. Gérard, D. Gonze, and A. Goldbeter, "Effect of positive feedback loops on the robustness of oscillations in the network of cyclin-dependent kinases driving the mammalian cell cycle," *FEBS J,* vol. 279, no. 18, pp. 3411-31, Sep 2012.

[123] C. Gérard and A. Goldbeter, "The balance between cell cycle arrest and cell proliferation: control by the extracellular matrix and by contact inhibition," *Interface Focus,* vol. 4, no. 3, p. 20130075, 2014.

[124] T. Zhang, P. Brazhnik, and J. J. Tyson, "Computational Analysis of Dynamical Responses to the Intrinsic Pathway of Programmed Cell Death," *Biophysical Journal,* vol. 97, no. 2, pp. 415-434, 2009.

[125] B. Zhao *et al.*, "Inactivation of YAP oncoprotein by the Hippo pathway is involved in cell contact inhibition and tissue growth control," *Genes Dev,* vol. 21, no. 21, pp. 2747-61, Nov 2007.

[126] H. Alon, "The Unreasonable Effectiveness of Data," *Expert Opinion,* vol. 24, no. 2, pp. 8-12, 2009.

[127] C. Bishop, *Pattern Recognition and Machine Learning*. Springer-Verlag New York, 2006.

[128] K. P. Murphy, *Machine Learning: A Probabilistic Perspective*. MIT Press, 2012.

[129] X. Lou, U. Koethe, J. Wittbrodt, and F. A. Hamprecht, "Learning to segment dense cell nuclei with shape prior," in *Computer Vision and Pattern Recognition (CVPR), 2012 IEEE Conference on*, 2012, pp. 1012-1018.

[130] L. Yang, O. Tuzel, P. Meer, and D. J. Foran, "Automatic Image Analysis of Histopathology Specimens Using Concave Vertex Graph," *Medical image computing and computer-*

assisted intervention : MICCAI ... International Conference on Medical Image Computing and Computer-Assisted Intervention, vol. 11, no. 0 1, pp. 833-841, 2008.

[131] Z. Yin, R. Bise, M. Chen, and T. Kanade, "Cell segmentation in microscopy imagery using a bag of local Bayesian classifiers," in *2010 IEEE International Symposium on Biomedical Imaging: From Nano to Macro*, 2010, pp. 125-128.

[132] O. Ronneberger, J. Fehr, and H. Burkhardt, "Voxel-Wise Gray Scale Invariants for Simultaneous Segmentation and Classification," in *Pattern Recognition: 27th DAGM Symposium, Vienna, Austria, August 31 - September 2, 2005. Proceedings*, W. G. Kropatsch, R. Sablatnig, and A. Hanbury, Eds. Berlin, Heidelberg: Springer Berlin Heidelberg, 2005, pp. 85-92.

[133] R. W. Cole, T. Jinadasa, and C. M. Brown, "Measuring and interpreting point spread functions to determine confocal microscope resolution and ensure quality control," *Nat. Protocols*, vol. 6, no. 12, pp. 1929-1941, 2011.

[134] C. Indhumathi, Y. Y. Cai, Y. Q. Guan, and M. Opas, "3D boundary extraction of confocal cellular images using higher order statistics," *Journal of Microscopy*, vol. 235, no. 2, pp. 209-220, 2009.

[135] C. Indhumathi, Y. Y. Cai, Y. Q. Guan, and M. Opas, "An automatic segmentation algorithm for 3D cell cluster splitting using volumetric confocal images," *Journal of Microscopy*, vol. 243, no. 1, pp. 60-76, 2011.

[136] J. E. Bresenham, "Algorithm for computer control of a digital plotter," *IBM Systems Journal*, vol. 4, no. 1, pp. 25-30, 1965.